Molecular Simulations of the Bulk-Heterojunction Morphology in Organic Solar Cells

A Thesis
Presented to
The Academic Faculty

by

Khanh Do

In Partial Fulfillment
of the Requirements for the Degree
Doctor of Philosophy in the
School of Chemistry and Biochemistry

Georgia Institute of Technology
August 2016

Molecular Simulations of the Bulk-Heterojunction Morphology in Organic Solar Cells

Approved by:

Dr. C. David Sherrill, Advisor
School of Chemistry and Biochemistry
Georgia Institute of Technology

Dr. Jean-Luc Bredas, Advisor
Physical Science and Engineering Division
King Abdullah University of Science and Technology
School of Chemistry and Biochemistry
Georgia Institute of Technology

Dr. Seth R. Marder
School of Chemistry and Biochemistry
Georgia Institute of Technology

Dr. Seung Soon Jang
School of Materials Science and Engineering
Georgia Institute of Technology

Dr. Kenneth R. Brown
School of Chemistry and Biochemistry
Georgia Institute of Technology

Date Approved: 6/12/16

To my parents,
Phuc Do and Nhung Tran,
who endured the cruelty of war and the drudgery of blue-collar labor
so that my brothers and I could have comfortable lives.

ACKNOWLEDGEMENTS

First and foremost, I would like to thank my Ph.D. advisor, Professor Jean-Luc Bredas, for his gracious support throughout my graduate studies and for showing me the enormous value in effectively communicating complex scientific ideas in clear and simple terms so that a general audience can understand.

I would like to thank my colleague and friend, Sean M. Ryno, for his friendship and technical assistance throughout my graduate studies.

I would also like to thank Daniel P. Mahoney for his friendship as we weathered the emotional struggles accompanied with the grind of graduate school and the process of becoming men.

Thank you to Professors Adam J. Moule and David M. Huang, who during my undergraduate studies, introduced me to the field of organic solar cells and invested their time in training me to become a scientist.

Thank you to my thesis committee members: Professors C. David Sherrill, Seth Marder, Seung Soon Jang and Ken Brown.

I appreciate the technical education and camaraderie I have received from the members of the Bredas group, most notably, Brad Rose, Mahesh Ravva, Veaceslav Coropceanu, Chad Risko, Hong Li, Paul Winget, Yao-Tsung, Stephen Shiring, Alexander Hyla, Rajesh Tummala, and Gjergji Sini. Also, thanks to Dawn Franklin and Sarah Truman for the administrative assistance.

Finally, thank you to Derek Le, Crystal Bradley, Ehson Nasir, Mauricio Gutierrez Arguedas, Ryan Josefsberg, Tuan Do, and Chuong Do for their support and companionship.

TABLE OF CONTENTS

LIST OF TABLES

LIST OF FIGURES

LIST OF SYMBOLS AND ABBREVIATIONS

OSCs	Organic Solar Cells
OPV	Organic Photovoltaic
OFETs	Organic Field-Effect Transistors
BHJ	Bulk-Heterojunction
HOMO	Highest Occupied Molecular Orbital
LUMO	Lowest Unoccupied Molecular Orbital
IP	Ionization Potential
EA	Electron Affinity
S_0	Singlet Ground State
S_1	Lowest Singlet Excited State
ET	Energy Transfer
CT	Charge Transfer
CS	Charge Separation
E_{opt}	Optical Gap
EQE	External Quantum Efficiency
J_{SC}	Short-Circuit Current Density
V_{OC}	Open-Circuit Voltage
FF	Fill Factor
PCE or η	Power Conversion Efficiency
HF	Hartree-Fock
DFT	Density Functional Theory

B3LYP	Becke 3-Parameter, Lee-Yang-Parr Hybrid Functional
ωB97X-D	Long-Range Corrected Hybrid Functional with Becke97 Exchange-Correlation Functional and Grimme's D2 Dispersion Model
MD	Molecular Dynamics
CG	Coarse-Grained
IBI	Iterative Boltzmann Inversion
OPLS-AA	All-Atom Optimized Potentials for Liquid Simulations
NVT	(Constant) Number of Atoms, Volume, Temperature
NPT	(Constant) Number of Atoms, Pressure, Temperature
MSD	Mean Square Displacement
RDF or $g(r)$	Radial Distribution Function
OCF	Orientational Correlation Function
SCLC	Space-Charge-Limited Current
t	Electronic Coupling or Transfer Integral
D	Translational Diffusion Coefficient
α	Orientational Diffusion Coefficient
τ_2	Chain Relaxation Time
$\overline{\psi}_n$	Demixing Parameter
R_g	Radius of Gyration
λ	Reorganization Energy
W	Electronic Band Width
m_{eff}	Effective Mass

SUMMARY

In this Thesis, we aim to elucidate clear connections between the chemical functionality and molecular morphologies of a number of high-performing or benchmark π-conjugated materials used in organic solar cells (OSCs). We proceed to link these structural features to electronic properties that are important to photovoltaic performance. This Thesis is organized into three themes, in each of which we investigate a particular component of the chemical functionality of a specific π-conjugated material and its effects on thin-film molecular packing:

- Fluorine substitution in a polymer donor (Chapter 3) and hole-transport molecular crystal (Chapter 6)
- Electron-withdrawing group and alkyl group substitution in a nonfullerene acceptor (Chapter 4)
- Modification of the core π-conjugated motif in a nonfullerene acceptor (Chapter 5)

The results from studying these specific systems showcase the utility of computer simulations, which when used in tandem with experiment can build a molecular understanding of the bulk-heterojunction (BHJ) morphology for OSC applications. While the parameter space of the materials studied in this Thesis remains limited, it does provide a rigorous starting point to developing a more comprehensive understanding of the structure-morphology-performance relationships in π-conjugated systems, which are necessary to systematically improve performance.

Chapter 1

Organic Bulk-Heterojunction Solar Cells

1.1 Introduction and Scope

The world today urgently needs clean energy. The transition away from fossil fuels is not prompted by any critical shortage of resources, but rather mandatory for the preservation of our planet. While we have enough coal for roughly 2000 years, natural gas for 200-600 years, and oil for at least 50-150 years,[1] we cannot afford to continue pumping CO_2, a greenhouse gas, into the atmosphere. There has been shown a clear correlation between atmospheric CO_2 concentrations and average global temperatures, with strong evidence linking it to anthropogenic activities since the Industrial Revolution.[2,3] Higher temperatures are expected to harm the equilibrium state of our planet, including its climate and biodiversity. There is thus a rational imperative for our society to move towards using carbon-free renewable energy sources. However, for renewable and clean energy technologies to make a real impact to the global energy mix, they must have the potential to reach the single and double digits of terawatt capacity.[4]

Solar photovoltaics is currently a front-runner and arguably the most promising candidate to accomplish this grand challenge in the not-too-distant future, with solar panels based on crystalline silicon (a "first generation" technology) currently leading the way.[4] In this Thesis, we focus on a third-generation technology: organic solar cells (OSCs) [Figure 1.1]. We highlight here some of their advantages, which make them a promising candidate to contribute to the global energy mix in the future[5]:

- Their active materials are organic and consist of earth-abundant elements: carbon, hydrogen, nitrogen, sulfur, silicon, etc.
- They have the potential for low-cost, large-area, high-throughput, and roll-to-roll production due to the solution processability of its active materials at low temperatures.

- They are mechanically lightweight and flexible, allowing for integration into both small-scale (portable electronic devices) and large-scale (building architectures) applications.
- The synthetic techniques used to tailor the properties of their active materials are highly versatile owing to the vast repertoire of organic chemistry.

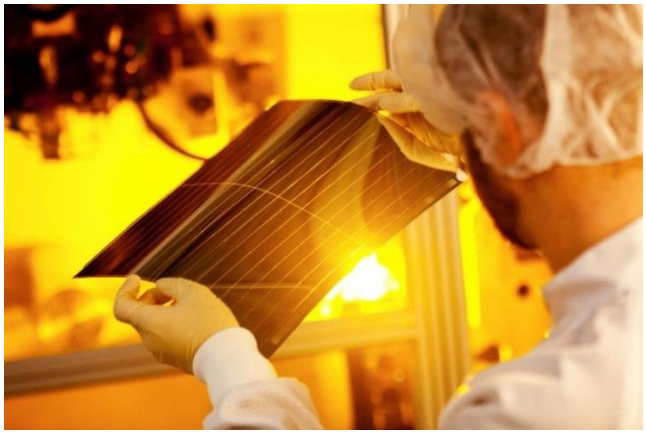

Figure 1.1 Demonstration modules for organic solar cells from the German company Heliatek.[6]

The list of pros above demonstrates the potential applications of OSCs. However, several important breakthroughs must be achieved before they can make a real impact, such as improving material stability, device performance and lifetime, and production scalability. The scope of this Thesis focuses on improving solar cell efficiency, paying particular attention to the optimization of the active layer morphology. To that end, we aim to build a molecular understanding of the relationships between the chemical functionality of the active materials, their thin-film morphologies, and performance properties using theoretical and computational methodologies. We begin our endeavor by first reviewing the properties of the active materials

and their device physics. Then, we examine the methodologies that are routinely used for characterizing the morphology and performance, while underlining the currently incomplete understanding of the structure-property relationships for BHJ solar cells. Finally, we explain our rationale for using theoretical and computational methodologies to develop that molecular understanding.

1.2 Materials and Device Physics

In OSCs, the active materials consist of organic semiconductors, which are used to absorb sunlight and generate electricity. Organic semiconductors are carbon-based π-conjugated systems ranging from small molecules to oligomers and polymers, which are usually classified into two categories: donor (electron rich) (D) and acceptor (electron poor) (A). In the framework of molecular orbital theory, a donor has frontier orbitals – HOMOs and LUMOs (highest occupied and lowest unoccupied molecular orbitals respectively) – that are energetically higher than those of an acceptor; thus the labels "donor" and "acceptor" are relative terms. The offsets between the frontier molecular orbital energy levels of the donor and acceptor induce a driving force for charge transfer and separation, which are the essential processes required in any solar cell. More rigorously, the ionization potential (IP) and electron affinity (EA) should be used instead of the HOMO and LUMO levels, respectively, because the latter stems from a one-electron picture only. Organic semiconductors differ from most of their inorganic counterparts in that they can be readily deposited to form thin films from solution using common organic solvents, including some of those that are environmentally friendly.[7] This solution processability at low temperatures is at the heart of their potential cost-effectiveness at the production stage. In

addition, their molecular properties such as redox potentials, optoelectronic properties, and solubilities can be readily tuned or influenced through organic chemistry techniques.

In its most basic components, an OSC consists of an active layer deposited between two electrodes having different Fermi levels so as to induce a built-in electric field for collecting charge carriers. The earliest devices employed a bilayer architecture comprising of adjacent donor and acceptor layers. The current understanding of the operating processes in a bilayer OSC (Figure 1.2) is described as follows[8]: (i) When light shines on a cell, photons can be absorbed ($S_0 \rightarrow S_1$) by either component material depending on its absorption profile and the wavelength of light. The photon absorption generates relatively localized excited states called excitons, which are electrically neutral, bound electron-hole pairs usually of singlet spin multiplicity.[5] (ii) The excitons diffuse throughout the active layer via energy transfer (ET) and (iii) can dissociate at the donor-acceptor interface, where electron transfer occurs and charge-transfer (CT) states are formed. This "interface" can range from a bimolecular complex to a discrete junction where the former is characteristic of a highly intermixed system and the latter corresponds to a highly phase-separated system. (iv) The CT states can proceed to charge-separated (CS) states leading to "free" electrons and holes that can be transported to and collected at their corresponding electrodes due to the built-in electric field.

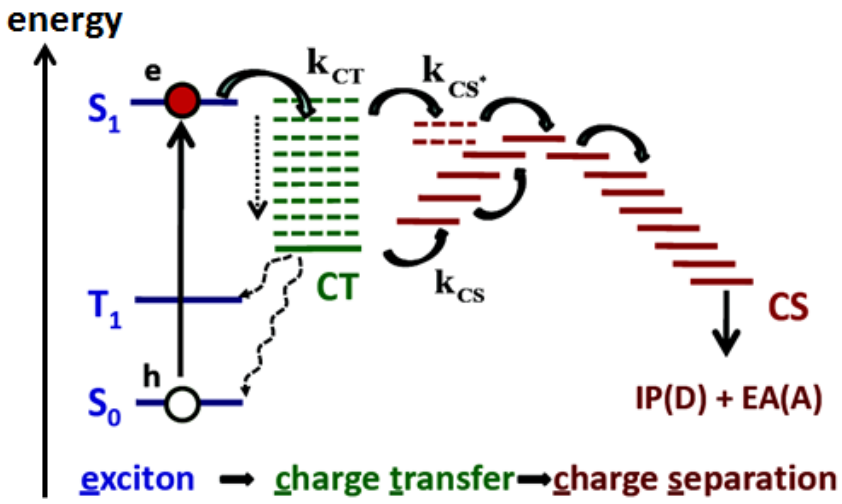

Figure 1.2 State energy diagram depicting the operating processes in an organic solar cell.[8]

For each of the processes described above, there is unfortunately a loss mechanism associated[5]: Excitons can relax radiatively back to the ground state before reaching the donor-acceptor interface; CT states can transition to triplet states via intersystem crossing, which can then relax non-radiatively back to the ground state; and finally, electrons and holes can recombine into excitons and decay to the ground state, which can occur either directly following charge transfer (geminate recombination) or after charge separation with the charge carriers originating from different excitons (bimolecular recombination). It is thus imperative to optimize the efficiency of each of these processes in order to maximize the solar cell efficiency. The most significant improvement, from a design standpoint, is to transition to a bulk-heterojunction (BHJ) architecture[9,10] whereby a blend solution is deposited to form an interpenetrating network of donor and acceptor domains in thin film due to the inherently limited miscibility of the component materials (see Figure 1.3). The BHJ architecture solves the primary issue of having a short exciton diffusion length (~10-20 nm) [the average distance an exciton diffuses before

relaxing back to the ground state], which wastes excitons formed too far from the donor-acceptor interface. For that reason, it has become the standard architecture of choice for achieving state-of-the-art efficiencies in OSCs, with record efficiencies of 11.7% and 7.7% for polymer:fullerene[7] and all-polymer devices,[11] respectively. While the adoption of the BHJ architecture has led to much higher efficiencies compared to those of bilayer devices, the task of controlling the active layer morphology has also become significantly more challenging due to the large parameter space involved in the device fabrication process.

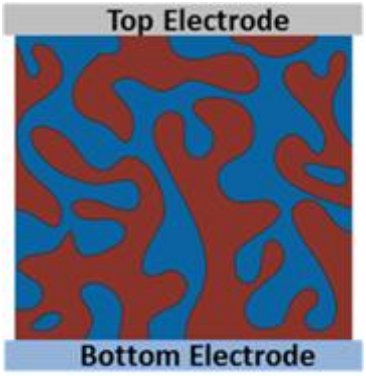

Figure 1.3 Schematic diagram of a bulk-heterojunction solar cell.

While there is currently a good understanding of how one can tune the molecular properties (particularly frontier energy levels) of π-conjugated materials by tailoring their chemical structures,[12] there is still an incomplete understanding of how chemical functionality affects thin-film morphology for both the pristine and blended systems, at least not with molecular resolution. And yet, optimizing the thin-film morphology is arguably *the* determining factor in maximizing solar cell efficiency as it affects both the voltage and current of the device. As we

shall see, controlling the BHJ morphology is inherently challenging as the parameter space includes, for example, the functionality and molecular weight[13] of the active materials, the blend ratio, the processing solvent and additives,[14] the deposition method, and the thermal[15] and solvent annealing methods. In the next Section, we will review a number of methods that are routinely used to characterize the BHJ morphology and optimize the various device parameters of an OSC.

1.3 Current Methods of Morphology Characterization and Performance Optimization

In this Section, we highlight that while there are a number of techniques available to control and characterize the BHJ morphology, in most cases, a molecular picture of the morphology and a thorough understanding of how it affects the performance properties remains incomplete.

Morphology characterization techniques

We begin by discussing the characterization of molecular properties, for in the process of architecting new active materials, this is where chemists have most control. The molecular properties that are typically modulated for photovoltaic purposes include absorption profiles, optical gaps (E_{opt}), ionization potentials (IPs), and electron affinities (EAs) through the use of electron-donating and electron-withdrawing groups. Solubilities are primarily influenced through the use of pendant alkyl side groups or chains. Absorption profiles and optical gaps can be determined by UV/vis spectroscopy; IPs can be determined by ultraviolet photoelectron spectroscopy (UPS); and EAs can be approximated from the solution-phase reduction potentials of cyclic voltammetry or via inverse photoemission spectroscopy (IPES).[16]

Moving to the characterization of thin films, a qualitative or semi-quantitative view of the BHJ morphology can be obtained from atomic force microscopy (AFM),[14] transmission electron microscopy (TEM),[13] and tomography[17] images. The micrographs can reveal whether the morphology is amorphous or nanocrystalline, highly intermixed or phase-separated. Differential scanning calorimetry has been useful for mapping out phase diagrams and miscibility. The degree of crystallinity present in the thin film can be measured using X-ray diffraction (XRD) or grazing incidence wide-angle X-ray scattering (GIWAXS) methods.[18,19] These diffraction and scattering methods can reveal the π-stacking and lamellar distances in sufficiently ordered polymeric systems. For lower-order systems such as those exhibiting liquid-crystallinity, the orientation of domains down to 10 nm resolution can be measured from the resonant scattering of polarized soft X-rays (P-SoXS).[20] Recently, solid-state nuclear magnetic resonance (SS-NMR) techniques have become increasingly used to determine solid-state conformations and molecular packing in tandem with molecular modeling.

Current understanding of performance optimization

We now turn our attention to the characterization of the solar cell performance, which is primarily measured by the current-voltage (*J*-*V*) curve (Figure 1.4). The maximum power generated by a cell is determined by the maximum output voltage (V_{max}) and current (J_{max}), which can be related to its open-circuit voltage (V_{OC}) and short-circuit current density (J_{SC}) by the fill factor (*FF*), see Equations 1.1-1.2.

$$\eta = \frac{J_{SC} V_{OC} FF}{P_{in}} \tag{1.1}$$

$$FF = \frac{J_{max} V_{max}}{J_{SC} V_{OC}} \tag{1.2}$$

Thus, to maximize the power conversion efficiency (η), one needs to optimize the three parameters: J_{SC}, V_{OC}, and FF. This task, however, is not straightforward as the factors that affect the current and those affecting the voltage are often mutually counteracting.

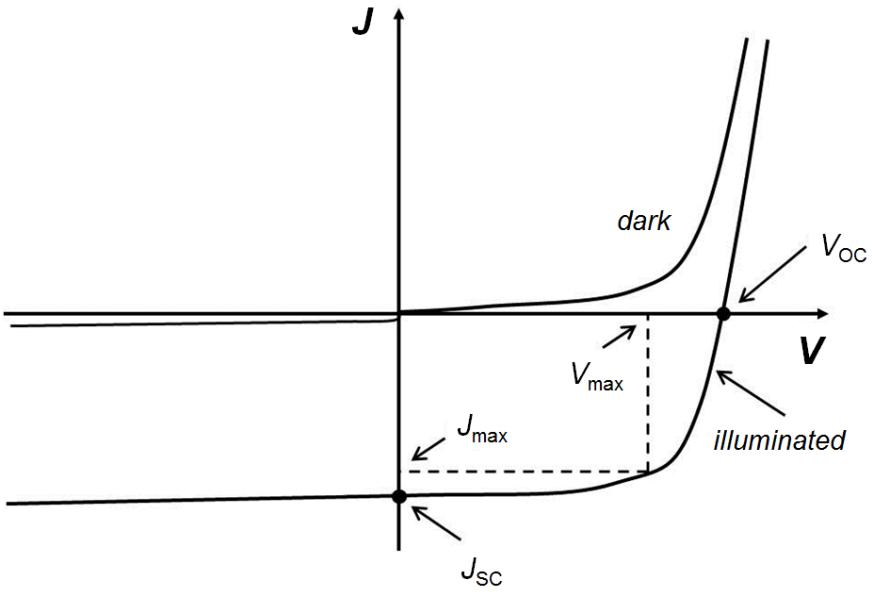

Figure 1.4 Schematic of a typical *J*-*V* curve for an illuminated solar cell.

For instance, the J_{SC} can be amplified by using active materials with small optical gaps and broad absorption profiles within the solar spectrum.[21] However, this comes at the expense of the V_{OC} due to having a smaller photovoltaic gap (energy difference between the donor IP and acceptor EA) and lower CT state energies, both of which have been shown to correlate with the V_{OC}.[22,23] The task of optimizing the efficiency is further complicated by having to control the intricate nanoscale details of the BHJ morphology. For example, it has been shown that reducing the interfacial area leads to higher V_{OC} as a result of reduced charge recombination.[24] However, a

smaller interfacial area also leads to diminished charge dissociation in the first place (hence the move away from a bilayer architecture). Moreover, the nature of the interfacial D-A configurations is also expected to play a crucial role in charge generation and recombination.[25–27] Thus, the optimization of the solar cell efficiency is difficult in practice and requires a delicate balancing act among a number of competing factors.

1.4 Using Computer Simulations for Studying Molecular Morphology

As we have seen, the formation of the BHJ morphology is governed by a large parameter space. Though a number of experimental techniques exist for probing some aspects of the BHJ morphology, many of them are indirect, qualitative, and do not have nanoscale resolution. Thus, in order to link the structural and morphological features of the bulk-heterojunction to its performance properties, a clearer picture of the molecular packing is required. To this end, theoretical and computational methodologies can be extremely effective given that all atomic coordinates take known values in a calculation or simulation. This helps to minimize ambiguity when making structure-property correlations, especially when used in tandem with experimental morphology and performance characterizations. Moreover, understanding the precise molecular packing behavior in the pure donor and acceptor phases and their mixed phases is of the utmost importance given that the transfer, dissociation, separation, and transport of charge carriers are all predicated on the nature of these phases and their prevalence in the active layer. Having a clearer and more concrete picture of the structural and electronic features of the BHJ morphology will allow us to rigorously point to structure-morphology-performance relationships.

1.5 Thesis Objective and Outline

In this Thesis, we aim to elucidate clear connections between the chemical functionality and molecular morphologies of a number of high-performing or benchmark π-conjugated materials used in OSCs. We proceed to link these structural features to electronic properties that are important to solar cell performance. This Thesis is organized into three themes, in each of which we investigate a particular component of the chemical functionality of a specific π-conjugated material and its effects on thin-film molecular packing:

- Fluorine substitution in a polymer donor (Chapter 3) and hole-transport molecular crystal (Chapter 6)
- Electron-withdrawing group and alkyl group substitution in a nonfullerene acceptor (Chapter 4)
- Modification of the core π-conjugated motif in a nonfullerene acceptor (Chapter 5)

The results from studying these specific systems showcase the utility of computer simulations, which when used in tandem with experiment can build a molecular understanding of the BHJ morphology for OSC applications. While the parameter space of the materials studied in this Thesis remains limited, it does provide a rigorous starting point to developing a more comprehensive understanding of the structure-morphology-performance relationships in π-conjugated systems, which are necessary to systematically improve performance.

1.6 References

(1) Lewis, N. S. *MRS Bull*. **2007**, *32* (10), 808.
(2) Fifth Assessment Report - Climate Change 2013 http://www.ipcc.ch/report/ar5/wg1/ (accessed Mar 13, 2016).
(3) US EPA, C. C. D. Causes of Climate Change http://www3.epa.gov/climatechange/science/causes.html (accessed Mar 13, 2016).
(4) Tao, M. *Terawatt Solar Photovoltaics*; SpringerBriefs in Applied Sciences and Technology; Springer London: London, 2014.
(5) Tress, W. *Organic Solar Cells*; Springer Series in Materials Science; Springer International Publishing: Cham, 2014; Vol. 208.
(6) Heliatek | organic based photovoltaics– The future is light http://www.heliatek.com/en/ (accessed Apr 17, 2016).
(7) Zhao, J.; Li, Y.; Yang, G.; Jiang, K.; Lin, H.; Ade, H.; Ma, W.; Yan, H. *Nat*. *Energy* **2016**, *1* (2), 15027.
(8) Brédas, J.-L.; Norton, J. E.; Cornil, J.; Coropceanu, V. *Acc*. *Chem*. *Res*. **2009**, *42* (11), 1691.
(9) Halls, J. J. M.; Walsh, C. A.; Greenham, N. C.; Marseglia, E. A.; Friend, R. H.; Moratti, S. C.; Holmes, A. B. *Nature* **1995**, *376* (6540), 498.
(10) Yu, G.; Gao, J.; Hummelen, J. C.; Wudl, F.; Heeger, A. J. *Science* **1995**, *270* (5243), 1789.
(11) Hwang, Y.-J.; Courtright, B. A. E.; Ferreira, A. S.; Tolbert, S. H.; Jenekhe, S. A. *Adv*. *Mater*. **2015**, *27* (31), 4578.
(12) Nielsen, C. B.; Holliday, S.; Chen, H.-Y.; Cryer, S. J.; McCulloch, I. *Acc*. *Chem*. *Res*. **2015**, *48* (11), 2803.
(13) Brinkmann, M.; Rannou, P. *Macromolecules* **2009**, *42* (4), 1125.
(14) Moon, J. S.; Takacs, C. J.; Cho, S.; Coffin, R. C.; Kim, H.; Bazan, G. C.; Heeger, A. J. *Nano Lett*. **2010**, *10* (10), 4005.
(15) Swaraj, S.; Wang, C.; Yan, H.; Watts, B.; Lüning, J.; McNeill, C. R.; Ade, H. *Nano Lett*. **2010**, *10* (8), 2863.
(16) Bredas, J.-L. *Mater*. *Horiz*. **2013**, *1* (1), 17.
(17) Andersson, B. V.; Herland, A.; Masich, S.; Olle Inganäs. *Nano Lett*. **2009**, *9* (2), 853.
(18) Brady, M. A.; Su, G. M.; Chabinyc, M. L. *Soft Matter* **2011**, *7* (23), 11065.
(19) Rivnay, J.; Mannsfeld, S. C. B.; Miller, C. E.; Salleo, A.; Toney, M. F. *Chem*. *Rev*. **2012**, *112* (10), 5488.
(20) Collins, B. A.; Cochran, J. E.; Yan, H.; Gann, E.; Hub, C.; Fink, R.; Wang, C.; Schuettfort, T.; McNeill, C. R.; Chabinyc, M. L.; Ade, H. *Nat*. *Mater*. **2012**, *11* (6), 536.
(21) Jung, J. W.; Jo, J. W.; Jung, E. H.; Jo, W. H. *Org*. *Electron*. **2016**, *31*, 149.
(22) Vandewal, K.; Gadisa, A.; Oosterbaan, W. D.; Bertho, S.; Banishoeib, F.; Van Severen, I.; Lutsen, L.; Cleij, T. J.; Vanderzande, D.; Manca, J. V. *Adv*. *Funct*. *Mater*. **2008**, *18* (14), 2064.
(23) Vandewal, K.; Tvingstedt, K.; Gadisa, A.; Inganäs, O.; Manca, J. V. *Nat*. *Mater*. **2009**, *8* (11), 904.
(24) Vandewal, K.; Widmer, J.; Heumueller, T.; Brabec, C. J.; McGehee, M. D.; Leo, K.; Riede, M.; Salleo, A. *Adv*. *Mater*. **2014**, *26* (23), 3839.
(25) Tumbleston, J. R.; Collins, B. A.; Yang, L.; Stuart, A. C.; Gann, E.; Ma, W.; You, W.; Ade, H. *Nat*. *Photonics* **2014**, *8* (5), 385.

(26) Graham, K. R.; Cabanetos, C.; Jahnke, J. P.; Idso, M. N.; El Labban, A.; Ngongang Ndjawa, G. O.; Heumueller, T.; Vandewal, K.; Salleo, A.; Chmelka, B. F.; Amassian, A.; Beaujuge, P. M.; McGehee, M. D. *J*. *Am*. *Chem*. *Soc*. **2014**, *136* (27), 9608.
(27) Vandewal, K.; Tvingstedt, K.; Gadisa, A.; Inganäs, O.; Manca, J. V. *Phys*. *Rev*. *B* **2010**, *81* (12), 125204.

Chapter 2

Theoretical and Computational Methodologies

2.1 Density Functional Theory

In this work, the computational methodology with the highest level of accuracy is density functional theory (DFT), which we used to determine the electronic structure of many hundreds to a thousand medium-sized molecular systems, each consisting of a few hundred atoms. DFT can give a good to excellent description of the electronic structure of a molecular system in a feasible amount of time given a proper density functional, which usually has been chosen to reproduce a set of properties for a variety of molecules. Here, we used the functionals B3LYP and ωB97X-D, which will be discussed in details below. First, we will present the theoretical framework of DFT (with Hartree-Fock theory along the way) before discussing the various types of density functionals. Finally, we give a rigorous definition for the electronic coupling (also known as the transfer integral) and explain why it is an appropriate parameter in describing the charge transfer and transport processes in π-conjugated systems.

The Schrödinger equation

A main objective in quantum chemistry is to solve the time-independent Schrödinger equation for an atomic or molecular system consisting of many electrons.[1] The terms in the Hamiltonian (Equation 2.1) include the operators for the kinetic energy of the electrons (1) and nuclei (2), the Coulomb attraction between the electrons and nuclei (3), and the repulsion among the electrons (4) and among the nuclei (5); these terms are given in atomic units where the electron mass, reduced Planck's constant, and electron charge take unit values ($m_e = \hbar = e = 4\pi\varepsilon_0 = 1$).

$$\left\{ -\sum_{i=1}^{N} \frac{1}{2} \nabla_i^2 - \sum_{A=1}^{M} \frac{1}{2M_A} \nabla_A^2 - \sum_{i=1}^{N} \sum_{A=1}^{M} \frac{Z_A}{r_{iA}} + \sum_{i=1}^{N} \sum_{j>i}^{N} \frac{1}{r_{ij}} + \sum_{A=1}^{M} \sum_{B>A}^{M} \frac{Z_A Z_B}{R_{AB}} - E \right\} \Psi = 0 \qquad (2.1)$$

The Schrödinger equation cannot be solved for multi-electron systems exactly due to the electron-electron repulsion terms, so we must obtain approximate solutions which we require to have good chemical accuracy and computational efficiency.

In the following, we will discuss the approximations used in obtaining solutions of the Schrödinger equation. The first of these is the Born Oppenheimer (BO) approximation, where the nuclear motions in Equation 2.1 are eliminated to obtain an electronic version (Equation 2.2) of the Schrödinger equation.

$$\left\{-\sum_{i=1}^{N}\frac{1}{2}\nabla_i^2-\sum_{i=1}^{N}\sum_{A=1}^{M}\frac{Z_A}{r_{iA}}+\sum_{i=1}^{N}\sum_{j>i}^{N}\frac{1}{r_{ij}}-E_{\text{elec}}\right\}\Psi_{\text{elec}}=0 \tag{2.2}$$

This approximation is based on the fact that the electrons are much lighter than the nuclei and therefore respond nearly instantaneously to nuclear motion. The electronic Schrödinger equation is solved for a fixed nuclear configuration $\{\mathbf{R}_A\}$ and therefore its solutions consisting of the electronic wavefunctions $\{\Psi_{\text{elec}}\}$ and energies $\{E_{\text{elec}}\}$ are parametrically dependent on the nuclear coordinates. In addition, Ψ_{elec} also depends explicitly on the 3*N* electronic coordinates $\{\mathbf{r}_i,...,\mathbf{r}_N\}$. Despite the simplification introduced by the BO approximation, it is not sufficient to solve Equation 2.2 exactly as the latter still includes multi-electron terms.

The Hartree-Fock equations

Another important approximation is the self-consistent field (SCF) method, such as the Hartree-Fock (HF) method, whereby Equation 2.2 is transformed into a set of *N* equations describing a system of *N* interacting electrons moving in an effective single-particle potential $v^{\text{HF}}(\mathbf{x})$, see Equation 2.3, where the variable **x** includes both spatial and spin coordinates. The HF potential

includes the Coulomb (J) and exchange (K) operators (Equations 2.4-2.5), which accounts for the interaction of an electron with all other electrons in a mean-field approach. Note that the K operator accounts for electron exchange in an exact way, therefore the term "Hartree-Fock exchange" is synonymous to "exact exchange."

$$\left\{-\frac{1}{2}\nabla_1^2 - \sum_{A=1}^{M}\frac{Z_A}{r_{1A}} + v_a^{\mathrm{HF}}(\mathbf{x}_1) - \varepsilon_a\right\}\chi_a(\mathbf{x}_1) = 0 \tag{2.3}$$

$$v^{\mathrm{HF}}(\mathbf{x}_1) = \sum_b J_b(\mathbf{x}_1) - K_b(\mathbf{x}_1)$$

$$J_b(\mathbf{x}_1)\chi_a(\mathbf{x}_1) = \left[\int d\mathbf{x}_2 \frac{|\chi_b(\mathbf{x}_2)|}{r_{12}}\right]\chi_a(\mathbf{x}_1) \tag{2.4}$$

$$K_b(\mathbf{x}_1)\chi_a(\mathbf{x}_1) = \left[\int d\mathbf{x}_2 \frac{\chi_b^*(\mathbf{x}_2)\chi_a(\mathbf{x}_2)}{r_{12}}\right]\chi_b(\mathbf{x}_1) \tag{2.5}$$

In the HF equations, the spatial portion of the spin orbitals $\{\chi_a\}$ [also called molecular orbitals (MOs)] are represented in terms of a basis set comprising of a finite set of atom centered functions which form linear combinations (Equation 2.6) to represent the MOs as vectors containing the expansion coefficients.

$$\varphi_\mu = \sum_{\nu=1}^{K} c_\nu^\mu \phi_\nu \tag{2.6}$$

The Hamiltonian is then represented as a matrix. The transformation of the HF equations (or any other self-consistent field problem) into linear algebra terms makes solving them much more computationally efficient. In the same vein, the basis functions typically take the form of Gaussians, which historically has made computing the integrals in the Hamiltonian more efficient. The results of *ab initio* calculations are obviously dependent on the basis set used, where larger ones typically give better accuracy.

In this work, we perform thousands of calculations and must strike a balance between using a sufficiently large basis set and keeping the calculations collectively feasible. Therefore, we opted to use the Pople double-zeta basis set, 6-31G(d,p). This basis includes one function for each core atomic orbital and two functions for each valence atomic orbital. The core orbitals contain 6 primitive Gaussians each while the valence orbitals contain 3 and 1 each. On top of that, a polarization function is added to each atom, allowing polarization of the electron clouds by adding a *p*-orbital for hydrogen and *d*-type orbitals for heavier atoms.

The solutions of the HF equations are solved iteratively and are exact with respect to the basis set used. The solutions yield a set of orthonormal spin orbitals $\{\chi_a\}$ and their corresponding energies $\{\varepsilon_a\}$. The Slater determinant (Equation 2.7) formed from these spin orbitals is called the HF ground-state wavefunction.[1]

$$\Psi_{\mathrm{HF}}(\mathbf{x}_1,\mathbf{x}_2,...,\mathbf{x}_N)=\frac{1}{\sqrt{N!}}\begin{vmatrix}\chi_1(\mathbf{x}_1) & \chi_2(\mathbf{x}_1) & \cdots & \chi_N(\mathbf{x}_1)\\ \chi_1(\mathbf{x}_2) & \chi_2(\mathbf{x}_2) & \cdots & \chi_N(\mathbf{x}_2)\\ \vdots & \vdots & \ddots & \vdots\\ \chi_1(\mathbf{x}_N) & \chi_2(\mathbf{x}_N) & \cdots & \chi_N(\mathbf{x}_N)\end{vmatrix}\equiv\left|\chi_1\ \chi_2\ \cdots\ \chi_N\right| \qquad (2.7)$$

As the HF equations are the result of applying the variational method to the Slater determinant, the HF ground-state energy (E_0^{HF}) is only an upper bound to the exact electronic ground-state energy (E_0) within the BO approximation, the difference being defined as the electron correlation energy $\left(E_{\mathrm{corr}}=E_0-E_0^{\mathrm{HF}}\right)$ [in the limit of a completely flexible basis set (HF limit)].[1,2]

The consequence of using a mean-field approach in describing electron-electron interactions is that the electrons cannot react instantaneously to each other's proximity and therefore the correlation of their motions is neglected. As a result, this error gives an electron

density that is too high at small distances and too low at large distances. Electron correlation can be taken into account by several post-Hartree-Fock methods such as configuration interaction (CI) and Møller-Plesset perturbation theory (MPPT).[1] While these methods can take into account electron correlation to varying degrees, they quickly become computationally expensive as the system size becomes large. CI and MPPT methods scale with N^5 and beyond (for orders higher than two in the case of MPPT; full CI scales with $N!$) while DFT scales with N^3, where N is the number of basis functions.[3]

The Kohn-Sham equations

In DFT, electron correlation (and exchange) effects are included without being hampered by too large computational costs. This is afforded by working with the electron density $n(\mathbf{r})$ instead of the spin orbitals $\{\chi_a\}$ in the Hamiltonian. This transition from wavefunction to electron density is supported rigorously by the two theorems of Hohenberg and Kohn (HK)[4]:

i. The ground-state energy from the Schrödinger equation is a unique functional of the electron density.[5]
ii. The electron density that minimizes the overall functional is the true electron density corresponding to the full solution of the Schrödinger equation.[5]

Applying these two theorems, one arrives at the Kohn-Sham (KS) equations[6] where the Hamiltonian is now solely in terms of the electron density (Equation 2.8). The KS equations represent a system of N non-interacting particles moving in an effective single-particle potential, $v_{\text{eff}}(\mathbf{r})$:

$$\left\{-\frac{1}{2}\nabla^2-\sum_{A=1}^{M}\frac{Z_A}{|\mathbf{r}-\mathbf{R}_A|}+v_{\text{eff}}(\mathbf{r})-\varepsilon_a\right\}\chi_a(\mathbf{x})=0 \tag{2.8}$$

$$v_{\text{eff}}(\mathbf{r})=v_{\text{H}}(\mathbf{r})+v_{\text{XC}}(\mathbf{r})$$

$$v_{\text{H}}(\mathbf{r})=\int d\mathbf{r}'\frac{n(\mathbf{r}')}{|\mathbf{r}-\mathbf{r}'|}$$

$$v_{\text{XC}}(\mathbf{r})=\frac{\delta E_{\text{XC}}(\mathbf{r})}{\delta n(\mathbf{r})}$$

The solutions of the KS equations are determined iteratively (like in the HF method) in the following steps[5]:

1. Pick a trial electron density $n(\mathbf{r})$.
2. Use the trial density and solve the KS equations to obtain the spin orbitals $\{\chi_a(\mathbf{x})\}$.
3. Determine the electron density from the spin orbitals: $n(\mathbf{r})=\sum_{a=1}^{N}|\chi_a(\mathbf{x})|$.
4. Check if the electron density has converged; if not, repeat steps 2-3.

The solutions of the KS equations yield the ground-state energy, shown in functional form in Equation 2.9.

$$E[n]=-\frac{1}{2}\sum_{a=1}^{N}\int d\mathbf{r}\chi_a^*(\mathbf{x})\nabla^2\chi_a(\mathbf{x})-\sum_{A=1}^{M}\int d\mathbf{r}\frac{Z_A}{|\mathbf{r}-\mathbf{R}_A|}n(\mathbf{r})+\frac{1}{2}\int d\mathbf{r}\int d\mathbf{r}'\frac{n(\mathbf{r})n(\mathbf{r}')}{|\mathbf{r}-\mathbf{r}'|}+E_{\text{XC}}[n] \tag{2.9}$$

The effects of electron exchange and correlation (XC) and the correction to the kinetic energy arising from the interacting nature of the electrons are collectively taken into account as a density functional, $E_{\text{XC}}[n(\mathbf{r})]$.[3] The HK theorems guarantee that an exact exchange-correlation

functional exists such that the overall functional gives an electron density that is the exact ground-state solution to the Schrödinger equation. However, the exact exchange-correlation functional is not yet known and developing better approximations to this functional is the main focus of the DFT community.

The SCF procedure to solve the KS equations above is straightforward and routinely implemented in many commercial and open-source software programs. The necessary inputs include the structure of the molecule, the density functional, and the basis set on which to represent the spin orbitals.

Density functionals

Many density functionals have been developed and mostly vary in their complexity in describing the exchange-correlation functional. In the simplest case, the local density approximation (LDA) describes the exchange-correlation energy as a function of the electron density $n(\mathbf{r})$ alone. Improving on this, the generalized gradient approximation (GGA) takes into account both $n(\mathbf{r})$ and its gradient Δn. Hybrid functionals are typically based on GGA and incorporate some contribution of exact (or Hartree-Fock) exchange. Density functionals typically fall under two categories: those that are based on numerical fitting procedures involving large molecular training sets and those that are derived from more fundamental principles of quantum mechanics.[3] In any case, the success of a density functional from a practical standpoint is measured by its accuracy in reproducing a large set of chemical properties for a large variety of molecules. These include bond lengths and angles, barrier heights, atomization energies, binding energies, ionization potentials, electron affinities, heats of formation, and several types of nonbonded interactions among others.[3] As mentioned earlier, the density functionals we used in

this work are B3LYP and the long-range corrected ωB97X-D, which we will discuss in that order.

B3LYP is a hybrid functional consisting of the Becke88 exchange functional,[7] the Lee-Yang-Parr correlation functional,[8] and a fraction of exact exchange.[9] The three parameters in the functional were determined by Becke via fitting to the so-called G1 molecule set.[10] Ref. 3 gives an excellent survey of the performances of DFT functionals with a special focus on B3LYP. In general, B3LYP performs well for structural properties of small molecules beyond those from G1. In particular, in the work of Riley et al., the functional gives a mean unsigned error (MUE) of 0.007 Å for bonds, 1.94° for angles, 0.22 eV for ionization potentials (IPs), and 0.15 eV for electron affinities (EAs) for a set of small organic molecules.[3,11] In this work, we used B3LYP mainly to optimize the geometries and calculate the electronic couplings and band structures of several pentacene-based molecular crystals.

Despite its success for small organic molecules, B3LYP has been shown to significantly overestimate torsion barriers for several extended π-conjugated systems,[12–14] which is a result of the functional's intrinsic electron self-interaction error, which leads to over-delocalization of the electron density and, as a result, over-stabilization of planar conformations. In general, the problem of excess electron delocalization and localization is common to standard (semilocal and global hybrids) DFT functionals and HF methods, respectively;[14] in standard DFT, the electron self-interaction (delocalization) error stems from the Coulombic self-repulsion of one-electron densities, while in the HF method, the localization error stems from the absence of static electron correlation. For these reasons, we chose the long-range corrected functional ωB97X-D[15] when studying molecules and oligomer chains that have extended π-conjugation pathways. In using ωB97X-D, we can minimize the (de)localization error by matching the energy of the HOMO of a

molecular system to its IP, which is a property obeyed by the exact functional.[16] The ω-value obtained in this matching procedure is referred to as the "IP-tuned" ω-value. Our rationale for using the ωB97X-D functional is three-fold: (i) to obtain a reliable description of the torsion profiles along extended π-conjugated systems; (ii) to obtain a robust description of the electronic structure with a balanced account of (de)localization effects; and (iii) to obtain an appropriate description of weak non-covalent interactions by explicit inclusion of empirical dispersion.

Electronic coupling

With the necessary inputs in hand, we can proceed to calculate the electronic structure of the systems of interest. Among the properties of interest to organic solar cells are the IP and EA, where the energy gap between the donor IP and the acceptor EA has been shown to correlate with the device V_{OC}. Another property of interest is the electronic coupling (or transfer integral), which is an important parameter in describing the charge transfer and transport mechanisms in organic semiconducting materials. Here, we follow the procedure to determine the electronic couplings by Valeev *et al*.,[17] which corrects for the case where the MO on different molecules are not orthogonal. The site energies and electronic coupling are shown in Equations 2.10 and 2.11, respectively, where e_1 and e_2 are the energies of the relevant MOs of molecule 1 and 2, respectively; S_{12} and J_{12} are the overlap and interaction energy, respectively, between the orbitals of molecules 1 and 2 in the dimer or molecular complex:

$$e_{1(2)}^{\text{eff}} = \frac{1}{2}\frac{(e_1+e_2)-2J_{12}S_{12} \pm (e_1-e_2)\sqrt{1-S_{12}^2}}{1-S_{12}^2} \tag{2.10}$$

$$J_{12}^{\text{eff}} = \frac{J_{12}-\frac{1}{2}(e_1+e_2)S_{12}}{1-S_{12}^2} \tag{2.11}$$

$$e_i = \langle \Psi_i | H | \Psi_i \rangle$$

$$J_{ij} = \langle \Psi_i | H | \Psi_j \rangle$$

$$S_{ij} = \langle \Psi_i | \Psi_i \rangle$$

All DFT calculations in this work were performed using the *Gaussian 09* code (Revisions C.01 and D.01).[18]

2.2 Atomistic Molecular Dynamics

While DFT methods can readily be used to determine the electronic and structural properties of single molecules and molecular complexes, they become computationally prohibitive or unfeasible when the system sizes approach 10-100 large molecules. To maneuver around this limitation, we turned to atomistic molecular dynamics (MD) simulations to study system sizes consisting of 50-250 molecules or polymer chains, which correspond to 5-10 nm or 25,000-30,000 atoms. MD simulations employ a force-field level of theory whereby only atomic nuclei are explicitly modeled and their dynamics are governed by simpler Newtonian mechanics with particles moving due to net forces. Electronic effects are averaged out and contained implicitly in the force field. Thus, in moving to MD simulations, the large electronic degrees of freedom are drastically reduced and as a result this allows us to study the molecular packing of bulk material systems. While some important electronic effects are not fully captured in this way, this is often acceptable when we are more interested in the local configurations of neighboring molecules.

Force fields

The main factor to consider when choosing a force field is the set of properties it was parameterized to accurately reproduce and the types of materials included in its training set. As we are interested here in studying the local structure and morphology of organic materials in thin films, we sought a force field that was parameterized to accurately reproduce the properties of condensed-phase organic molecules. The OPLS-AA (all-atom optimized potentials for liquid simulations) force field[19] developed by Jorgensen and co-workers has shown good performance for bulk properties such as density, compressibility, and heat capacity. However, the atomic partial charges are empirically derived and generalized, as are the bond lengths and angles. The description of dihedrals is from lower-level HF methods or DFT calculations at the B3LYP level. In light of these features, we proceeded to use the OPLS-AA force field as a starting point and updated as many parameters as practically feasible using DFT methods, which we will detail below. The OPLS-AA force field has the following analytical form (Equations 2.12-2.16):

$$E(r^N) = E_{\text{bonds}} + E_{\text{angles}} + E_{\text{dihedrals}} + E_{\text{nonbonded}} \tag{2.12}$$

$$E_{\text{bonds}} = \sum_{\text{bonds}} k_r (r - r_0)^2 \tag{2.13}$$

$$E_{\text{angles}} = \sum_{\text{angles}} k_\theta (\theta - \theta_0)^2 \tag{2.14}$$

$$E_{\text{dihedrals}} = \sum_{\text{dihedrals}} \left(\frac{V_1}{2}\left[1 + \cos\left(\phi - \phi_1\right)\right] + \frac{V_2}{2}\left[1 - \cos\left(\phi - \phi_2\right)\right] + \frac{V_3}{2}\left[1 + \cos\left(3\phi - \phi_3\right)\right] \right) \tag{2.15}$$

$$E_{\text{nonbonded}} = \sum_{j>i} f_{ij} \left(\frac{A_{ij}}{r_{ij}^{12}} - \frac{C_{ij}}{r_{ij}^{6}} + \frac{q_i q_j e^2}{4\pi\varepsilon_0 r_{ij}} \right) \tag{2.16}$$

Bond lengths and angles are described by harmonic potentials; dihedrals are described by a third-order cosine function (sometimes fourth-order); electrostatic interactions are described by the

Coulomb potential between partial atomic charges; and van der Waals interactions are governed by the 6-12 Lennard-Jones potential. The nonbonded interactions are scaled to 0 and 1/2 their original values if the atoms are separated by one and two bonds, respectively.

In our procedure for updating the force-field parameters, we took values from the bonds and angles of the geometry-optimized molecules as determined from DFT calculations at the B3LYP or ωB97X-D level. The force constants of the OPLS stock values were retained. The dihedral parameters corresponding to inter-monomer or inter-ring bonds were updated by obtaining a torsion profile about the inter-ring bond at the ωB97X-D/6-31G(d,p) DFT level and optimizing the parameters such that the corresponding dihedral distribution yielded the same profile as the DFT profile when approximated as a free energy in a range of finite temperatures. The reader is referred to Ref. 20 for a detailed demonstration of this procedure.[20] Finally, the partial atomic charges were updated using the ESP (electrostatic potential) method where charge values are fitted to reproduce the molecular electrostatic potential around the molecule.[21,22]

Running simulations

With the modified force field built, we sampled phase space via dynamics using the velocity-Verlet algorithm shown in Equations 2.17-2.18:

$$\mathbf{x}(t+\Delta t) = \mathbf{x}(t) + \mathbf{v}(t)\Delta t + \frac{1}{2}\mathbf{a}(t)\Delta t^2 \tag{2.17}$$

$$\mathbf{v}(t+\Delta t) = \mathbf{v}(t) + \frac{\mathbf{a}(t)+\mathbf{a}(t+\Delta t)}{2}\Delta t \tag{2.18}$$

In this work, the simulations were performed in either the NVT (constant volume) or NPT (constant pressure) ensembles using a Nosé-Hoover thermostat[23] and barostat[24] to keep the temperature and pressure constant, respectively. In the case of a triclinic simulation box when

studying crystal systems, the Parinello-Rahman barostat was used instead to handle the triclinic symmetry of the simulation box.[25] The vibration frequencies of C-H bonds are much faster than the typical integration time steps (1.0-2.0 fs) used in atomistic MD simulations, which allows us to keep them fixed with negligible loss in accuracy. For this purpose, the SHAKE algorithm[26] was used to constrain C-H bonds with fixed length. In MD simulations, nonbonded interactions are usually separated into short-range (SR) and long-range (LR) parts, where they are treated explicitly in the SR part and either omitted or approximated in the LR part. In our work, the LJ potentials were truncated at a distance of 12 Å and shifted to zero. For the Coulombic potentials, the cut-off distance was also 12 Å with the remaining tail of the potential being approximated using the Particle-Particle Particle-Mesh (PPPM) method of Hockney and Eastwood.[27]

The initial configurations of our simulations were either random when studying amorphous systems in the melt or based on the structure of a super cell when studying crystalline systems. In both cases, periodic boundary conditions were enforced. For the first case, the simulations were performed at elevated temperatures (550-650 K) corresponding to the melt. Our rationale for sampling the configurational space corresponding to this temperature range was to obtain enough sampling in a feasible amount of time due to the elevated temperatures while also capturing the configurational space that is representative of the solid state. As a guide, we used the chain or molecular relaxation time τ_2 to determine how long to run the simulation, which was typically 3-6 times τ_2. The relaxation time is obtained by fitting the auto-correlation function of a unit vector $\mathbf{u}(t)$ between the ends of a chain or molecular backbone to the equation $\left\langle P_2[\mathbf{u}(t)\cdot\mathbf{u}(0)]\right\rangle \approx \exp\left(-t/\tau_2\right)$, where $P_2(x) \equiv \left(3x^2-1\right)/2$ is the second-order Legendre polynomial.

The output of an MD simulation is the trajectory of all the atoms. With these atomic coordinates, we can analyze the structural and dynamical properties of the system. Below is a list of the most basic values, functions, and distributions that can be computed from the trajectory of an MD simulation. We will use these quantities in this Thesis to compare the structural order among different material systems.

- ***Density*:** The density of a material is usually the simplest property to reproduce correctly. From an MD simulation, the density can be readily determined by dividing the mass of the system by its average volume.
- ***Mean square displacement (MSD)*:** The translational diffusion coefficient D for molecules in the melt can be determined by computing the MSD and relating it to the expression: $\left\langle r^2(t) \right\rangle \approx 6Dt$.
- ***Radial distribution function (RDF)*:** The RDF or $g(r)$ measures the probability of finding a particle some distance away from a reference particle. In other words, it measures the local density of the system, where $g(r)$ approaches the global density (unity) at large distances.
- ***Orientational correlation function (OCF)*:** The OCF measures the spatial correlation between two vectors that can be defined to represent any physical portion of the molecular system such as the backbone of a polymer chain or its alkyl side chains.
- ***Structural distribution functions*:** These distributions are simply the probability distributions of finding the molecule with a specific bond length, bond angle, dihedral angle, or intermolecular packing distance. Examples are shown in Figure 2.1.

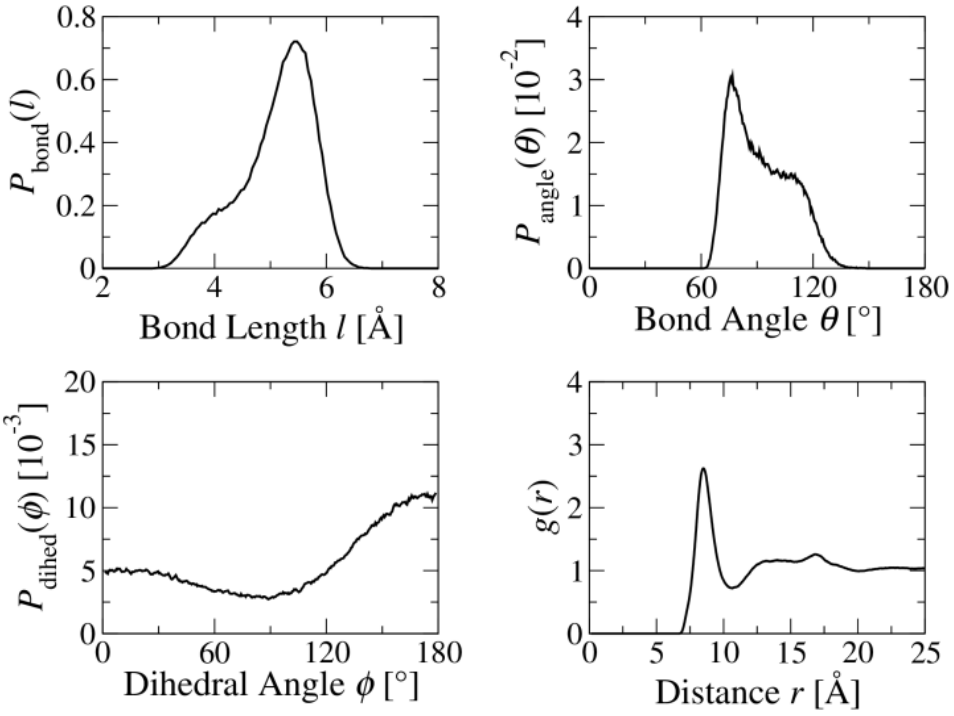

Figure 2.1 Examples of the kinds of structural distribution functions that can be computed from an MD simulation trajectory. The system of interest is a PBDT[2F]T:PCBM blend.

2.3 Coarse-Grained Molecular Dynamics

In the previous Section, we discussed how DFT results can be used to parameterize force fields for atomistic MD simulations. We noted that in moving to force fields, we can simulate much larger systems. In the same vein, even larger systems can be simulated when moving to coarse-grained (CG) simulations, albeit at the cost of atomistic resolution. While atomistic MD simulations can handle system sizes on the order of 10^4 atoms, CG simulations can handle 10^5-10^6 "super atoms" that represent tens of millions of atoms. In the coarse-graining procedure, we simplify the system by turning groups of atoms into "super atoms," taking their centers-of-mass as the new coordinates. Then, we derive a set of potentials such that when we apply them to the super atoms, the resulting structural distributions matches those from the atomistic MD

simulations.[28] The derivation of the CG potentials is distribution-based and is called the iterative Boltzmann inversion (IBI) method.[28] In Equation 2.19, a CG potential is iteratively updated until it reproduces the target structural probability distribution $P_{\text{target}}(x)$, where x is any structural variable such as the bond length l, bond angle θ, dihedral angle ϕ, or nonbonded distance r. The parameter a_i is used to control the rate of convergence of the iterative procedure, k_{B} is the Boltzmann constant, and T is the absolute temperature. The initial potential to start the iteration cycle is shown in Equation 2.20. Once all the potentials have converged, the nonbonded interactions are scaled linearly following Equation 2.21 so the volume (and hence density) of the system is reproduced when performing the simulation in the NPT ensemble.

$$U_{i+1}(x) = U_i(x) + a_i k_{\text{B}} T \ln\left[\frac{P_i(x)}{P_{\text{target}}(x)}\right] \tag{2.19}$$

$$U_0(x) = -k_{\text{B}} T \ln\left[P_{\text{target}}(x)\right] \tag{2.20}$$

$$\Delta U_{jk}(r) = b_{jk}\left(1 - \frac{r}{r_{\text{cut}}}\right), \qquad r \le r_{\text{cut}} \tag{2.21}$$

Figure 2.2 shows examples of the goodness-of-fit between the structural distributions from the CG simulations and those from the atomistic MD simulations, which is excellent to within thermal fluctuations. All MD and CG simulations were performed using the open-source *LAMMPS* simulation package.[29] Many of the calculations and simulations here were carried out using the computing resources at the King Abdullah University of Science and Technology,[30] with the remaining portion at the Georgia Institute of Technology.[31]

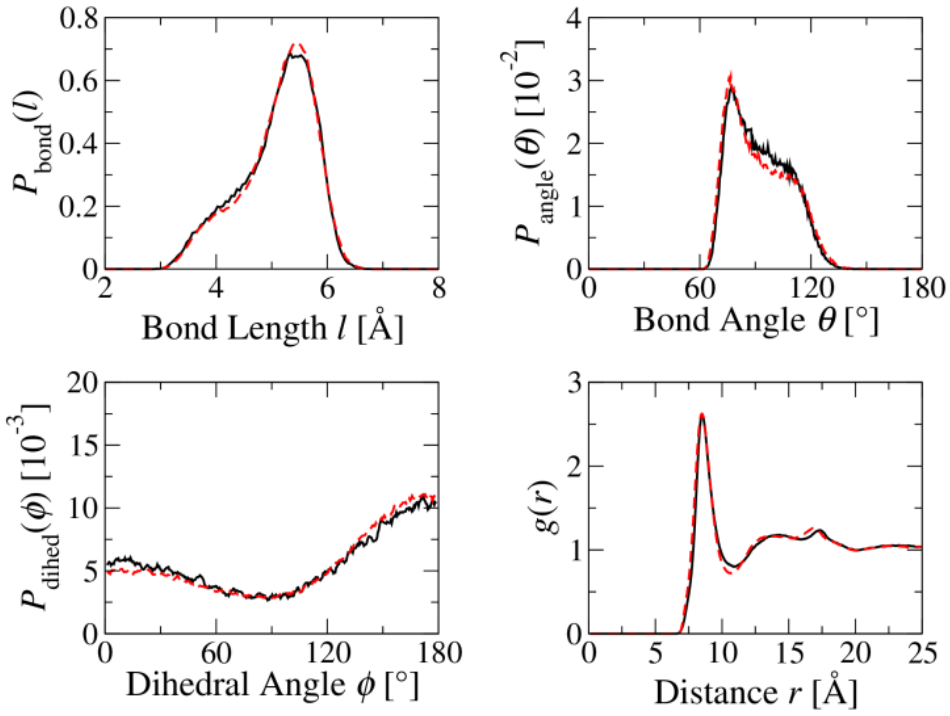

Figure 2.2 Examples of the goodness-of-fit between the structural distributions from the CG simulations (red, dashed) and those from the atomistic MD simulations (black, solid). The system of interest is a PBDT[2F]T:PCBM blend.

2.4 Putting It All Together

In this Chapter, we have described the three computational methodologies that are used in this Thesis for molecular simulations at varying length scales, ranging from the individual molecule to the nanoscale domain. The three methodologies are integrated in a way that preserves the chemical identity of the material of interest such that the structural and electronic properties of the thin-film morphology can be traced back to the molecular structure of its constituents. The procedure we have used is diagrammed in Figure 2.3, where the molecular information from the DFT calculation is passed to the force field for the MD simulation. In turn, the structural distributions from the MD simulation are used to parameterize the force field for the CG

simulation. The results of the MD and CG simulations could also be passed up one level to regain the higher atomistic resolution picture of the system, although this is beyond the scope of this Thesis.

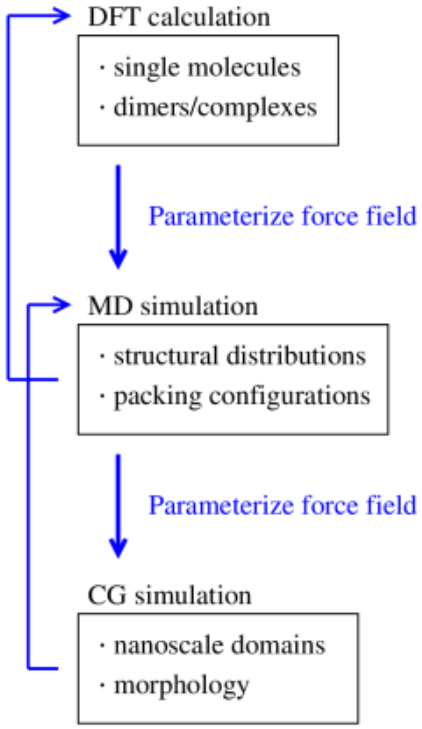

Figure 2.3 Diagram showing the relationships between the three computational methodologies used in this Thesis.

In closing, we have presented in this chapter the theoretical framework for the computational methodologies exploited in this Thesis for studying π-conjugated systems and develop some structure-property relationships for each of them. The results of these investigations are the subject of the following Chapters.

2.5 References

(1) Szabo, A.; Ostlund, N. S. *Modern Quantum Chemistry: Introduction to Advanced Electronic Structure Theory*; Dover, 1996.
(2) Hehre, W. J.; Radom, L.; Schleyer, P. v.R.; Pople, J. A. *Ab Initio Molecular Orbital Theory*; Wiley, 1986.
(3) Sousa, S. F.; Fernandes, P. A.; Ramos, M. J. *J*. *Phys*. *Chem*. *A* **2007**, *111* (42), 10439.
(4) Hohenberg, P.; Kohn, W. *Phys*. *Rev*. **1964**, *136* (3B), B864.
(5) Sholl, D.; Steckel, J. A. *Density Functional Theory: A Practical Introduction*; Wiley, 2009.
(6) Kohn, W.; Sham, L. J. *Phys*. *Rev*. **1965**, *140* (4A), A1133.
(7) Becke, A. D. *Phys*. *Rev*. *A* **1988**, *38* (6), 3098.
(8) Lee, C.; Yang, W.; Parr, R. G. *Phys*. *Rev*. *B* **1988**, *37* (2), 785.
(9) Becke, A. D. *J*. *Chem*. *Phys*. **1996**, *104* (3), 1040.
(10) G09 Keywords: DFT Methods http://www.gaussian.com/g_tech/g_ur/k_dft.htm (accessed Mar 21, 2016).
(11) Riley, K. E.; Op't Holt, B. T.; Merz, K. M. *J*. *Chem*. *Theory Comput*. **2007**, *3* (2), 407.
(12) Karpfen, A.; Choi, C. H.; Kertesz, M. *J*. *Phys*. *Chem*. *A* **1997**, *101* (40), 7426.
(13) Sutton, C.; Körzdörfer, T.; Gray, M. T.; Brunsfeld, M.; Parrish, R. M.; Sherrill, C. D.; Sears, J. S.; Brédas, J.-L. *J*. *Chem*. *Phys*. **2014**, *140* (5), 054310.
(14) Körzdörfer, T.; Brédas, J.-L. *Acc*. *Chem*. *Res*. **2014**, *47* (11), 3284.
(15) Chai, J.-D.; Head-Gordon, M. *Phys*. *Chem*. *Chem*. *Phys*. **2008**, *10* (44), 6615.
(16) Kohn, W. *Rev*. *Mod*. *Phys*. **1999**, *71* (5), 1253.
(17) Valeev, E. F.; Coropceanu, V.; da Silva Filho, D. A.; Salman, S.; Brédas, J.-L. *J*. *Am*. *Chem*. *Soc*. **2006**, *128* (30), 9882.
(18) Frisch, M. J.; Trucks, G. W.; Schlegel, H. B.; Scuseria, G. E.; Robb, M. A.; Cheeseman, J. R.; Scalmani, G.; Barone, V.; Mennucci, B.; Petersson, G. A.; Nakatsuji, H.; Caricato, M.; Li, X.; Hratchian, H. P.; Izmaylov, A. F.; Bloino, J.; Zheng, G.; Sonnenberg, J. L.; Hada, M.; Ehara, M.; Toyota, K.; Fukuda, R.; Hasegawa, J.; Ishida, M.; Nakajima, T.; Honda, Y.; Kitao, O.; Nakai, H.; Vreven, T.; Montgomery Jr., J. A.; Peralta, J. E.; Ogliaro, F.; Bearpark, M. J.; Heyd, J.; Brothers, E. N.; Kudin, K. N.; Staroverov, V. N.; Kobayashi, R.; Normand, J.; Raghavachari, K.; Rendell, A. P.; Burant, J. C.; Iyengar, S. S.; Tomasi, J.; Cossi, M.; Rega, N.; Millam, N. J.; Klene, M.; Knox, J. E.; Cross, J. B.; Bakken, V.; Adamo, C.; Jaramillo, J.; Gomperts, R.; Stratmann, R. E.; Yazyev, O.; Austin, A. J.; Cammi, R.; Pomelli, C.; Ochterski, J. W.; Martin, R. L.; Morokuma, K.; Zakrzewski, V. G.; Voth, G. A.; Salvador, P.; Dannenberg, J. J.; Dapprich, S.; Daniels, A. D.; Farkas, Ö.; Foresman, J. B.; Ortiz, J. V.; Cioslowski, J.; Fox, D. J. *Gaussian 09*; Gaussian, Inc.: Wallingford, CT, USA, 2009.
(19) Jorgensen, W. L.; Maxwell, D. S.; Tirado-Rives, J. *J*. *Am*. *Chem*. *Soc*. **1996**, *118* (45), 11225.
(20) Huang, D. M.; Faller, R.; Do, K.; Moulé, A. J. *J*. *Chem*. *Theory Comput*. **2010**, *6* (2), 526.
(21) Singh, U. C.; Kollman, P. A. *J*. *Comput*. *Chem*. **1984**, *5* (2), 129.
(22) Besler, B. H.; Merz, K. M.; Kollman, P. A. *J*. *Comput*. *Chem*. **1990**, *11* (4), 431.
(23) Hoover, W. G. *Phys*. *Rev*. *A* **1985**, *31* (3), 1695.
(24) Hoover, W. G. *Phys*. *Rev*. *A* **1986**, *34* (3), 2499.
(25) Parrinello, M.; Rahman, A. *J*. *Appl*. *Phys*. **1981**, *52* (12), 7182.

(26) Ryckaert, J.-P.; Ciccotti, G.; Berendsen, H. J. C. *J*. *Comput*. *Phys*. **1977**, *23* (3), 327.
(27) Hockney, R. W.; Eastwood, J. W. *Computer Simulation Using Particles*; Institute of Physics Publishing: Bristol, 1988.
(28) Reith, D.; Pütz, M.; Müller-Plathe, F. *J*. *Comput*. *Chem*. **2003**, *24* (13), 1624.
(29) Plimpton, S. *J*. *Comput*. *Phys*. **1995**, *117* (1), 1.
(30) KAUST Supercomputing Laboratory - King Abdullah University of Science and Technology https://ksl.kaust.edu.sa/Pages/Home.aspx (accessed Apr 12, 2016).
(31) Center for Computational Molecular Science and Technology http://www.ccmst.gatech.edu/ (accessed Apr 12, 2016).

Chapter 3

Impact of Fluorine Substitution on π-Conjugated Polymer Main-Chain Conformations, Packing, and Electronic Couplings

3.1 Introduction

Organic semiconductors, which include π-conjugated polymers,[1] small molecules,[2] and oligomers, are of great interest as active materials for thin-film devices such as organic field-effect transistors (OFETs)[3] and photovoltaic (OPV) cells.[4,5] The potential for low-cost,[6] large-area,[7] and high-throughput manufacturing of such organic-based devices is a major ground for the development of rational design strategies[8,9] geared to improve material properties and enhance performance. Of key interest is to develop a better understanding of how one can systematically tailor chemical structure in π-conjugated systems in order to achieve desirable morphological and optoelectronic properties, which are determining factors to material and device performance.

Design strategies for organic electronic materials include: (i) modulating the electronic, redox, and optical properties via chemical substitution of electron-donating and electron-withdrawing groups; and (ii) influencing solubility/miscibility through substitution of pendant alkyl groups. Interestingly, substitution of fluorines (fluorination) on the π-aromatic motifs along the molecular backbone has generally been shown as an effective approach to enhancing OFET and bulk-heterojunction (BHJ) OPV performance. Material building blocks that have benefited, either directly as the recipient of substitution, or indirectly as co-motifs, from fluorination include: thiophenes,[10,11] carbazoles,[12] thienothiophenes,[13,14] benzothiadiazoles,[12,15–17] benzotriazoles,[18] benzodithiophenes,[10,13,14] indacenodithiophenes,[19] and anthradithiophenes.[20] Fluorination has been implemented in various ways, including: (i) single and double substitution on an aromatic ring;[12,15] (ii) substitution on either the donor or the acceptor motif (or both) along copolymer backbones;[21,22] and (iii) incrementally increasing the fluorine content along the main-chain.[23,24]

Fluorination can lead to important changes in backbone conformation and morphology. For polymers, fluorination has been described as inducing higher degrees of main-chain planarity, rigidity, order, and packing tightness.[23,25,26] For small molecules, fluorination can range from modifying slightly the crystal structure[27] to changing entirely the crystal structure packing motif.[28] In thin-film BHJ solar cells, fluorination of the polymer or small molecule donor material tends to increase the phase separation pattern between the blend component materials and can also affect the purity of the domains formed (via pronounced demixing effects between the donor and acceptor components).[14,15,19] In terms of electronic structure, well-established effects of fluorination are: (i) an increase in ionization potential (IP), which generally yields higher open-circuit voltages (V_{OC}) in BHJ solar cells with fullerene acceptors;[14] and (ii) a concurrent increase in electron affinity (EA) that reduces the energy offset relative to the EA of the fullerene acceptor. In OFETs, fluorination has been described as conducive to enhanced hole mobilities and/or electron mobilities (partly by lowering the energetic barrier for electron injection owing to a larger EA).[29] Overall, the corresponding increased IP and EA, and closer molecular packing, can also result in higher thermal[30] and ambient[29] stability, which are of practical importance for thin-film OPV and OFET device applications.

Despite the well-documented modifications in electronic and structural properties resulting from fluorination outlined above, the underlying molecular-scale effects induced by the presence of fluorine substituents and their impact on thin-film packing remain unclear. The need to forge a better understanding of those effects also lies in the fact that fluorination sometimes leads to poorer material and/or device performance or yields only marginal improvements.[13,19,21] In parallel, it is especially important to examine how fluorination and related molecular-scale effects can induce critical morphological changes in the solid state.

To this end, we focus here on two recently reported donor-acceptor copolymers[10] (Figure 3.1): poly(4,8-bis((2-ethylhexyl)oxy)benzo[1,2-b:4,5-b′]dithiophene-thiophene (PBDT[2H]T) and its 3,4-difluoro-thiophene analog (PBDT[2F]T). In that work,[10] the fluorine-substituted polymer was shown to give rise to a marked two-fold enhancement in the average power conversion efficiency (PCE) (6.8%) as compared to its unsubstituted analog (2.8%) in BHJ solar cells with $PC_{71}BM$ as the acceptor. The PCE enhancement for PBDT[2F]T was shown to be the result of all-around improvements in V_{OC}, short-circuit current density (J_{SC}), and fill factor (*FF*). The higher V_{OC} (0.90 V versus 0.80 V) was attributed to the larger IP of PBDT[2F]T compared to PBDT[2H]T. Likewise, the J_{SC} was found to be starkly higher in PBDT[2F]T (10.7 mA cm^{-2} vs. 6.3 mA cm^{-2}). Overall, the simplicity of the molecular structure of the PBDT[2X]T polymers, their comparable molecular weights,[10] and the notable differences in their performance patterns make them ideal test beds for a comparative examination of the influence of fluorination on electronic and molecular-scale effects in π-conjugated polymers for thin-film device applications.

In this work, we use PBDT[2X]T polymers (X = H or F) as model systems to examine the effects of fluorine substituents on main-chain conformations and packing via combined quantum-mechanical calculations, molecular dynamics (MD) simulations, and solid-state nuclear magnetic resonance (SS-NMR) analyses. Density functional theory (DFT) calculations at the long-range corrected level are performed to parameterize our simulation models and to relate molecular packing configurations obtained from MD simulations to electronic properties relevant to material efficiency patterns. In particular, we elucidate the *intra*- and *inter*-molecular interactions that contribute to the local packing of polymer main-chains in thin films, and correlate those interactions with the specific electronic and charge transport characteristics of

fluorine- and nonfluorine-substituted polymers. The combined theoretical and experimental analyses in this work reveal molecular-scale effects that fluorination induces on main-chain conformations, packing and electronic couplings, which have not been described in prior studies.

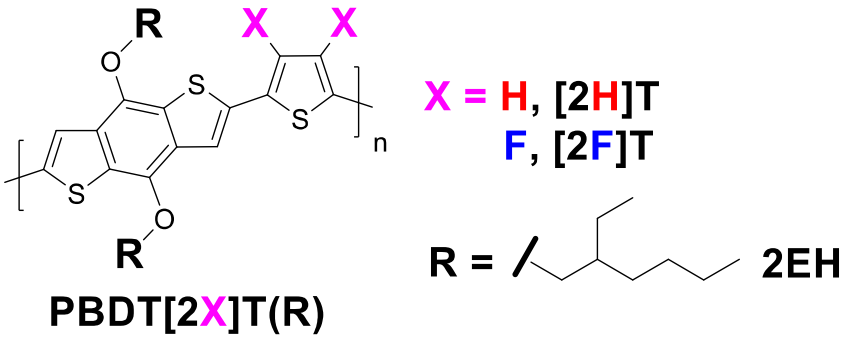

Figure 3.1 Structures of the wide optical-gap PBDT[2X]T polymers (with X = H or F).

3.2 Methodologies

I. Computational Analyses – MD simulations and DFT calculations

In modeling polymers, it is imperative to accurately capture the chain conformational space and electrostatic potential around the polymer chain. For π-conjugated polymers, we expect inter-monomer or inter-ring torsion potentials to be most significant in impacting chain conformation. We therefore updated the generalized OPLS[31] (Optimized Potentials for Liquid Simulations) parameters for atomic charges, bonds, angles, and dihedrals, using long-range corrected DFT-ωB97XD[32]/6-31G(d,p) calculations with the default value (0.2) of the range-separation parameter ω, to reflect the specific chemical nature of the PBDT[2X]T polymers. The atomic

charges were obtained using the ESP (electrostatic potential) method, which fits to the quantum chemical (QC) molecular electrostatic potential. We proceeded to modify these QC-derived charges slightly to ensure charge neutrality in each chain as detailed in Appendix A. Torsion profiles were obtained for increasing chain lengths until convergence was reached, which was a tetramer for both polymers as shown in Figure A1. Using the converged QC torsion profile, we obtained dihedral parameters for MD simulations by iteratively performing a constant volume and temperature (NVT ensemble) simulation of a trimer chain in vacuum at finite temperatures until the optimized parameters gave the same "intrinsic" torsion profile as that obtained from QC calculations, as shown in Figure A2. The MD "intrinsic" torsion profile is approximated as a free energy following the equation $U_{\text{dihed}}(\varphi) = -kT\ln[P_{\text{dihed}}(\varphi)]$, where $P_{\text{dihed}}(\varphi)$ is the dihedral-angle distribution. The procedure used here to obtain dihedral parameters ensures that the MD torsion profile matches well the QC profile within the temperature range of interest, which is demonstrated in Figure A2.

The choice of chain length and number of chains for simulations was determined with consideration to computational feasibility. Given the relatively large number of atoms per monomer of PBDT[2X]T, we chose to simulate systems of ~30,000 atoms consisting of 80 chains with a chain length of 5 monomers. While, practically, material systems with longer chains are involved in the making of thin-film polymer devices, we direct our analyses to the local structure in these materials and the chain length considered here has been demonstrated to suffice to discern differences in molecular packing.[33] Ideally, simulations of oligomer chains in the melt should be sufficiently long to allow for chain relaxation via reorientation as characterized by $\tau_{2,}$ which is obtained by fitting the auto-correlation function of a unit vector u(t) between the chain ends to the equation $\langle P_2[\mathrm{u}(t)\cdot\mathrm{u}(0)]\rangle \approx \exp(-t/\tau_2)$, where $P_2 \equiv (3x^2 - 1)/2$ is the

second-order Legendre polynomial. However, the chain relaxation time is too large for these PBDT[2X]T 5-mer chains (about 166 and 222 ns for [2H]T and [2F]T, respectively, at 550 K) to feasibly simulate for several lengths of τ_2. Therefore, simulations were performed for duration of one τ_2 whereby distribution functions and quantities of interests were computed from trajectories corresponding to the latter half of τ_2 and were checked that they did not vary systematically with time.

To examine the molecular packing at room temperature, the PBDT[2X]T systems were cooled from 550 K to 298 K over the course of 10 ns. Dimers of chains were extracted from the bulk system if any atom on one chain backbone is within 4 Å from another atom on the adjacent chain backbone. This dimer selection method is rationalized by the expectation that the frontier orbitals relevant to charge transport properties are located predominantly on the chain backbone. Binding energies were calculated for the extracted dimers at the ωB97XD/6-31G(d,p) level with counterpoise correction to account for basis set superposition errors (BSSE). The calculations of the electronic couplings (transfer integrals) were performed at the same level of theory using the accurate method of Valeev et. al.[34]

II. Experimental Analyses – Solid-State NMR

For SS-NMR investigations, the PBDT[2X]T polymers were first dissolved in chlorobenzene at a concentration of 20 mg ml^{-1}. The solutions were left to stir overnight at 110 °C and subsequently drop-cast on clean silicon wafers. The films were left to dry under vacuum for 5 hours. Using a clean blade, the films were scrapped off the wafers, and the collected samples were placed under high vacuum for 3 days. The samples were then loaded into 2.5 mm o.d. Bruker rotors.

SS-NMR experiments were conducted on a Bruker Avance III spectrometer operating at 14.1 T using a Bruker 2.5 mm HFX triple resonance probe. The ^{1}H and ^{13}C signals were calibrated to adamantane as a secondary external reference (1.85 ppm (relative to neat TMS)[35] and 37.77 ppm (on the IUPAC scale),[36] respectively).

1D $^{13}C\{^{1}H\}$ recoupled polarization transfer-heteronuclear single quantum coherence (REPT-HSQC)[37] experiments were conducted at a spinning frequency of 29,762 Hz, using a 3.50 μs 90° pulse on both ^{1}H and ^{13}C channels. The relaxation delay was set to 2 s and one rotor period (t_r) of recoupling was utilized to primarily observe ^{13}C nuclei with directly bonded protons. Proton decoupling via SPINAL64[38] was employed during acquisition at a radio-field strength of 81 kHz. For the PBDT[2F]T polymer, ^{19}F decoupling via the rotor-synchronized π pulse scheme[39] was also concurrently employed at a radio-field strength of 50 kHz. Over 112,000 scans were collected in total. Line fitting on the resulting spectra was performed using Mnova NMR software by Mestrelab Research.

2D $^{13}C\{^{1}H\}$ recoupled polarization transfer-heteronuclear dipolar order rotor encoding (REPT-HDOR)[37] experiments were conducted at a spinning frequency of 25,000 Hz, using a 3.50 μs 90° pulse on both ^{1}H and ^{13}C channels. The relaxation delay was set to 2 s and a 3 t_r recoupling time was employed. 20 t_1 increments were recorded at a dwell time of 2 μs for a total evolution time of 20 μs (1 t_r), using over 2,000 scans per increment. Only the cosine dataset was acquired for all experiments. Relevant slices from the 2D spectrum were replicated 120 times before Fourier transformation to obtain the ^{13}C-^{1}H dipole-dipole side band patterns. Simulations to fit the measured spectra were performed using a MATLAB program developed by the solid-state NMR group in Mainz, Germany.[37]

2D multi-quantum ^{1}H-^{1}H NMR experiments were conducted at a spinning frequency of 29,762 Hz, using a ^{1}H 90° pulse of 2.4 μs. A relaxation delay of 1.68 s (50 t_r), 96 t_1 increments with a dwell time of one t_r, and 16 scans per fid were acquired for all experiments. The States-TPPI scheme was used to acquire spectra for all experiments. For 2D ^{1}H-^{1}H double quantum-single quantum (DQ-SQ) experiments, the compensated Back-to-Back (BaBa) dipolar recoupling sequence[40] was used with one t_r of DQ excitation and reconversion, and a one t_r long z-filter. For 2D ^{1}H-^{1}H triple quantum-single quantum (TQ-SQ) experiments, a BaBa dipolar recoupling sequence[41] was used with two t_r of TQ excitation and reconversion, and a z-filter set to one t_r. ^{1}H syn (S)/anti (A) assignments in the resulting spectra were determined via a 2D frequency switched Lee-Goldburg heteronuclear correlation (2D ^{13}C{^{1}H} FSLG HETCOR) experiment[42] using a short (50 μs) Lee-Goldburg cross polarization[43] pulse to polarize only directly bonded ^{13}C-^{1}H spin pairs. The homonuclear decoupling used in this experiment produced a 2D ^{13}C-^{1}H correlation spectrum at a much higher resolution than the 2D ^{13}C{^{1}H} REPT-HSQC.[44] The thiophene 2D ^{13}C-^{1}H region is shown in Figure A4.

3.3 Results and Discussion

We begin our discussion by examining the charge-carrier mobilities in neat films of PBDT[2X]T polymers and how these measured values suggest important differences in chain packing between the polymers. We then lay the foundation of our work by describing the intrinsic main-chain torsion profiles of these polymers. We proceed to use, in parallel, MD simulations and SS-NMR analyses to describe the structural behavior of these polymers in terms of their *intra*- and *inter*-molecular interactions, and their respective stacking patterns in thin films. Finally, we

discuss how differences in main-chain conformation and chain packing lead to differences in binding energy and electronic coupling between neighboring chains in thin films.

Hole mobilities

The hole mobilities of the PBDT[2X]T polymers in neat films were determined using the space-charge-limited current (SCLC) model using hole-only device configurations for the measurements (see details in Appendix A). SCLC mobility measurements capture the vertical mobility of charge carriers moving between bottom and top electrodes in a vertically stacked device analogous to the configuration used for the fabrication of thin-film BHJ solar cells. The SCLC mobility measurements showed that the PBDT[2F]T neat films exhibited a zero-field hole mobility that is ca. 7 times larger than that of PBDT[2H]T (5.2×10^{-6} cm^2 V^{-1} s^{-1} vs. 7.2×10^{-7} cm^2 V^{-1} s^{-1}) (See Figure 3.2, and Tables A2 and A3). All other things being equal, the net difference in carrier mobility between the two polymers in neat films could stem from inherent conformational, local packing and/or morphological effects related to the presence or absence of fluorine substituents along the polymer main-chain. In the following sections, we examine those effects in detail, starting with a comprehensive analysis of the intrinsic torsion behavior of single chains of PBDT[2H]T and PBDT[2F]T.

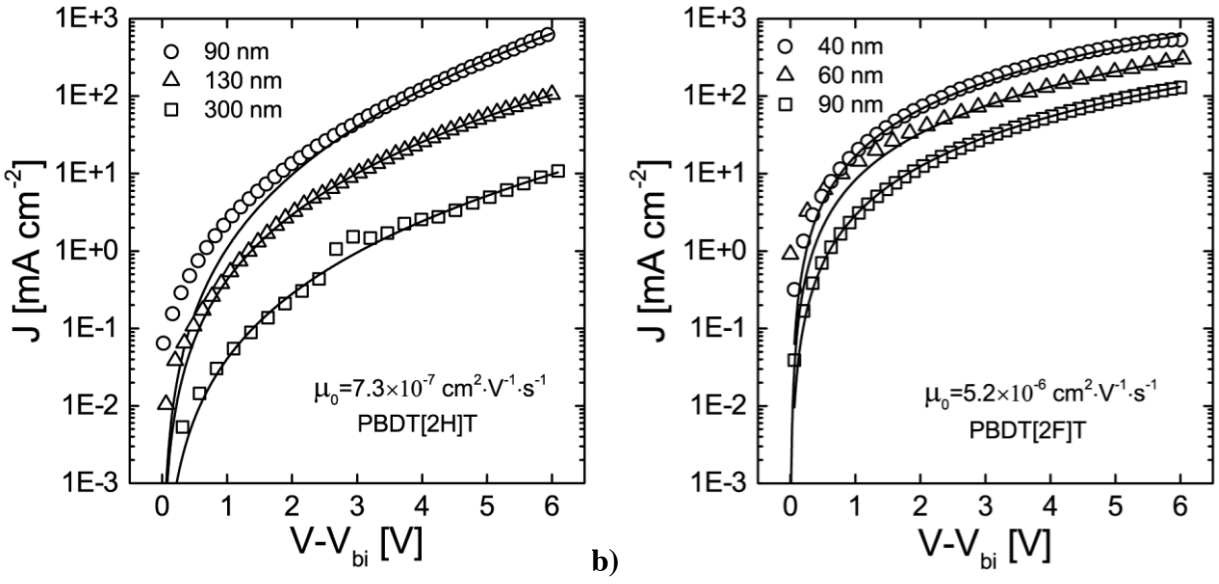

Figure 3.2 Experimental dark current densities as a function of effective electric field for hole-only devices made with neat films of a) PBDT[2H]T and b) PBDT[2F]T. Diode configuration: ITO/PEDOT:PSS/PBDT[2X]T/MoO_3/Ag. The legend indicates the different film thicknesses used for this analysis. The experimental data were fitted using the single-carrier SCLC model as described in Appendix A.

Main-chain torsion profiles

Theoretical investigations comparing unsubstituted versus fluorine-substituted π-conjugated systems, polymers in particular, have largely relied on DFT calculations with the B3LYP functional to study energy-minimized structures and/or to characterize the inter-monomer or inter-ring torsion profiles.[10–12,21,25] However, B3LYP has been shown to significantly overestimate torsion barriers for several π-conjugated systems,[45,46] which is a result of the functional's intrinsic error in over-delocalizing the electron density and, as a result, over-stabilizing planar conformations. In general, the problem of excess electron delocalization and localization is common to standard (semilocal and global hybrids) DFT functionals and Hartree-Fock methods, respectively;[46] in standard DFT, the delocalization error stems from the

Coulombic self-repulsion of one-electron densities (electron self-interaction error), while in the Hartree-Fock method, the localization error stems from the absence of static electron correlation. In this work, we therefore employ ωB97XD,[32] a long-range corrected functional that minimizes the (de)localization error by matching the energy of the highest occupied molecular orbital (HOMO) of a molecular system to its ionization potential (IP), which is a property obeyed by the exact functional.[47] The ω-value obtained in this matching procedure is referred to as the "IP-tuned" ω-value. Our rationale for using the ωB97XD functional is three-fold: (i) to obtain a reliable description of the inter-monomer torsion profile; (ii) to obtain a robust description of the electronic structure with a balanced account of (de)localization effects; and (iii) to obtain an appropriate description of weak non-covalent interactions by explicit inclusion of empirical dispersion. The first point is important for our molecular simulations, while the latter two are important for determination of the electronic couplings and binding energy between neighboring chains in the bulk.

We first examine the intrinsic inter-monomer torsion profile, which is expected to control the main-chain dihedral distribution in the bulk, and in turn to determine how neighboring chains pack. Intermolecular interactions do obviously also play an important role in chain packing and will be examined next.

The converged DFT-ωB97XD/6-31G(d,p) torsion profiles for single chains of PBDT[2H]T and PBDT[2F]T in vacuum are shown in Figure 3.3. For PBDT[2H]T, the syn conformer is energetically higher than the anti conformer by about ~1 kcal mol^{-1}. There are two shallow local minima at ~30° and ~160°, which would favor markedly non-planar conformers. These local minima are separated by energetic barriers of ~2 kcal mol^{-1} (on going from syn to anti conformer) and ~3 kcal mol^{-1} (on going from anti to syn conformer). Therefore, conformers

corresponding to the local minimum on the anti side are expected to dominate the main-chain dihedral distribution in the bulk. In contrast, for PBDT[2F]T, the local minima are located at the syn and anti conformer (~0° and ~180°, respectively), and there is no energetic offset between them. Thus, planarity is more favored in PBDT[2F]T relative to PBDT[2H]T. The energetic barriers are the same in transitioning between syn and anti conformers in PBDT[2F]T, suggesting a more balanced distribution of syn and anti conformers in the bulk. If we bear in mind that *RT* at room temperature (298 K) is approximately 0.6 kcal mol^{-1}, the energetic barriers of 2-3 kcal mol^{-1} here is a significant impediment to inter-conversion between anti and syn conformers at room temperature.

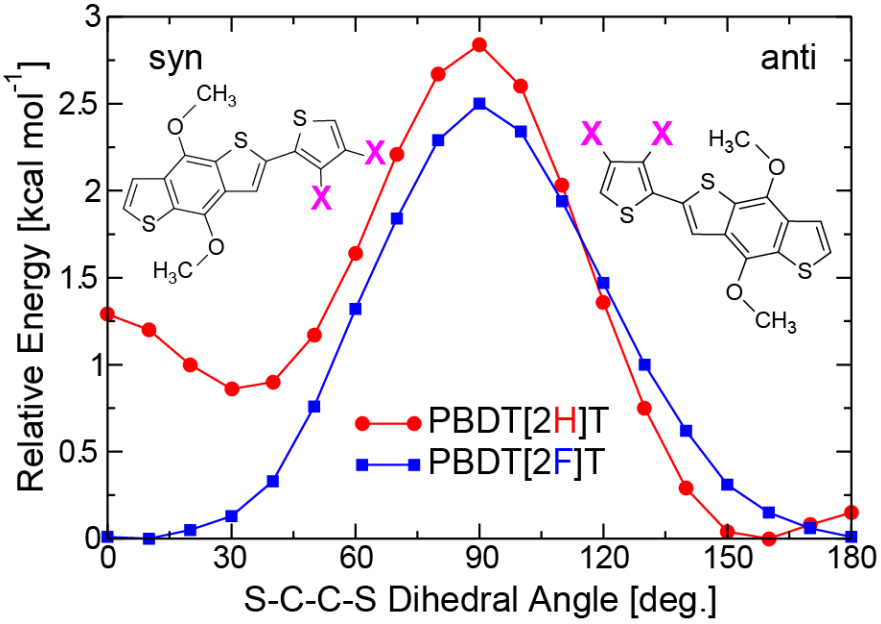

Figure 3.3 Converged inter-monomer torsion profile for PBDT[2H]T and PBDT[2F]T (both tetramers) determined using DFT calculations at the ωB97XD/6-31G(d,p) level.

SS-NMR was employed to experimentally characterize the conformational landscape of the PBDT[2X]T polymers in thin films. ^{13}C NMR is an appropriate method to explore conformations in the solid state due to the high sensitivity of the ^{13}C isotropic chemical shift to the spatial configuration of neighboring nuclei.[48] To probe this property in self-assembled films of PBDT[2X]T polymers, we performed 1D $^{13}C\{^{1}H\}$ REPT-HSQC NMR experiments. By employing one rotor period of dipolar recoupling, only strong signals from directly bonded ^{13}C-^{1}H spin pairs are measured, effectively precluding any overlapping signals from non-protonated moieties within the polymers. Figure 3.4a shows the full 1D $^{13}C\{^{1}H\}$ REPT-HSQC spectrum for both polymers. As expected, the ^{13}C chemical shifts of the alkyl chains (10-40 ppm) are similar between PBDT[2H]T and PBDT[2F]T. However, a key difference in ^{13}C chemical shift between the two polymers is seen for the fused thiophenes of the BDT unit (labeled 2 in Figure 3.4). As apparent in Figure 3.4b, much of the signal from the fused thiophenes in PBDT[2F]T is centered at ~117 ppm while the majority in PBDT[2H]T is centered around ~114 ppm. A prominent shoulder around ~114 ppm is observed in the PBDT[2F]T spectrum, while a much attenuated one is seen at ~116 ppm in the PBDT[2H]T spectrum. Note that there is no signal at ~122-124 ppm for PBDT[2F]T due to the absence of C-H bonds at the positions labeled 7. Since the anti conformers in both polymers would have the BDT carbon 2 located near the sulfur groups of PBDT[2X]T, the isotropic chemical shift at ~114 ppm is assigned to the anti conformer. Conversely, since the syn conformer would result in the BDT carbon 2 being close to either a hydrogenated or a fluorinated carbon 7 of PBDT[2X]T, the isotropic chemical shifts at ~116 and ~117 ppm are attributed to the syn conformation of PBDT[2H]T and PBDT[2F]T, respectively. This conformational assignment is qualitatively consistent with theoretical chemical shifts

determined from DFT calculations using the gauge-including atomic orbital (GIAO)[49] method (see details in Appendix A).

Furthermore, given the similar effective heteronuclear dipolar couplings experienced at the carbon position 2 in both polymers (see Figure A4), the ^{13}C intensities of thiophenes in the 1D $^{13}C\{^{1}H\}$ REPT-HSQC spectra should correspond approximately to the relative distribution of syn and anti conformers in the film. To quantify this syn/anti ratio, the correspondent thiophene portion of the 1D $^{13}C\{^{1}H\}$ REPT-HSQC spectrum was fitted to Gaussian functions for both polymers. For PBDT[2F]T (Figure 3.5a), the ^{13}C chemical shift labeled 2 corresponding to the fused thiophene was fitted to two Gaussian functions centered at 113.7 ppm and 116.9 ppm, corresponding to the anti and syn conformers, respectively. Likewise, the analogous ^{13}C chemical shift in PBDT[2H]T (Figure 3.5b) was fitted to two Gaussian functions at 113.8 ppm and 115.6 pm, corresponding also to the anti and syn conformers, respectively. Table 3.1 summarizes the relative distributions of syn and anti conformers obtained from the fitting protocol described above (and compares them to the MD results discussed below).

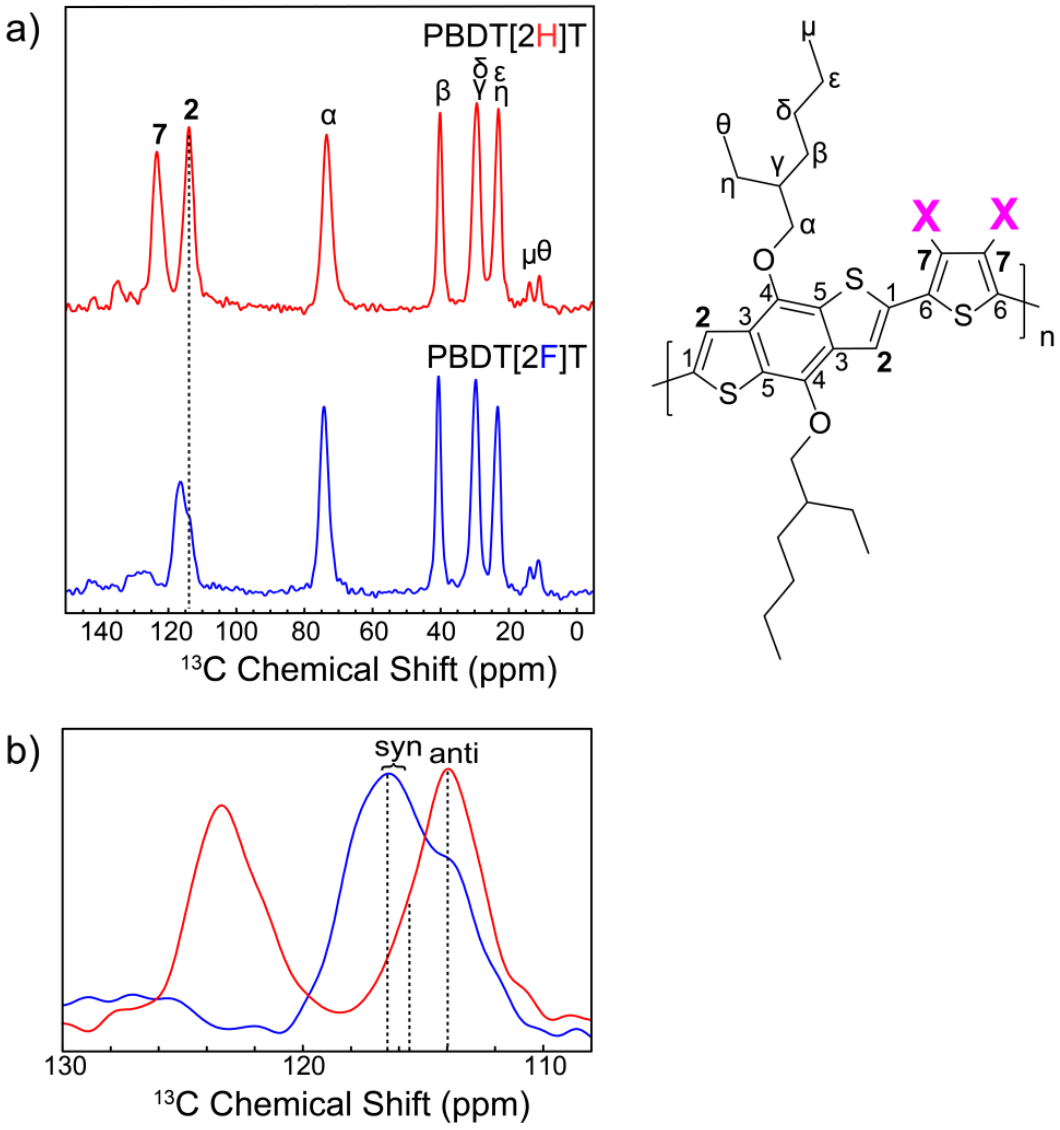

Figure 3.4 (a) 1D $^{13}C\{^{1}H\}$ REPT-HSQC NMR spectra of PBDT[2H]T (red) and PBDT[2F]T (blue) assigned according to the labeled chemical structure shown on top. Note that since only one rotor period of recoupling was used in the experiment, only ^{13}C nuclei directly bonded to hydrogen appear in the spectra. (b) Expansion of the thiophene region of spectra presented in (a), with assignment of the ^{13}C isotropic chemical shifts to the syn and anti conformers.

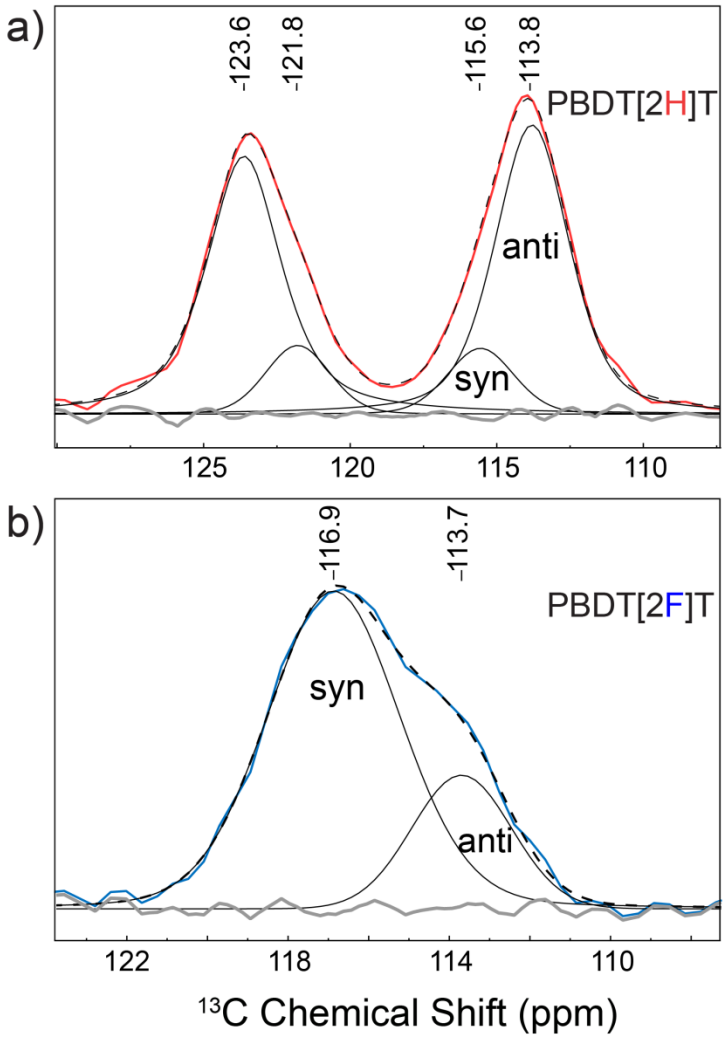

Figure 3.5 Gaussian fits to 1D $^{13}C\{^{1}H\}$ REPT-HSQC NMR spectra for (a) PBDT[2H]T and (b) PBDT[2F]T. The red and blue lines outline the experimental spectra of PBDT[2H]T and PBDT[2F]T, respectively. The black solid lines represent Gaussian fits to the experimental line shapes. The black dashed lines represent the sum of the Gaussian-fitted lines. The grey lines represent the residuals of the fit to the experimental data.

Table 3.1 Relative populations (in %) of syn and anti conformers of the PBDT[2X]T polymers in the bulk as derived from SS-NMR analyses and MD simulations.

Polymer	Syn	Anti
PBDT[2H]T (NMR)[a]	16	84
PBDT[2H]T (MD)[b]	18	82
PBDT[2F]T (NMR)[a]	77	23
PBDT[2F]T (MD)[b]	64	36

[a]Determined by deconvoluting the peaks corresponding to BDT thiophenes in the $^{13}C\{^{1}H\}$ REPT-HSQC spectrum acquired with one recoupling rotor period.

[b]Determined by computing the inter-monomer dihedral distribution from a constant NPT simulation of 80 5-mer chains at 550 K and using the Boltzmann equation to approximate the relative ratio of syn/anti conformer at 298 K.

The syn/anti ratio for PBDT[2H]T follows the trend depicted by the intrinsic inter-monomer torsion profile discussed earlier (Figure 3.3), favoring the anti conformer (or more precisely, the conformers closely resembling the anti conformer). In contrast, the intrinsic inter-monomer torsion profile of PBDT[2F]T depicted an even syn/anti ratio; however, the syn/anti ratio is shifted towards the syn conformer. In thin films, some specific intermolecular interactions governing chain packing are likely to be at the origin of the prominence of the syn conformers. The shift in syn/anti ratio for PBDT[2F]T will be discussed further in later sections of this study, when we examine the binding energy between neighboring chains.

The inference of the relative ratio of syn/anti conformers in the solid state from SS-NMR spectra can be substantiated by comparison with MD simulations (whereby all atomic positions take known coordinates). While the single-chain torsion profiles described earlier could depict the main-chain conformation distribution in the bulk at finite temperature by simply invoking the Boltzmann equation, this would neglect consideration of important intermolecular interactions that also need to be taken into account. Thus, atomistic MD simulations can provide a more complete description of main-chain conformation and packing in the bulk[33] and provide molecular-scale insight into structure-property relationships.

Constant temperature and pressure (NPT ensemble) simulations of 80 5-mer chains of PBDT[2X]T were performed at 550 K, which corresponds to the melt. Simulations at this elevated temperature allow for exploration of the entire phase space for the structural properties of interest in this study. Figure 3.6 shows the dihedral distributions for the inter-monomer bonds of the PBDT[2X]T polymers. The dihedral distributions for PBDT[2H]T are in line with the intrinsic (single-chain) torsion potential, wherein the local-minimum anti conformers prevail over the syn conformers. The local maxima in the distributions align with the minima of the torsion potential; there are substantial numbers of out-of-plane conformers, which would hinder close main-chain stacking and is expected to be detrimental for *inter*-molecular charge-carrier transport. The dihedral distributions for PBDT[2F]T are also consistent with its intrinsic torsion potential, where the maxima of the distributions align with the minima of the torsion potential at the planar anti and syn conformational extremes. In general, the distribution for PBDT[2F]T is much more steep in the regions near the anti and syn conformational extremes, which indicates that, in the bulk, breaking away from planarity is more energetically demanding than in PBDT[2H]T. Planar chains are expected to facilitate more efficient *intra*-chain charge transport

due to a more extended π-conjugation length and larger electronic coupling between adjacent monomers along the chains. In parallel, the higher propensity for planarity in PBDT[2F]T is expected to favor main-chain stacking, which may further promote charge transport (*inter*-chain) in PBDT[2F]T. Here, the dihedral distributions seen for the PBDT[2X]T polymers are revealing of the degree of chain stacking in the bulk as will be shown below.

Using the main-chain conformational distributions discussed above for the PBDT[2X]T polymers, we can relate the relative ratio of syn/anti conformers from simulations at 550 K to that at 298 K using the Boltzmann equation. The assumption used here is that the intrinsic torsion potential is equivalent at the two temperatures, which is reasonable given the good fit in the range of 300-500 K (see Figure A3). The deduced ratios are shown in Table 3.1 and match well those deduced from fitting the SS-NMR spectra, favoring the anti conformer for PBDT[2H]T and the syn conformer for PBDT[2F]T. The very good agreement between values derived from SS-NMR spectra and MD simulations gives validation to the methodologies we have followed in this work (the agreement between experiment and simulation can be expected to even further improve when considering longer chains in the simulations, as longer chains should enhance the propensity for planarity or non-planarity due to correlations along the main-chains).

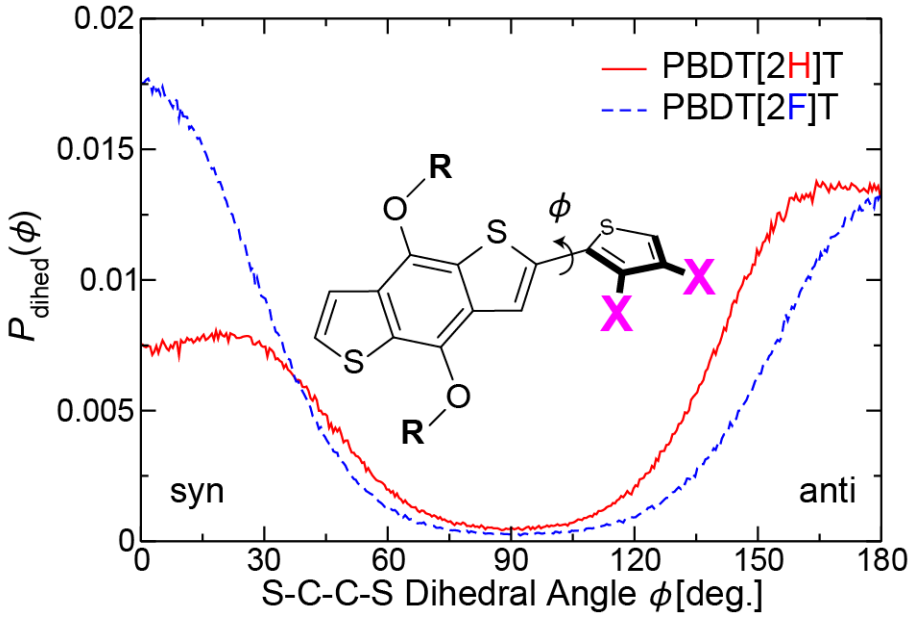

Figure 3.6 The inter-monomer dihedral distributions determined from constant NPT simulations of 80 5-mer chains of PBDT[2X]T at 550 K.

Main-chain packing

To further the idea that the inter-monomer dihedral distributions are revealing of the degree of chain stacking in the bulk, we determined the orientational correlation function (OCF) for a pair of normal unit vectors, n_i and n_j, located at the centers-of-mass of backbone rings on different chains as shown in Figure 3.7 (inset). Vector 1 is located on the lone thiophene and vector 2 on the central benzene ring in BDT. The OCF, or $P_2[\mathbf{n}_j(r)\cdot\mathbf{n}_i(0)]$ where P_2 is the second-order Legendre polynomial, is a measure of the spatial correlation of chain planarity, and hence the degree of order in main-chain packing. The limits of P_2 are 1, -½, and 0, which correspond to parallel (or anti-parallel), perpendicular, and uncorrelated vectors, respectively. Figure 3.7 shows clearly that the order in chain packing is higher in PBDT[2F]T than in PBDT[2H]T at the level of this analysis. At small neighboring distances, chain backbones of aromatic rings can only pack

by stacking in parallel, hence the first-order peak in the OCF reaches 1. The correlation decays as a function of distance, with PBDT[2F]T clearly sustaining higher correlation as compared to PBDT[2H]T. The higher order in chain packing for PBDT[2F]T can be attributed as the result of the higher propensity for planarity discussed above. Again, we recall that planar chains would facilitate more efficient *intra*-chain charge transport while more ordered chain packing is expected to facilitate *inter*-chain charge transport.

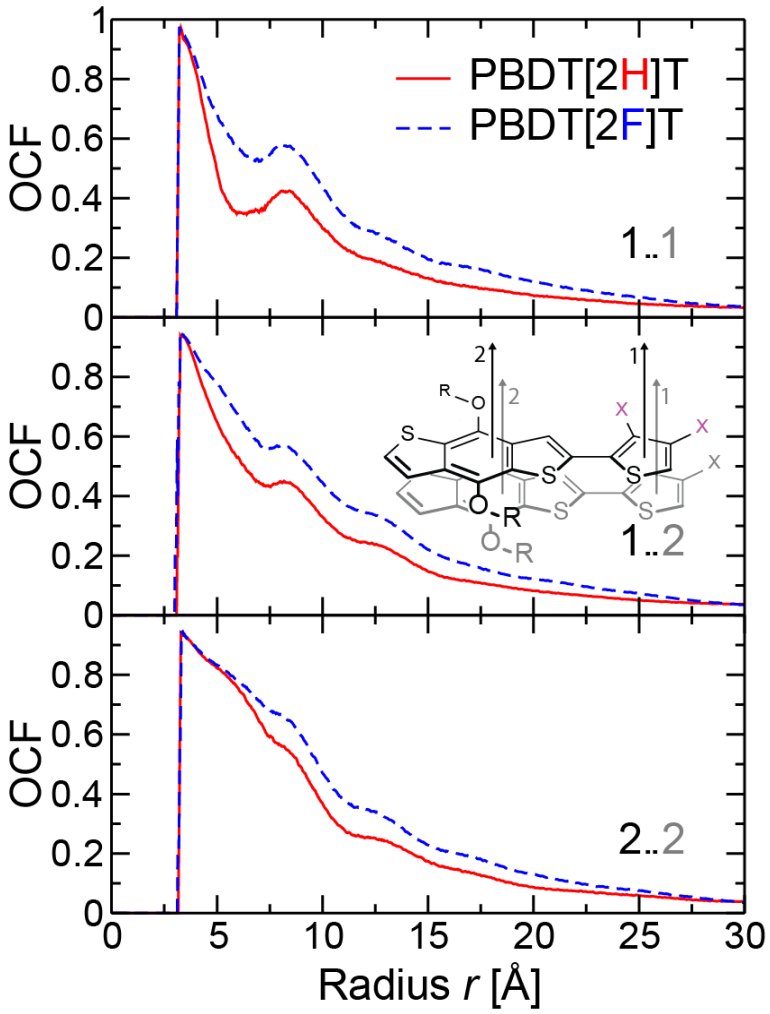

Figure 3.7 The orientational correlation functions (OCFs, $P_2[\mathbf{n}_j(r)\cdot\mathbf{n}_i(0)]$), for pairs of unit vectors normal to the chain backbone rings, determined from constant NPT simulations of 80 5-mer chains of PBDT[2X]T at 550 K. Inset: The paired vectors are located on different chains; vector types 1 and 2 correspond to the lone thiophene in [2X]T and central benzene ring in BDT, respectively.

Having established that PBDT[2F]T is likely to exhibit higher degree of chain planarity and chain packing order than PBDT[2H]T, we now inspect the chain packing patterns in the two polymers. We examine how chains pack in thin films, at the scale of individual motifs along the polymer main-chains, by using double quantum-single quantum (DQ-SQ) and triple quantum-single quantum (TQ-SQ) NMR experiments. These experiments can be exploited to characterize the interaction network of distinct protons across both aliphatic and olefinic chains. In the case of *intra*-molecularly isolated protons, these experiments can reveal specific *inter*-molecular interactions between protons that reside within ~4 Å[50,51] (an inter-nuclear distance on par with that of π-π stacking in conjugated systems). The ^{1}H-^{1}H DQ-SQ NMR spectra of the PBDT[2X]T polymers are shown in Figure 3.8 (a, b), with proton types indicated by colored circles. For PBDT[2H]T (Figure 3.8a), well-resolved ^{1}H-^{1}H correlations indicate the various expected *intra*-molecular interactions between the protons of the alkoxyl chain (green and purple), BDT thiophene (yellow), and the thiophene (black). In parallel, the high intensity correlation on the diagonal at around ~6 ppm (SQ axis) indicates *inter*-molecular interactions between adjacent BDT thiophenes (yellow-yellow) and possibly those between adjacent lone thiophenes (black-black). These specific on-diagonal correlations, typically referred to as autocorrelations, are consistent with a co-facial-like arrangement between backbones in PBDT[2H]T. Turning to PBDT[2F]T, *intra*- and *inter*-molecular interactions are also apparent from the DQ-SQ NMR spectrum (Figure 3.8b). However, in contrast to PBDT[2H]T, the double quantum correlation observed in the region of the BDT thiophenes is significantly less pronounced, suggesting the existence of staggering effects in the packing of PBDT[2F]T polymers. Further examining the *inter*-molecular arrangement in the chain packing pattern of PBDT[2X]T, ^{1}H-^{1}H TQ-SQ NMR was employed to extend the probing range of the interaction network to three protons.[52] In the

context of molecular backbone stacking, it allows for the determination of possible interactions between three backbones within a stack. Akin to ^{1}H-^{1}H DQ-SQ spectra, *inter*-molecular interactions can be described by focusing on the signal of *intra*-molecularly isolated protons along the diagonal of the spectrum. The ^{1}H-^{1}H TQ-SQ NMR spectra for the PBDT[2X]T polymers are shown in Figure 3.8 (c, d). For PBDT[2H]T (Figure 3.8c), co-facial stacking persists between backbones as indicated by the correlations at ~12 and ~16-18 ppm (TQ axis). In contrast, the absence of TQ correlations along the diagonal in the ^{1}H-^{1}H TQ-SQ spectrum of PBDT[2F]T (emphasized by the purple and yellow-circled area in Figure 3.8d), confirms the existence of pronounced staggering effects in thin films of this polymer.

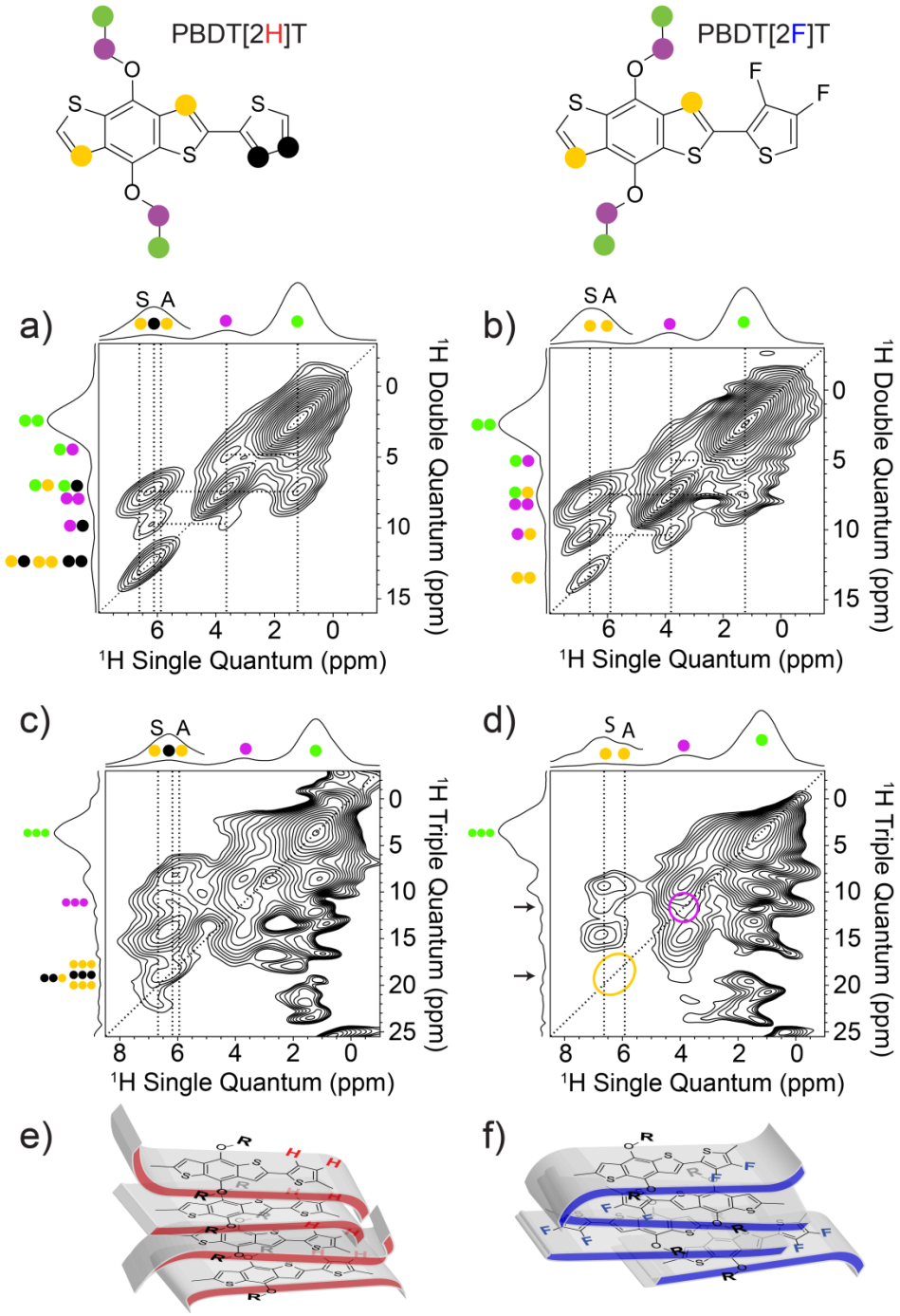

Figure 3.8 ^{1}H-^{1}H double quantum-single quantum (DQ-SQ) (top) and ^{1}H-^{1}H triple quantum-single quantum (TQ-SQ) (bottom) NMR spectra of PBDT[2H]T (a, c) and PBDT[2F]T (b, d). The colored circles indicate proton types as depicted by the chemical structures above the spectra. S and A refer to the BDT thiophene protons in the syn and anti conformers, respectively. For the ^{1}H-^{1}H TQ-SQ spectra, only the diagonal assignments are highlighted. Schematic representations of the stacking patterns of PBDT[2H]T and PBDT[2F]T are shown in (e) and (f), respectively.

Turning to the MD simulations, the presence of staggering effects in the PBDT[2X]T polymers can be examined by comparing the radial distribution functions (RDFs), $g(r)$, for pairs of sites on different chains as shown in Figure 3.9. The RDFs are determined from constant NPT simulations of 80 5-mer chains at 550 K; sites 1 and 2 correspond to the centers-of-mass of the lone thiophene and the central benzene ring in BDT, respectively. The RDF measures the probability of finding a site some distance away from a reference site. The location and height/sharpness of the first-order peak (at small distances) indicate the proximity and interaction strength, respectively, in the packing of the sites involved. Secondary and higher-order peaks reflect higher degrees of order. The RDF profiles show a distribution of co-facial (1..1 and 2..2) and staggered (1..2) chain packing in both PBDT[2X]T systems. The first-order peaks in the 1..1 distributions are broader and located at a slightly larger distance than in other distributions, indicating greater freedom for the lone thiophene to rotate about its inter-ring bonds. In the 1..2 distributions, and looking at the first-order peaks, the staggering effects in the packing of PBDT[2F]T are clearly more pronounced compared to PBDT[2H]T. In parallel, the presence of smaller secondary peaks in the PBDT[2F]T distributions points to an overall higher degree of order. In general, the relative distributions of co-facial and staggered main-chains are expected to affect *inter*-chain charge transport given that the electronic couplings (or transfer integrals) between adjacent backbones are dependent on the degree of overlap and phase-alignment of the molecular orbitals involved.

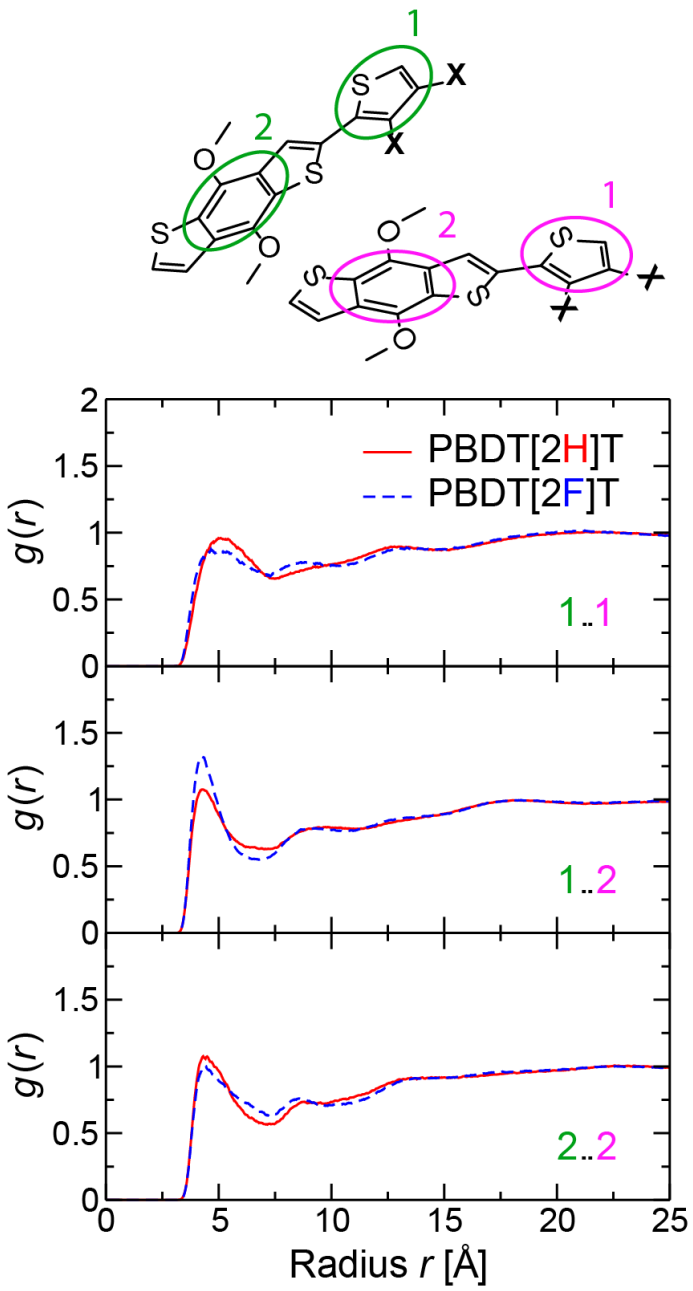

Figure 3.9 Radial distribution functions (RDFs), $g(r)$, determined from constant NPT simulations of 80 5-mer chains of PBDT[2X]T at 550 K. Inset: Sites 1 and 2 correspond to the centers-of-mass of the lone thiophene and central benzene ring in BDT, respectively.

Electronic couplings and binding energies

To explore how the inter-monomer dihedral distribution and chain packing affect electronic coupling, we carried out MD simulations in which we cooled the PBDT[2X]T systems from 550 K to 298 K over the course of 10 ns. This cooling rate is expected to be sufficiently slow to prevent kinetic frustration whereby high energetic conformations at higher temperatures remain stuck while the temperature is being lowered, in which case the conformational distributions at low temperature would be misrepresented; Figure A3 shows the inter-monomer dihedral distributions at 298 K, which is consistent with the higher temperature simulations. From the PBDT[2X]T systems at 298 K, we extracted dimers of neighboring chains that have atoms on their backbone within a distance of 4 Å of each other; this resulted in the gathering of 80 and 94 dimers for PBDT[2H]T and PBDT[2F]T, respectively. The electronic couplings and binding energies of the extracted PBDT[2X]T chain dimers were determined using DFT-ωB97XD/6-31G(d,p) calculations and are shown in Figure 3.10. Note that we chose to emphasize the electronic couplings between HOMO orbitals since the PBDT[2X]T polymers are used as donor materials in thin-film BHJ solar cells with fullerene acceptors.[10] In inspecting the chain dimers, we categorized them on the basis of the number of monomers that are stacking (see Figure 3.11 for snapshots of representative dimers).

The first important observation is that, expectedly, chain dimers with more extended stacking lead to higher binding energies (Figure 3.10). The overall higher binding energies in PBDT[2F]T chain dimers are indicative of higher thermal stability, which is consistent with differential scanning calorimetry measurements of similar fluorinated polymers.[30] There are many more dimers in PBDT[2F]T than in PBDT[2H]T that show extended stacking patterns, which stems from the higher propensity for chain planarity in congruence with the results of the

higher temperature simulations and DFT calculations discussed above. Accompanying the extended chain stacking in PBDT[2F]T is (generally) higher electronic coupling between HOMO orbitals, although some appreciable values are obtained for modest chain stacking as well. The latter case occurs when the molecular orbitals of the individual chain monomers are located predominantly on the small region where chain stacking occurs. The electronic coupling is a critical parameter in determining charge-carrier mobility, with higher values leading to higher mobilities.[53,54]

We note that, to the best of our knowledge, the recent work of Jones *et al*.[55] is a first example of a theoretical study that has related the molecular morphology of a π-conjugated polymer system (P3HT) containing realistically long chains [modeled via coarse-grained (CG) simulations] to the hole mobility, via kinetic Monte-Carlo (KMC) simulations. The hole mobility was approximated through semiempirical quantum-chemical evaluations of the charge-transfer rates between molecular sites following the semiclassical Marcus equation, where the rates are proportional to the square of the electronic couplings. While our approach in the present work does not give a quantitative connection between morphologies and mobilities, it provides a direct, qualitative link.

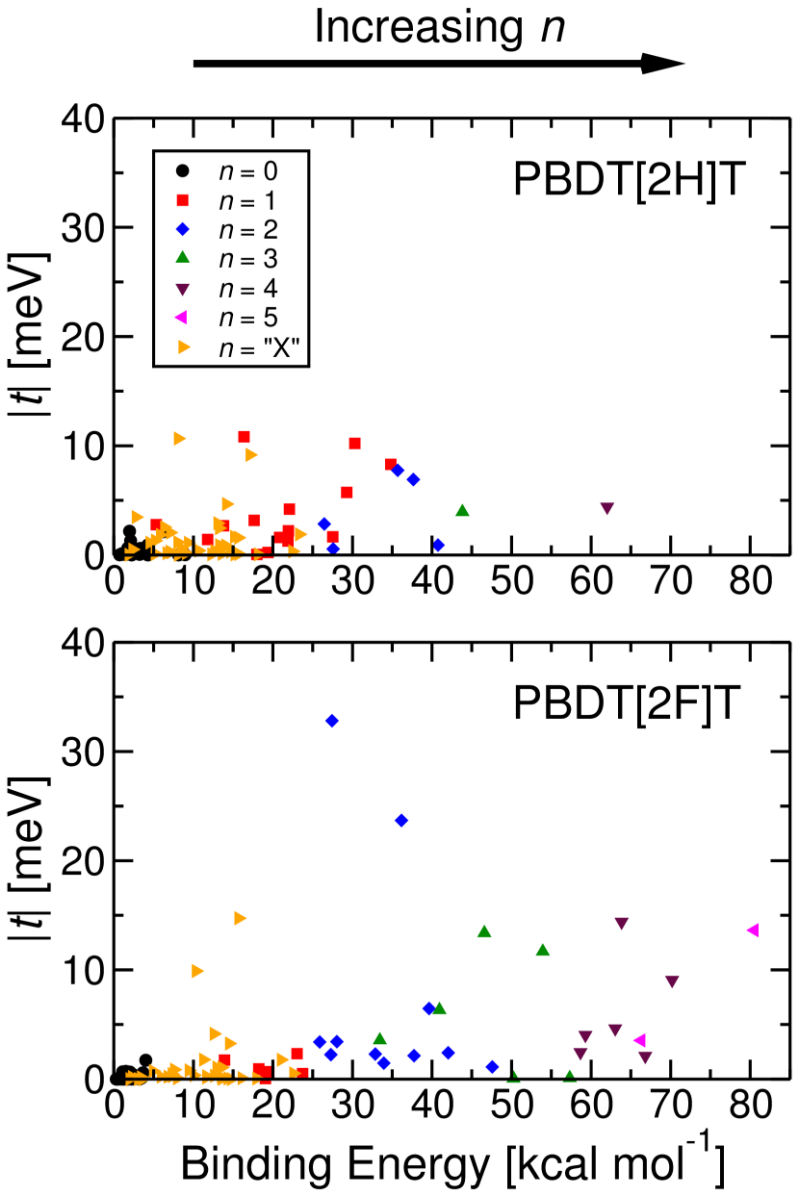

Figure 3.10 Binding energies and electronic couplings *t* between HOMO orbitals, determined from DFT-ωB97XD/6-31G(d,p) calculations, of chain dimers extracted from constant NPT simulations of 80 5-mer chains of PBDT[2X]T at 300 K after cooling from 550 K (note that no correlation is expected nor intended between the two quantities).

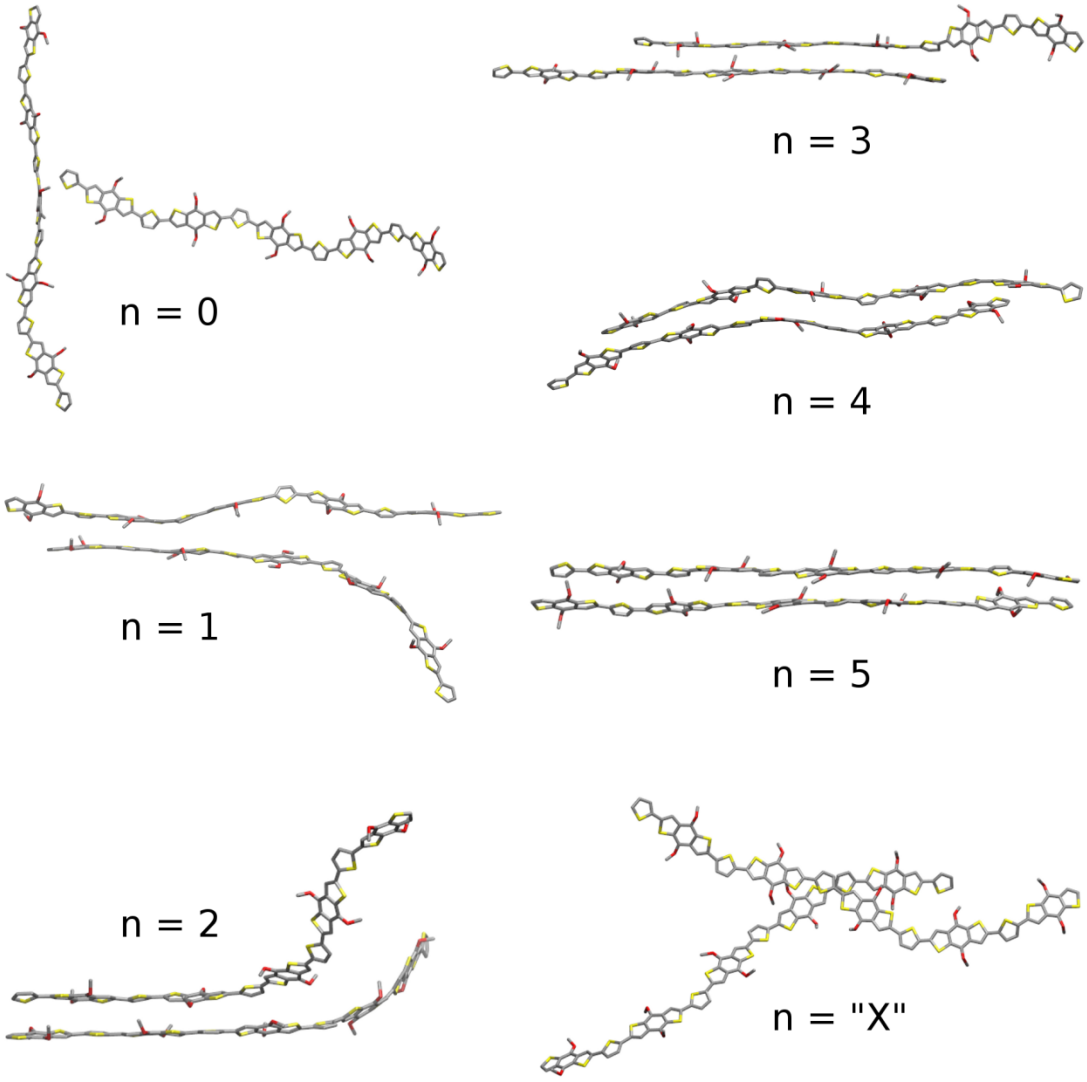

Figure 3.11 Snapshots of representative chain dimers of PBDT[2X]T (coming from [2F]T) corresponding to chain stacking with n = 0, 1, 2, 3, 4, and 5 monomers. n = "X" corresponds to chain dimers that are crossing instead of stacking in parallel. Hydrogen and fluorine atoms are omitted for clarity.

Earlier in our examinations of the inter-monomer dihedral distributions, we observed (via both SS-NMR and MD simulations) that the syn/anti ratio in PBDT[2F]T thin films was shifted towards the syn conformer while the intrinsic inter-monomer torsion profile of PBDT[2F]T depicted an even syn/anti ratio. We now examine this effect in more detail. While it can be

expected that a higher propensity for main-chain planarity can promote chain stacking, the specific pattern of *inter*-molecular arrangement achieved between chains and the inherent electronic effects that promote those specific patterns are important characteristics that require a different level of analysis. In Figure 3.10, the binding energies for (and instances of) chain stacking with $n \geq 3$ are found to be generally higher in PBDT[2F]T than in PBDT[2H]T; this is specifically the case when those are compared in reference to n (degree of stacking). Differences in binding energies suggest variations in how neighboring chains pack. Focusing on extensive chain stacking ($n \geq 4$) as instances where all inter-monomer dihedrals along the neighboring chains contribute to stacking, Figure 3.12 correlates the syn/anti ratio among those dihedrals with the binding energies of the chain dimers in PBDT[2F]T. For $n = 4$, higher syn/anti ratios do clearly correlate with higher binding energies (we note that for $n = 5$, the sample size is too small to observe any correlation). This is an important result that indicates that in addition to the higher propensity for main-chain planarity, the shift in the syn/anti ratio in PBDT[2F]T to the syn conformers contributes to a more energetically favorable chain stacking pattern, which in turn allows for higher degrees of chain stacking order as seen in higher-temperature MD simulations (Figure 3.7). Interestingly, we note that shifting the syn/anti ratio in PBDT[2F]T to larger populations of syn conformers comes at no extra cost in terms of *intra*-molecular energy given the symmetric intrinsic inter-monomer torsion profile of PBDT[2F]T (Figure 3.3). These concurrent analyses underline that, in the design of π-conjugated systems with main-chain substituents, molecular substitutions that can induce a higher propensity for main-chain planarity while allowing for energetically favorable structures with higher binding energies can help achieve higher degrees of packing order in thin-film devices.

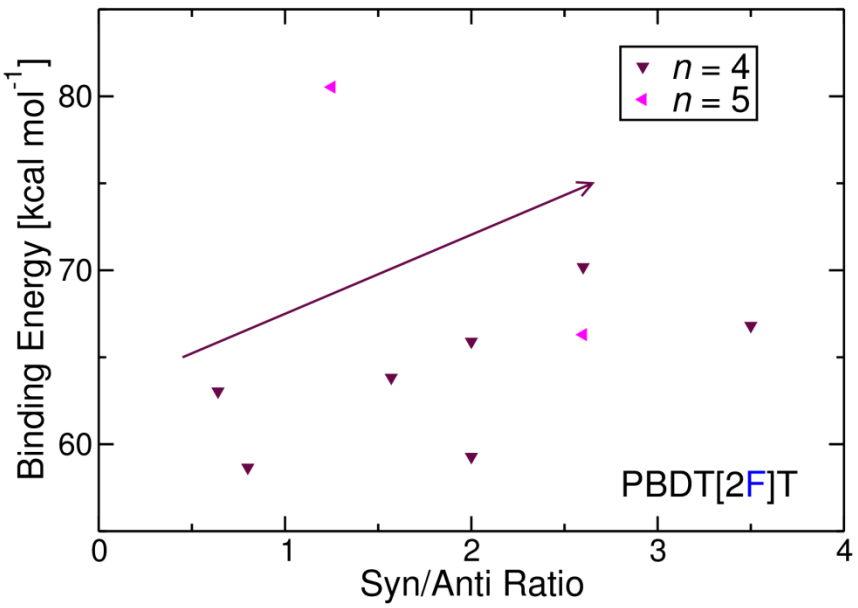

Figure 3.12 Binding energies of PBDT[2F]T chain dimers (with chain stacking of 4 or more monomers) as a function of the syn/anti ratio of the inter-monomer dihedrals along the neighboring chains.

3.4 Conclusions

In this work, we considered the PBDT[2X]T polymers as model systems to elucidate the molecular-scale effects that fluorine substituents induce on main-chain conformations, packing, and electronic couplings. Notably, we exploited a methodology in which we tightly combined quantum-mechanical calculations, molecular dynamics simulations, and solid-state NMR analyses. Among the main results from our work, we emphasize that:

(i) The quantum chemical calculations of the intrinsic inter-monomer torsion profiles along the chains point to a clear propensity for backbone planarity in PBDT[2F]T and lower extents of backbone planarity in PBDT[2H]T. The solid-state NMR analyses and molecular dynamics simulations provide a consistent picture and indicate a

prominence of (near) anti conformations along the PBDT[2H]T chains and coplanar syn conformations along the PBDT[2F]T chains.

(ii) Importantly, compared to PBDT[2H]T, the higher propensity for backbone planarity seen in PBDT[2F]T leads to more pronounced, yet staggered, chain stacking in the solid state.

(iii) As a result, higher inter-chain electronic couplings for holes and larger binding energies between neighboring polymer chains are calculated in the fluorine-substituted polymer, with the former being consistent with the larger hole mobility measured for this material via SCLC experiments.

We note that the molecular-scale effects and electronic characteristics induced by fluorine substituents in the PBDT[2F]T polymers are expected to translate to other fluorine-substituted material systems. Finally, we stress that the protocol followed in this study (thus, combining QC calculations, MD simulations, and solid-state NMR data) can serve in the development of rational design rules to control molecular packing and improve material performance for thin-film OPV and OFET device applications.

3.5 References

(1) Facchetti, A. *Chem. Mater.* **2011**, *23* (3), 733.
(2) Mishra, A.; Bäuerle, P. *Angew. Chem. Int. Ed.* **2012**, *51* (9), 2020.
(3) Wang, C.; Dong, H.; Hu, W.; Liu, Y.; Zhu, D. *Chem. Rev.* **2012**, *112* (4), 2208.
(4) Li, G.; Zhu, R.; Yang, Y. *Nat. Photonics* **2012**, *6* (3), 153.
(5) Lin, Y.; Li, Y.; Zhan, X. *Chem. Soc. Rev.* **2012**, *41* (11), 4245.
(6) Darling, S. B.; You, F. *RSC Adv.* **2013**, *3* (39), 17633.
(7) Søndergaard, R. R.; Hösel, M.; Krebs, F. C. *J. Polym. Sci. Part B Polym. Phys.* **2013**, *51* (1), 16.
(8) Li, Y. *Acc. Chem. Res.* **2012**, *45* (5), 723.
(9) Chochos, C. L.; Tagmatarchis, N.; Gregoriou, V. G. *RSC Adv.* **2013**, *3* (20), 7160.
(10) Wolf, J.; Cruciani, F.; El Labban, A.; Beaujuge, P. M. *Chem. Mater.* **2015**, *27* (12), 4184.
(11) Jo, J. W.; Jung, J. W.; Wang, H.-W.; Kim, P.; Russell, T. P.; Jo, W. H. *Chem. Mater.* **2014**, *26* (14), 4214.
(12) Kim, J.; Yun, M. H.; Kim, G.-H.; Lee, J.; Lee, S. M.; Ko, S.-J.; Kim, Y.; Dutta, G. K.; Moon, M.; Park, S. Y.; Kim, D. S.; Kim, J. Y.; Yang, C. *ACS Appl. Mater. Interfaces* **2014**, *6* (10), 7523.
(13) Carsten, B.; Szarko, J. M.; Son, H. J.; Wang, W.; Lu, L.; He, F.; Rolczynski, B. S.; Lou, S. J.; Chen, L. X.; Yu, L. *J. Am. Chem. Soc.* **2011**, *133* (50), 20468.
(14) Chen, H.-Y.; Hou, J.; Zhang, S.; Liang, Y.; Yang, G.; Yang, Y.; Yu, L.; Wu, Y.; Li, G. *Nat. Photonics* **2009**, *3* (11), 649.
(15) Stuart, A. C.; Tumbleston, J. R.; Zhou, H.; Li, W.; Liu, S.; Ade, H.; You, W. *J. Am. Chem. Soc.* **2013**, *135* (5), 1806.
(16) Yang, L.; Tumbleston, J. R.; Zhou, H.; Ade, H.; You, W. *Energy Environ. Sci.* **2012**, *6* (1), 316.
(17) Briseno, A. L.; Tseng, R. J.; Ling, M.-M.; Falcao, E. H. L.; Yang, Y.; Wudl, F.; Bao, Z. *Adv. Mater.* **2006**, *18* (17), 2320.
(18) Price, S. C.; Stuart, A. C.; Yang, L.; Zhou, H.; You, W. *J. Am. Chem. Soc.* **2011**, *133* (12), 4625.
(19) Schroeder, B. C.; Huang, Z.; Ashraf, R. S.; Smith, J.; D'Angelo, P.; Watkins, S. E.; Anthopoulos, T. D.; Durrant, J. R.; McCulloch, I. *Adv. Funct. Mater.* **2012**, *22* (8), 1663.
(20) Gundlach, D. J.; Royer, J. E.; Park, S. K.; Subramanian, S.; Jurchescu, O. D.; Hamadani, B. H.; Moad, A. J.; Kline, R. J.; Teague, L. C.; Kirillov, O.; Richter, C. A.; Kushmerick, J. G.; Richter, L. J.; Parkin, S. R.; Jackson, T. N.; Anthony, J. E. *Nat. Mater.* **2008**, *7* (3), 216.
(21) Son, H. J.; Wang, W.; Xu, T.; Liang, Y.; Wu, Y.; Li, G.; Yu, L. *J. Am. Chem. Soc.* **2011**, *133* (6), 1885.
(22) Jo, J. W.; Bae, S.; Liu, F.; Russell, T. P.; Jo, W. H. *Adv. Funct. Mater.* **2015**, *25* (1), 120.
(23) Li, W.; Albrecht, S.; Yang, L.; Roland, S.; Tumbleston, J. R.; McAfee, T.; Yan, L.; Kelly, M. A.; Ade, H.; Neher, D.; You, W. *J. Am. Chem. Soc.* **2014**, *136* (44), 15566.
(24) Guo, S.; Ning, J.; Körstgens, V.; Yao, Y.; Herzig, E. M.; Roth, S. V.; Müller-Buschbaum, P. *Adv. Energy Mater.* **2015**, *5* (4), n/a.
(25) Fei, Z.; Boufflet, P.; Wood, S.; Wade, J.; Moriarty, J.; Gann, E.; Ratcliff, E. L.; McNeill, C. R.; Sirringhaus, H.; Kim, J.-S.; Heeney, M. *J. Am. Chem. Soc.* **2015**, *137* (21), 6866.

(26) Zhang, X.; Lu, Z.; Ye, L.; Zhan, C.; Hou, J.; Zhang, S.; Jiang, B.; Zhao, Y.; Huang, J.; Zhang, S.; Liu, Y.; Shi, Q.; Liu, Y.; Yao, J. *Adv*. *Mater*. **2013**, *25* (40), 5791.
(27) Subramanian, S.; Park, S. K.; Parkin, S. R.; Podzorov, V.; Jackson, T. N.; Anthony, J. E. *J*. *Am*. *Chem*. *Soc*. **2008**, *130* (9), 2706.
(28) Nielsen, C. B.; White, A. J. P.; McCulloch, I. *J*. *Org*. *Chem*. **2015**, *80* (10), 5045.
(29) Lei, T.; Dou, J.-H.; Ma, Z.-J.; Yao, C.-H.; Liu, C.-J.; Wang, J.-Y.; Pei, J. *J*. *Am*. *Chem*. *Soc*. **2012**, *134* (49), 20025.
(30) Liu, X.; Hsu, B. B. Y.; Sun, Y.; Mai, C.-K.; Heeger, A. J.; Bazan, G. C. *J*. *Am*. *Chem*. *Soc*. **2014**, *136* (46), 16144.
(31) Jorgensen, W. L.; Maxwell, D. S.; Tirado-Rives, J. *J*. *Am*. *Chem*. *Soc*. **1996**, *118* (45), 11225.
(32) Chai, J.-D.; Head-Gordon, M. *Phys*. *Chem*. *Chem*. *Phys*. **2008**, *10* (44), 6615.
(33) Do, K.; Huang, D. M.; Faller, R.; Moulé, A. J. *Phys*. *Chem*. *Chem*. *Phys*. **2010**, *12* (44), 14735.
(34) Valeev, E. F.; Coropceanu, V.; da Silva Filho, D. A.; Salman, S.; Brédas, J.-L. *J*. *Am*. *Chem*. *Soc*. **2006**, *128* (30), 9882.
(35) Hayashi, S.; Hayamizu, K. *Bull*. *Chem*. *Soc*. *Jpn*. **1991**, *64* (2), 688.
(36) Morcombe, C. R.; Zilm, K. W. *J*. *Magn*. *Reson*. **2003**, *162* (2), 479.
(37) Saalwächter, K.; Schnell, I. *Solid State Nucl*. *Magn*. *Reson*. **2002**, *22* (2–3), 154.
(38) Fung, B. M.; Khitrin, A. K.; Ermolaev, K. *J*. *Magn*. *Reson*. **2000**, *142* (1), 97.
(39) Liu, S.-F.; Mao, J.-D.; Schmidt-Rohr, K. *J*. *Magn*. *Reson*. **2002**, *155* (1), 15.
(40) Feike, M.; Demco, D. E.; Graf, R.; Gottwald, J.; Hafner, S.; Spiess, H. W. *J*. *Magn*. *Reson*. *A* **1996**, *122* (2), 214.
(41) Blanc, F.; Copéret, C.; Lesage, A.; Emsley, L. *Chem*. *Soc*. *Rev*. **2008**, *37* (3), 518.
(42) van Rossum, B.-J.; Förster, H.; de Groot, H. J. M. *J*. *Magn*. *Reson*. **1997**, *124* (2), 516.
(43) Goldburg, W. I.; Lee, M. *Phys*. *Rev*. *Lett*. **1963**, *11* (6), 255.
(44) Saalwächter, K.; Graf, R.; Spiess, H. W. *J*. *Magn*. *Reson*. **2001**, *148* (2), 398.
(45) Karpfen, A.; Choi, C. H.; Kertesz, M. *J*. *Phys*. *Chem*. *A* **1997**, *101* (40), 7426.
(46) Körzdörfer, T.; Brédas, J.-L. *Acc*. *Chem*. *Res*. **2014**, *47* (11), 3284.
(47) Körzdörfer, T.; Sears, J. S.; Sutton, C.; Brédas, J.-L. *J*. *Chem*. *Phys*. **2011**, *135* (20), 204107.
(48) Tonelli, A. E. *NMR Spectroscopy and Polymer Microstructure: The Conformational Connection*; Wiley-VCH, 1989.
(49) Cheeseman, J. R.; Trucks, G. W.; Keith, T. A.; Frisch, M. J. *J*. *Chem*. *Phys*. **1996**, *104* (14), 5497.
(50) Schnell, I.; Spiess, H. W. *J*. *Magn*. *Reson*. **2001**, *151* (2), 153.
(51) Dudenko, D.; Kiersnowski, A.; Shu, J.; Pisula, W.; Sebastiani, D.; Spiess, H. W.; Hansen, M. R. *Angew*. *Chem*. *Int*. *Ed*. **2012**, *51* (44), 11068.
(52) Friedrich, U.; Schnell, I.; Demco, D. E.; Spiess, H. W. *Chem*. *Phys*. *Lett*. **1998**, *285* (1–2), 49.
(53) Coropceanu, V.; Cornil, J.; da Silva Filho, D. A.; Olivier, Y.; Silbey, R.; Brédas, J.-L. *Chem*. *Rev*. **2007**, *107* (4), 926.
(54) Brédas, J. L.; Calbert, J. P.; Filho, D. A. da S.; Cornil, J. *Proc*. *Natl*. *Acad*. *Sci*. **2002**, *99* (9), 5804.
(55) Jones, M. L.; Huang, D. M.; Chakrabarti, B.; Groves, C. *J*. *Phys*. *Chem*. *C* **2016**, *120* (8), 4240.

Chapter 4

Impact of Chemical Functionality on Dynamics, Miscibility, and Morphology in Polymer:Molecule Blends

4.1 Introduction

Organic photovoltaic (OPV) cells are of academic and commercial interest due to their potential for flexible, light-weight, and large-scale solar energy harvesting applications derived from low-cost, high-throughput manufacturing techniques.[1–4] The most prevalent OPV photoactive layer, referred to as a bulk heterojunction (BHJ), is comprised of a solution-processed organic donor:acceptor blend that relies on inherently poor miscibility between the donor and acceptor to form nanoscale phase-separated domains.[1] The donor and acceptor materials can include π-conjugated polymers and/or (small) molecules and oligomers,[5,6] with blends based on polymer donors and fullerene-derivative acceptors typically showing the highest photovoltaic performance.[7]

Fullerene derivatives, particularly [6,6]-phenyl-C_{61}-butyric acid methyl ester ($PC_{61}BM$) and its C_{70} analog ($PC_{71}BM$), possess many properties that lead to high OPV performance, including facile reduction,[8] good electron-transport properties,[9,10] three-dimensional charge-carrier transport, and sufficient phase separation with many donor polymers in solution-cast thin films.[11] Consequently, most efforts in the design of donor systems, and in particular narrow optical-gap conjugated polymers,[12] aim for complementary properties with these fullerene-based acceptors such that the electronic and optical properties of the device are optimized. This includes maximizing: (i) photon absorption within the full solar spectrum; (ii) open-circuit voltage (V_{OC}) by controlling (to a first approximation) the offset between the ionization potential of the donor and the electron affinity of the fullerene; and (iii) charge-transfer state energy at the polymer/fullerene interface. Beyond these properties, the phase-separation thermodynamics and kinetics need to be optimized to control the thin-film morphology, as the latter directly impacts charge-carrier generation, migration, recombination, and collection. As a result, a large

parameter space must be considered for BHJ OPV optimization, including many intrinsic details at the molecular scale. Unfortunately, fullerene derivatives possess a number of drawbacks. For example, although much more costly, $PC_{71}BM$ has been employed in part to address the weak absorption of visible radiation by $PC_{61}BM$, which generally leads to higher OPV performance stemming from increased short-circuit current density (J_{SC}).[13] In addition, the large electron affinities of fullerene derivatives can result in suboptimum V_{OC} when blended with common conjugated polymers such as poly(3-hexylthiophene) (P3HT).[14]

Consequently, recent efforts have focused on developing non-fullerene acceptors to optimize material absorption, miscibility, and material electronic properties to maximize the versatility of selecting donor and acceptor pairs.[14–27] Having a greater selection of donor:acceptor pairs can improve our basic understanding of how features in chemical structure affect each device characteristic, and in particular the formation of the BHJ morphology. Representative non-fullerene acceptors include naphthalene[18] and perylene[19] diimides, oligothiophenes, diketopyrrolopyrroles, vinazenes, rhodamines, and substituted pentacenes.[14–17] Design strategies for these acceptors include: (i) modulating the electronic, redox, and optical properties via chemical substitution of electron-withdrawing groups and/or increasing the π-conjugation pathway; and (ii) influencing solubility/miscibility through substitution of pendant alkyl groups. These strategies are generating increased success, as power conversion efficiencies (PCE) over 7% have now been achieved in polymer:molecule and all-polymer BHJ OPVs.[20–26,28,29]

It is well demonstrated that slight modifications in the chemical structure of organic electronic materials can lead to major changes in pristine and blend film morphologies and their subsequent performance.[17,29–33] In many OPV cells incorporating new acceptors, limiting factors, when compared to their fullerene counterparts, include poor thin-film morphologies – *e.g.*, in the

forms of excessively coarse phase separation or intimate mixtures with insufficient phase separation – and charge-carrier transport characteristics, both of which are a direct consequence of chemical functionality, processing conditions and formulation. While the latter two have been the subject of several experimental investigations,[30–33] the former has been explored far less, especially in the context of non-fullerene acceptors and even less so via computational methods. Therefore, it is desirable to develop a better understanding of the relationships between chemical structure and morphology to improve the performance of non-fullerene acceptors. In drawing connections between acceptor chemical structure and blend microstructure, it is important to elucidate the morphological influences of the electron-withdrawing and alkyl groups, both of which are non-innocent components during film formation. Moreover, it is of special interest to untangle the steric and electrostatic effects these chemical groups may exert on their local environment.

Of particular relevance to this study is previous work by Shu and co-workers, who surveyed a variety of electron-deficient pentacenes as acceptors in BHJ devices with poly(3-hexylthiophene) [P3HT] acting as the donor material.[34] Pentacene-based small molecules are easily amenable to synthetic substitution, which makes them good candidates for comprehensive investigations (Figure 4.1). Device V_{OC} and J_{SC} were found to vary with the electron-withdrawing group and alkyl group substitution, respectively, and correlate with crystal structure packing motifs of the pentacene-based material.[34]

Here, we systematically evaluate, through a series of multi-scale molecular simulations, the structure-function relationships of these pentacene-based acceptors in P3HT to clarify how the chemical structure of the substituted pentacenes influences the blend morphology, which in turn affects OPV performance. We focus specifically on a series of 6,13-bis(trialkylsilylethynyl)-

substituted pentacenes, hereafter simply referred to as acenes, shown in Figure 4.1. The acene structures are varied by the alkyl groups appended to the silicon atoms – including triethyl (TES), tri-isopropyl (TIPS), and tri-cyclopentyl (TCPS) – and by substitution on the *β*-position on the pentacene core with an electron-withdrawing group, either trifluoromethyl (-CF_3) or cyano (-CN), while the unsubstituted core is denoted as -Pn.

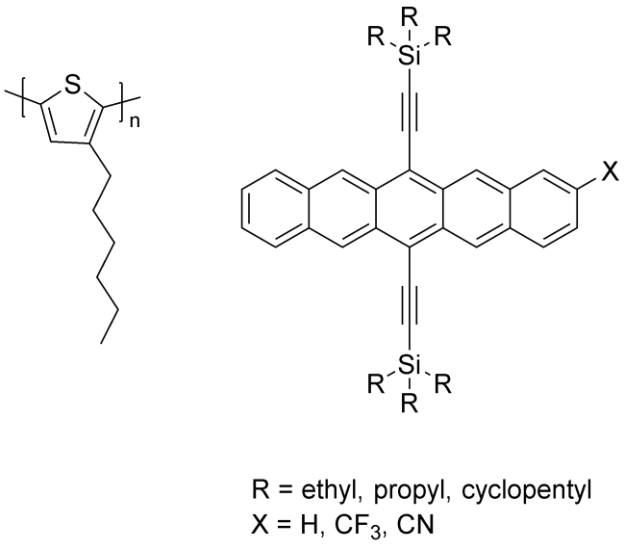

Figure 4.1 Chemical structures of poly(3-hexylthiophene) (left) and trialkylsilylethynyl-substituted pentacene (right).

In our molecular modeling approach, we perform atomistic molecular dynamics (MD) simulations to obtain target structural distributions, which are then used to derive coarse-grained (CG) potentials following the work of Huang *et al*.[35] CG simulations drastically reduce the degrees-of-freedom involved in modeling large systems, which is essential to studying systems with length scales approaching that of the device and for timescales that ensure the possibility of phase separation of the blend component materials.[35–38] These modeling advantages allow us to

build structure-morphology relationships that are relevant to device properties, such as donor-acceptor morphology, miscibility, and interfacial area, and may inform future designs of donor/non-fullerene acceptor combinations. In our mapping scheme, see Figure 4.2, we choose to represent the P3HT monomer and acene molecule with the fewest CG particles possible while retaining the molecular shape and chemical nature of the materials. In this way, we can discern trends in morphological properties and link them to specific features of the chemical structure.

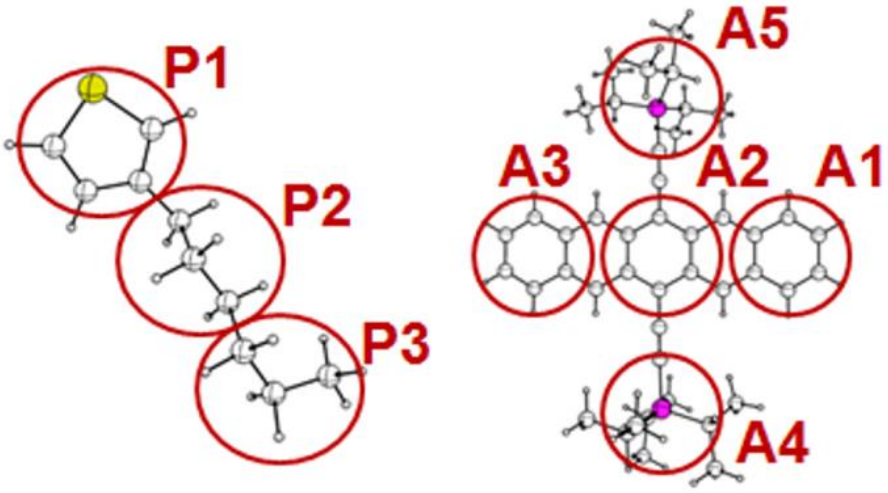

Figure 4.2 Mapping scheme used in the coarse-grained (CG) simulations of P3HT and the acenes (TIPS-Pn as the example). CG sites are constructed from the centers-of-mass of the encircled atoms. A1 is the site on the acene backbone where the electron-withdrawing group is attached.

4.2 Computational Methodologies

Atomistic MD simulations of systems containing pure P3HT, pure acene, and mixed P3HT:acene were performed to obtain target microstructures for the coarse-graining procedure. The pure P3HT system contained 40 decamer chains, which are completely regioregular, and the pure

acene systems each contained 256 molecules. The mixed P3HT:acene systems each contained 40 decamer P3HT chains and a varying number of acene molecules, depending on their type, to construct an approximate 1:1 wt/wt ratio mixture; larger system sizes gave nearly identical structural distributions and thermodynamic properties. The All-Atom Optimized Potentials for Liquid Simulations (OPLS-AA)[39] force field was used for the material systems with some modifications, on the basis of DFT calculations,[40] in the partial charges of the thiophene and in inter-monomer dihedral potentials of P3HT to account for the conjugation of the chain backbone.[35,41] The atomistic MD simulations were performed with a random initial configuration in a cubic box with periodic boundary conditions and in the melt (melting points of P3HT and TIPS-Pn are 511 K and 549 K, respectively)[42] at 550 K and 1 atm (NPT ensemble), using a Nosé-Hoover thermostat[43] and Nosé-Hoover barostat,[44] respectively. A timestep of 1.5 fs was used. Simulations were performed for a total time of at least 10 τ_2 and varied between 25-75 ns depending on the type of acene in the mixture. Distribution functions and quantities of interests were computed from trajectories corresponding to the latter $5\tau_2$ of each simulation, and were checked that they did not vary systematically with time.

The parameters for CG simulations were derived using the iterative Boltzmann inversion (IBI) method following the work of Huang *et al*.,[35] see Chapter 2.3 for details. The CG particles were constructed using the centers-of-mass of groups of atoms as shown in Figure 4.2. The simulations to optimize the CG potentials were performed at constant volume and 550 K in an NVT ensemble. After convergence, the CG potentials were scaled linearly following Equation 2.21 in order to match the density from atomistic simulations at the same thermodynamic conditions. The scaling parameter b_{ij} was chosen to reach a $\leq 2\%$ error in the density. The P3HT-P3HT and acene-acene CG interaction potentials were optimized using the pure P3HT and pure

acene systems, respectively. The P3HT-acene CG interaction potentials were optimized using the mixed P3HT:acene systems while keeping the P3HT-P3HT and acene-acene potentials fixed as obtained from the pure systems.

Having systematically coarse-grained the P3HT:acene mixtures, we performed CG simulations of approximately 1:1 wt/wt ratio mixtures, with each simulation containing approximately 100,000 particles at *ca*. 25 nm length scales. The blend ratio simulated here is equivalent to that used in reported devices.[34] The chain length was 48 monomers, which corresponds to a molecular weight of about 8 kDa. Simulations of significantly longer chains, which would be more relevant to actual devices, were limited by computational feasibility. The CG simulations were performed at 550 K for 120 ns and then cooled from 550 K to 300 K over 200 ns to compare the impact of temperature on the miscibility of each blend. This was followed by 10 ns simulations at 300 K. Initial configurations were random. A timestep of 5.0 fs was used. All simulations were performed using LAMMPS[45] (see lammps.sandia.gov) and the Shaheen Blue Gene/P Supercomputer at KAUST (see ksl.kaust.edu.sa).

4.3 Results and Discussion

As noted earlier, the matrix of nine blends for our simulation studies comprise pentacenes substituted with varying electron-withdrawing and trialkylsilylethynyl groups (Figure 4.1). The electron-withdrawing group is varied between a cyano (-CN) and trifluoromethyl (-CF_3) group, in addition to the unsubstituted case (-Pn). The alkyl chains on the silylethynyl arms are varied among tri-ethyl (TES), tri-isopropyl (TIPS), and tri-cyclopentyl (TCPS) groups. It is expected

that electron-withdrawing group strength and alkyl group size will control the blend miscibility and influence intermolecular packing.

It is instructive to first compare the electron-withdrawing group polarity – and its contribution to the dipole moment of the acene molecule – as it will impact the structure-property relationships. Using the empirically-derived OPLS charges,[39] dipole moments of 2.5 D and 2.8 D are obtained for the "C-CF_3" and "C-CN" group, respectively. Meanwhile, the "C-H" group in the unsubstituted acene has a dipole moment of 0.6 D. The polarity of these electron-withdrawing groups (or lack thereof) – the order of which is emphasized for our discussion below – leads to a range via energy minimization (in increasing order) of 0.0-1.0 D, 2.5-2.7 D, and 3.0-3.5 D for the unsubstituted, CF_3-, and CN-substituted acenes, respectively. Although partial charges obtained from quantum-chemical calculations would give more specific values with respect to the chemical structure of the acene, we expect the qualitative trends in polarity discussed here using OPLS charges to remain intact.

We first examine the connection between chemical structure and molecular dynamics, as characterized by diffusivity, of the simulated atomistic systems. The diffusivity of P3HT and the acenes in their pure and mixed systems is expected to affect the BHJ microstructure during solution-casting and post-production thermal annealing; extensive solution studies are ongoing and are the focus of future work. Figure 4.3 shows a comparison of the orientational and translational diffusivities of P3HT (using the thiophene center-of-mass) in the pure and mixed systems. The orientational diffusion coefficient α, which is the inverse of τ_2, is obtained by fitting the chain auto-correlation function to the equation $\langle P_2[\mathrm{u}(t)\cdot\mathrm{u}(0)]\rangle \approx \exp(-t/\tau_2)$ as described in the Computational Methodology section. The translational diffusion coefficient D is obtained by fitting the mean square displacement to the equation $\langle r^2(t)\rangle \approx 6Dt$.

Both orientational and diffusional types of diffusion decrease with increasing alkyl group size and with electron-withdrawing group strength, with the P3HT diffusivity being generally smaller in mixtures than in the pure polymer; the lone exception is TES-Pn (TES is the smallest alkyl substituent considered and the acene has no electron-withdrawing group). In addition, the decrease in diffusivity, which increases with increasing strength of the electron-withdrawing group, is more dramatic when the alkyl group size is smaller, *i.e.*, the variation in diffusivity is more pronounced for TES-acenes than for TIPS- and TCPS-acenes. The trends here for P3HT diffusivity in pure and mixed systems are likewise observed for the acenes, see Figure B1.

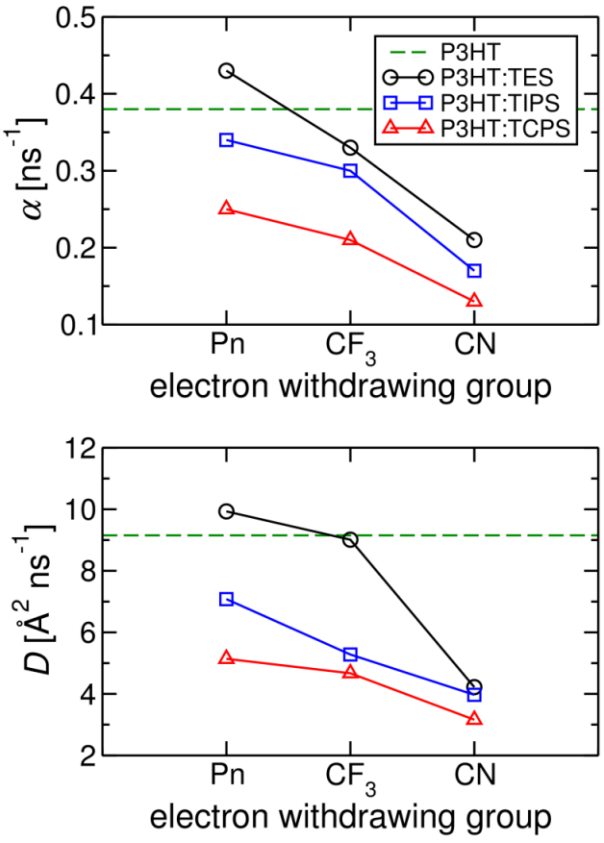

Figure 4.3 P3HT diffusivity in pure and mixed systems determined from atomistic NPT simulations at 550 K and 1 atm. The coefficients α and D correspond to orientational (top plots) and translational (bottom plots) diffusion, respectively.

We next detail the nature of the interactions between P3HT and the acenes, which impacts the diffusive properties of the blends and, as we will show, their miscibility; importantly, the relative interaction among the P3HT and acene will govern the distribution of configurations at the donor-acceptor interface and, in turn, the energy landscape and critical electronic processes relevant to charge generation and solar cell operation.[46–48] Figure 4.4 shows the radial distribution functions (RDFs), $g(r)$, among pairs of sites, defined by taking the centers-of-mass of a thiophene in a P3HT oligomer (P1) and three (distinct) six-carbon rings of the pentacene backbone (A1-A3); note that A1 is the site nearest to the electron-withdrawing group. The RDF measures the probability of finding a site some distance away from a reference site. The location and height/sharpness of the first-order peak (at small distances) indicate the closeness and (energetic) strength, respectively, in the packing of the sites involved. The appearance of secondary and higher-order peaks indicate higher degree of order.

We start with the impact of the alkyl group substitution. The RDFs in TES-acene mixtures contain the highest first-order peaks (Figures 5.4 a, d, g) relative to their TIPS (b, e, h) and TCPS (c, f, i) analogues, indicating that the thiophene rings approach the pentacene backbones more readily, owing to minimal steric hindrance of the ethyl groups. The first-order peaks for the TIPS-acene (Figures 5.4 b, e, h) and TCPS-acene mixtures (Figures 5.4 c, f, i) show marginal difference, hence the steric bulk of the isopropyl and cyclopentyl groups similarly affect the interactions between the thiophene and pentacene backbones.

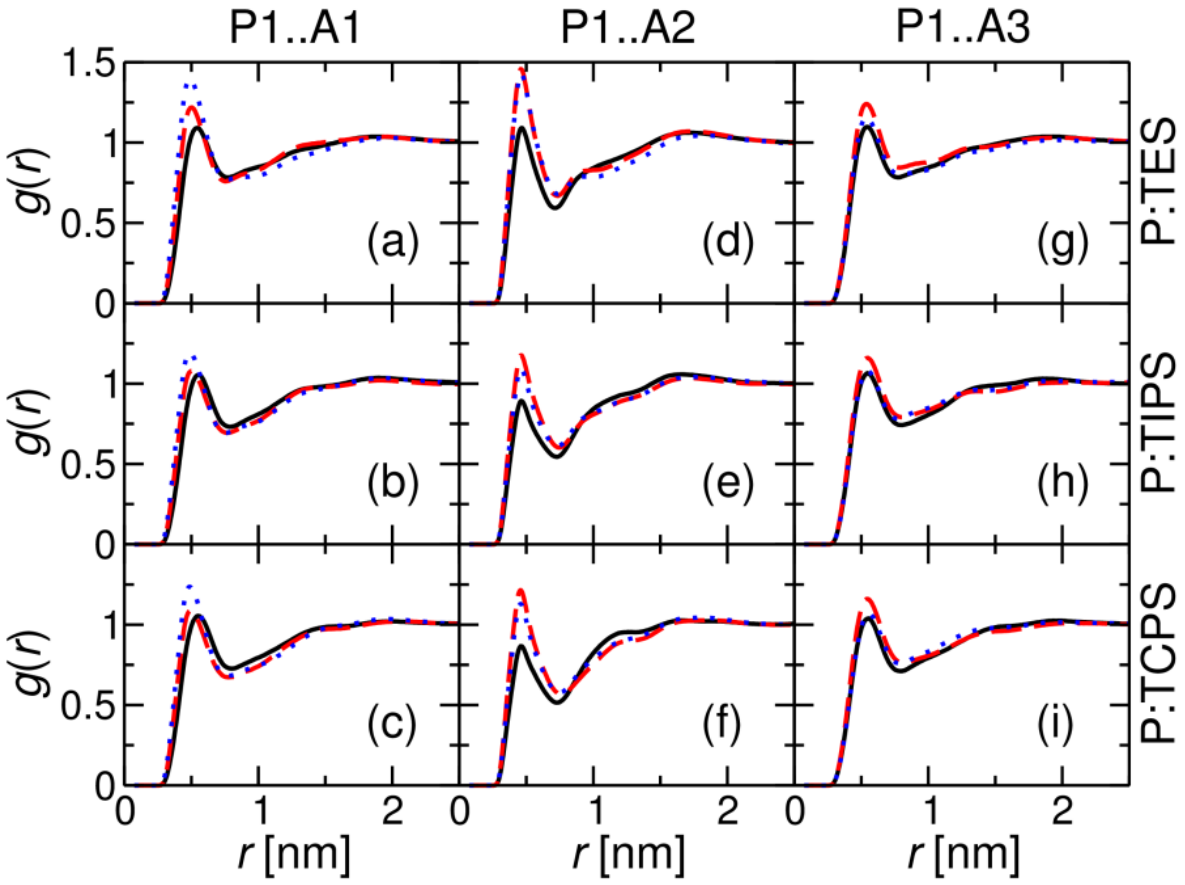

Figure 4.4 Radial distribution functions, $g(r)$, among non-bonded sites P1 of P3HT and A1-A3 of the acenes determined from atomistic NPT simulations of P3HT:acene mixtures at 550 K and 1 atm. Solid, dashed, and dotted lines denote the unsubstituted, CF_3-, and CN-acene, respectively. See Figure 4.2 for site definitions.

We now turn to the influence of the electron-withdrawing group. The CF_3 and CN substitutions systematically give rise to slightly closer and stronger contacts among the thiophene rings and pentacene backbones, characterized by the (mostly) higher first-order peaks when compared to the unsubstituted case across the RDFs. This feature stems in part from the thiophene polarity, with dipole-dipole interactions leading to the stronger contacts between the thiophene rings and the substituted polar pentacene backbones, see for instance the P1..A1 RDFs in Figures 5.4 a-c. Consequently, the P1..A3 RDF peaks for the CN-acenes (Figures 5.4 g-i) decrease to the

equivalence of the unsubstituted case, as the thiophene predominantly settles near A1 and A2. The P1..A2 RDFs (Figures 5.4 d-f), when compared with the P1..A1 RDFs, reveal the relative interplay of the electron-withdrawing group polarity versus steric bulk: The peaks in the P1..A2 RDFs are clearly sharper than those in P1..A1 RDFs for the CF_3-acenes (dashed lines), indicating that the steric hindrance of the tetrahedral CF_3 group outweighs its polar attraction in packing with neighboring thiophenes. On the other hand, the peaks for the CN-acenes (dotted lines) in P1..A1 and P1..A2 RDFs are roughly the same, which shows that the polar attraction of the CN group outweighs the extra steric hindrance when compared to the unsubstituted system. Thus, the trends in diffusivity as a function of electron-withdrawing group discussed above can be directly linked to the thiophene-pentacene interactions.

The trends in thiophene-pentacene interactions discussed so far reveal polar-driven interactions. We now examine the RDFs between sites on the P3HT hexyl-chains and the pentacene backbones, plotted in Figure 4.5; we note that these interactions are relevant to solar-cell performance as they are likely to minimize the important electronic couplings between the conjugated units of P3HT and the acenes. The first-order P3…A1 RDF peaks are clearly sharp for the unsubstituted acenes (solid lines), while the peaks are smaller for CF_3- and CN-acenes (dashed and dotted lines, respectively), due to a combination of the steric bulk and polarity of the electron-withdrawing groups. Furthermore, the first-order peaks and corresponding valleys for CF_3-acenes are flatter when compared to CN-acenes, which points to a lesser degree of order stemming from the more pronounced steric bulk of the tetrahedral CF_3. The P3..A2 and P3..A3 RDFs (Figure B2) are nearly indistinguishable as a function of the chemical structure, suggesting that the alkyl group size does not affect the interactions between the hexyl-chain of P3HT and

the pentacene backbone. Note that the RDF trends obtained from the simulations at 550 K are expected to be more pronounced at lower (room) temperatures.

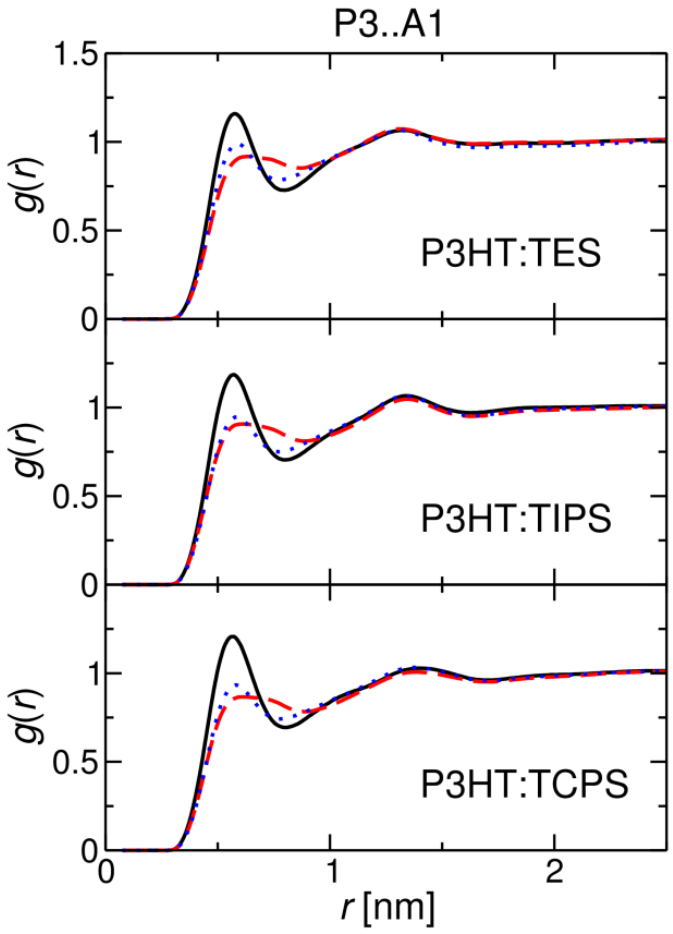

Figure 4.5 Radial distribution functions, $g(r)$, among non-bonded sites P3 of P3HT and A1 of the acenes determined from atomistic NPT simulations of P3HT:acene mixtures at 550 K and 1 atm. Solid, dashed, and dotted lines denote the unsubstituted, CF_3-, and CN-acene, respectively. See Figure 4.2 for site definitions.

The above discussion comparing P3HT-P3HT, acene-acene, and P3HT-acene interactions with elaboration on thiophene-pentacene and hexyl-pentacene interactions is prerequisite to drawing connections between chemical structure and miscibility and/or morphology. Thus, we now shift

our focus to CG simulations of P3HT:acene blends in order to build such structure-property relationships. As mentioned in the Computational Methodology section, we performed CG simulations of P3HT:acene blends at 550 K and at 300 K (by cooling from 550 K over 200 ns).

To quantify miscibility, the normalized demixing parameter $\overline{\psi}_n$ was determined at both thermodynamic conditions, see Figure B3 for data at 550 K; however, we opt to highlight the demixing parameter as a function of temperature over the course of cooling as shown in Figure 4.6. The demixing parameter is defined in Equation 4.1, where n^3 is the total number of cubes into which the system is divided, ρ_i is the density of the i-th cube, and ρ is the global density of the system.[49]

$$\overline{\psi}_n \equiv \frac{1}{n^3}\sum_{i=1}^{n^3}\left|\frac{\rho_i}{\langle\rho\rangle} - 1\right| \tag{4.1}$$

In principle, the lower limit of $\overline{\psi}_n$ is zero, which corresponds to a completely uniform phase where the local and global densities are the same. The upper limit of $\overline{\psi}_n$ is $2V_2/(V_1+V_2)$, where V_1 and V_2 are the volumes of the individual pure systems, and indicates two completely separated phases. However, in practice $\overline{\psi}_n$ cannot be zero due to the fluctuating local densities of each cube and is proportional to the standard deviation of the fluctuations, which decreases with n. More information on the demixing parameter can be found in Ref. 47. Here, $\overline{\psi}_n$ was determined with n = 12 by dividing the simulation box into n^3 cubes with length $l_{cube}=L_{box}/n$, which is $ca.$ 20 Å. Figure 4.6 shows a comparison of $\overline{\psi}_n$ for the P3HT:acene blends during the course of 200 ns where the temperature was cooled from 550 K to 300 K. Each blend started from an initial homogeneously mixed system.

The first notable trend is that acenes with larger alkyl groups result in less mixing with P3HT. The exception is TES-CF_3, which is less mixed than its unsubstituted and CN-substituted analogs. These features suggest that steric hindrance, coming from either the alkyl or electron-withdrawing groups, disrupts close packing and induces less mixing. On the other hand, the polarity of the electron-withdrawing group enhances mixing. The demixing parameter decreases on going from the unsubstituted TIPS- and TCPS-acenes (squares and triangles, respectively) to the CF_3- and CN-substituted analogs. Once again, TES-CF_3 is an exception in addition to TES-CN. In fact, the miscibility of P3HT:TES-acene blends (circles) decreases with the steric hindrance of the electron-withdrawing group, suggesting that steric effects of the electron-withdrawing group dominate in controlling miscibility when the alkyl group is small. Conversely, steric effects of the alkyl groups dominate in controlling miscibility when the alkyl groups are sufficiently larger, *e.g.*, isopropyl and cyclopentyl. In the latter case, variations in miscibility are to a secondary degree controlled by the electron-withdrawing group strength. The trends in P3HT:acene miscibility presented here can be directly attributed to the P1..A1 interactions between thiophene and the pentacene backbone discussed above. Hence, clear connections between the variation in P3HT:acene miscibility can be made to specific intermolecular interactions due to the chemical structure.

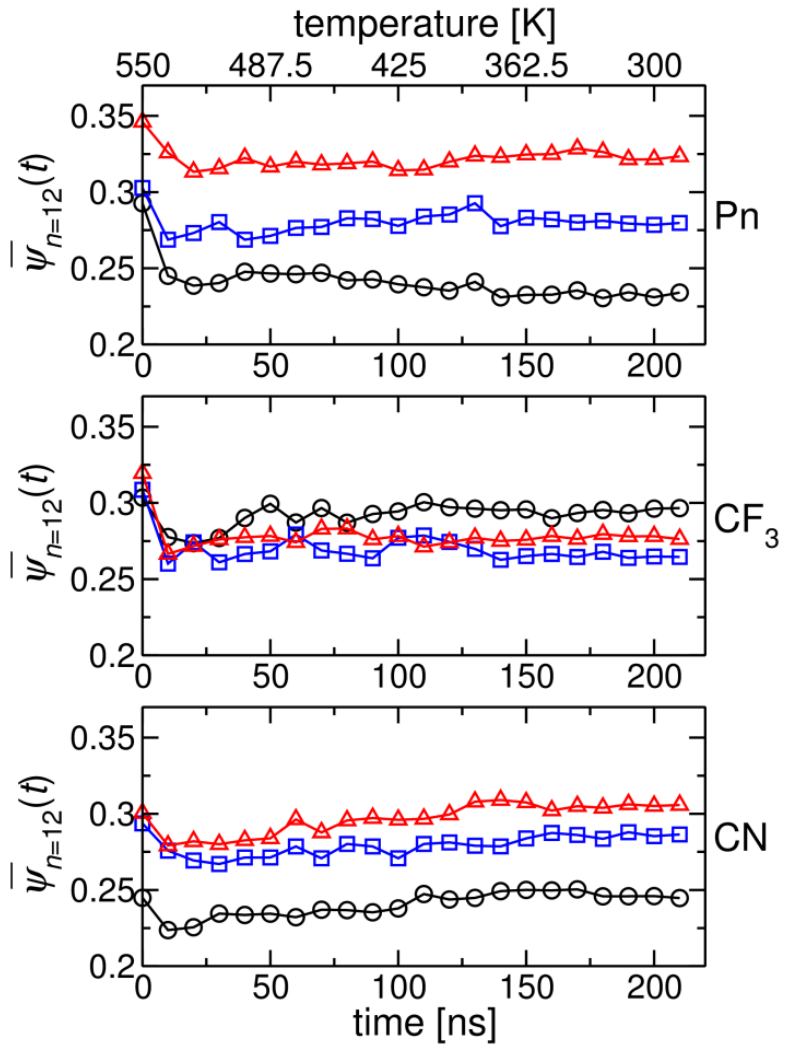

Figure 4.6 Normalized demixing parameter $\overline{\psi}_n$ (n = 12) for P3HT:acene blends determined from CG simulations where the system is cooled from 550 K to 300 K over the course of 200 ns. Circles, squares and triangles denote TES-, TIPS- and TCPS-acenes, respectively.

The discussion of miscibility based on the demixing parameter can vary with the number of cells n^3 used in the calculation. Although trends in miscibility can be deduced from a comparison of the demixing parameter in P3HT:acene blends, a more robust parameter that is directly relevant to experiment is desirable. To this end, we implemented a simple discretization procedure similar to that in Ref. 37 to approximate the interfacial area between "phases" of P3HT and acene. Each

blend system at 300 K is divided into $N = 48$ cubes, giving a cube size of ≈5 Å (roughly the volume of a CG particle when taking the average distance at the onset of the first-order peaks in their RDFs with other particles in the system). Each cube is then assigned as a blue (P3HT) or yellow (acene) cube, see Figure 4.7, depending on which material has the majority volume in the cube. The interfacial area is then computed between cubes of different color and is normalized by the total area between cubes, therefore giving a relative percent value.

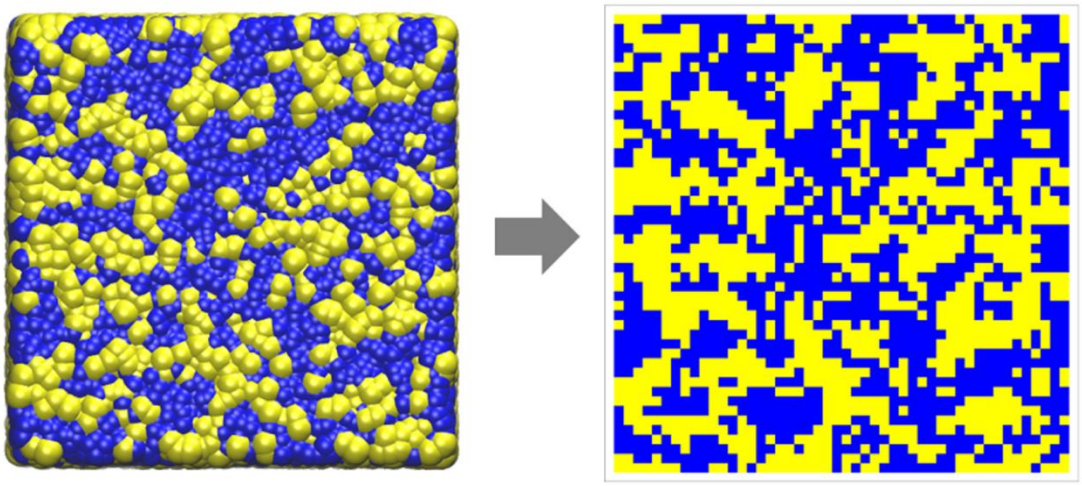

Figure 4.7 Illustration of the discretization procedure used to approximate the interfacial area among the P3HT (blue) and acene (yellow) "phases." Each cube is assigned to P3HT or acene depending on which material has the majority volume in the cube.

A comparison of the relative interfacial area for the P3HT:acene blends is shown in Figure 4.8. The trends in interfacial area parallel those deduced from the demixing parameter, see Figure 4.6, namely that acenes with larger alkyl groups lead to lower miscibility and hence smaller interfacial area (rectangles in Figure 4.8). The trends for CF_3-acenes are less clear (circle in Figure 4.8), which suggests that the miscibilities of these acenes are too similar for our simple

discretization method to discern their order of interfacial area. According to the demixing parameter, TCPS-CF_3 is expected to have an interfacial area in between those of its TES and TIPS analogues; however, the former has a slightly larger area than the latters. In general, the range of interfacial area (and miscibility) for these blends is relatively narrow, between 33 to 39%, which means that any marked variations observed in BHJ thin-film morphology should be expected to arise from solubility differences in these materials and/or crystallization features, which are not likely captured in these CG simulations. Studying the solubility of P3HT:acene blends in solution and the effect of solvent on the formation of the blend morphology is the subject of our future work. We note that the ability to systematically control interfacial area, domain sizes, and interfacial phase mixing – *i.e.*, the composition of the mixed phase layer at the interface between pure donor and acceptor domains – would allow better control of charge-carrier recombination, which is important for device properties such as V_{OC}.[50]

Recent works have used similar coarse-graining methods to investigate the optimal blending ratios of P3HT:PCBM and poly(2,5-bis(3-alkylthiophen-2-yl)thieno[3,2-b]thiophene [PBTTT]:PCBM blends.[36,37] The P3HT:acene blends here at ~1:1 wt/wt ratio exhibit similarly high miscibility as those of P3HT:PCBM and PBTTT:PCBM at the same blend ratio. Given these similar miscibilities between the P3HT:acene blends and P3HT:PCBM, we expect that phase separation in the acene-blends will be led by crystallization (or the lack thereof) of P3HT and the acene molecules, as it is in PCBM-blends.[33,51] For P3HT:PCBM blends, pure amorphous phases of the component materials are negligible; miscibility studies[52,53] have shown three distinct phases: crystalline P3HT, crystalline PCBM, and mixed amorphous P3HT with significant concentrations of PCBM. Again, given that the miscibilities of the P3HT:acene blends are similar to that of P3HT:PCBM, we expect to see similar patterns in the types of

phases present in the BHJ morphology. It should be stressed that any complete model describing the formation of the BHJ morphology should be able to capture the crystallization of the component materials. The coarse-graining methods used here are unlikely to reproduce precise crystal structures and unit-cell parameters given that hydrogen and π-interactions have been averaged out and that planar rings are represented as "spheres", which increases the steric bulk in their interactions. However, the aggregation of π-conjugated polymers in the bulk[54] and solution[41] has been shown to reproduce correctly the lamellar packing in simulations using similar coarse-graining methods. In fact, the atomistic force field for P3HT used here is the same as that in Ref. 41, which lends support to the validity of our model. Studies examining the crystallization of P3HT and the acene molecules, and their behavior in solution are the subject of our future work.

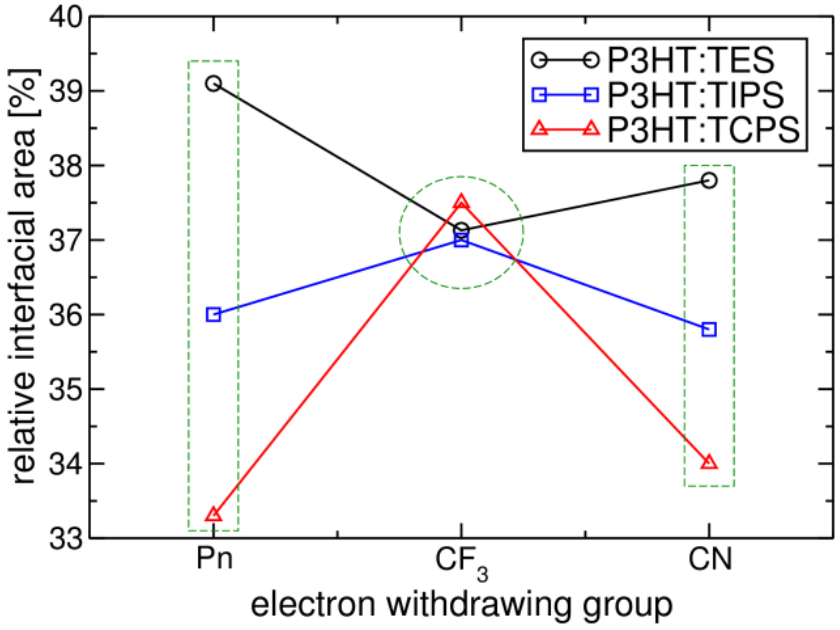

Figure 4.8 Relative interfacial area between P3HT (donor) and acene (acceptor) cubes computed from discretized models of the P3HT:acene blends at 300 K.

So far, we have drawn connections linking the chemical structure of the acene with molecular diffusivity, donor-acceptor interactions, miscibility, and interfacial area in blends with P3HT. We now inspect the effect of miscibility on the structure of P3HT chains in the blend, namely the gyration radius, R_g. Larger values of R_g indicate extended chains while lower values indicate folded or coiled chains. Figure 4.9 shows the average gyration radius as a function of the demixing parameter as determined from 10 ns of CG simulations at 300 K (after being cooled from 550 K). The green arrow in Figure 4.9 highlights the positive relationship between the two parameters such that lower miscibility facilitates more extended chains in the blend. Although the range of R_g is narrow for our blends owing to the computationally-limited short chains, the trends are apparent and expected to become more pronounced when longer chains and larger system sizes are modeled. Extended chains in the blend morphology can be more favorable in solar-cell operation as they can bridge segregated ordered domains as "tie-chains," and facilitate more efficient pathways for charge carriers to reach electrodes.[55]

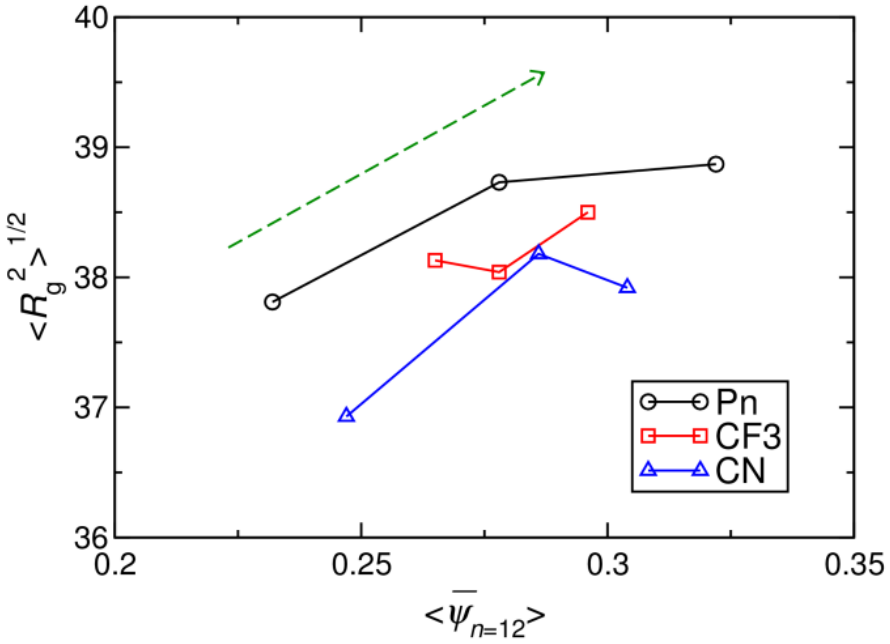

Figure 4.9 Relationship between the gyration radius of P3HT and the demixing parameter in P3HT:acene blends determined from CG simulations at 300 K.

4.4 Conclusions

Molecular simulations of P3HT:acene blends have been performed to determine structure-morphology relationships relevant to organic BHJ solar-cell performance. By focusing on a matrix of nine acenes whose chemical structure is systematically varied in the nature of the alkyl groups and electron-withdrawing groups, connections between the chemical structure of the acene and P3HT and the molecular-scale properties within the blend can be made.

The main results from our work are:

- Diffusivity is observed to generally decrease with size of the alkyl group and strength of the electron-withdrawing group on the acene.

- Donor-acceptor interactions are enhanced by the electron-withdrawing group strength, but diminished primarily by steric bulk of the alkyl groups.
- The blend miscibility generally decreases with alkyl group size and increases with electron-withdrawing group strength.
- The trends in interfacial area between P3HT:acene "phases" reflect those in miscibility.
- Blends with lower miscibility contain more extended P3HT chains.

Importantly, the simulations employed here help to clarify molecular-scale mechanisms contributing to these materials properties. While our simulations consider only a small class of molecules, the systematic structure-property relationships detailed showcase the ability to systematically tailor organic electronic materials with specific morphological properties, as well as the power of molecular simulations to provide details that can relate to molecular design.

4.5 References

(1) Brabec, C. J.; Gowrisanker, S.; Halls, J. J. M.; Laird, D.; Jia, S.; Williams, S. P. *Adv*. *Mater*. **2010**, *22* (34), 3839.
(2) Darling, S. B.; You, F. *RSC Adv*. **2013**, *3* (39), 17633.
(3) Scharber, M. C.; Sariciftci, N. S. *Prog*. *Polym*. *Sci*. **2013**, *38* (12), 1929.
(4) Søndergaard, R. R.; Hösel, M.; Krebs, F. C. *J*. *Polym*. *Sci*. *Part B Polym*. *Phys*. **2013**, *51* (1), 16.
(5) Facchetti, A. *Mater*. *Today* **2013**, *16* (4), 123.
(6) Walker, B.; Kim, C.; Nguyen, T.-Q. *Chem*. *Mater*. **2011**, *23* (3), 470.
(7) He, Y.; Li, Y. *Phys*. *Chem*. *Chem*. *Phys*. **2011**, *13* (6), 1970.
(8) Xie, Q.; Perez-Cordero, E.; Echegoyen, L. *J*. *Am*. *Chem*. *Soc*. **1992**, *114* (10), 3978.
(9) Tummala, N. R.; Mehraeen, S.; Fu, Y.-T.; Risko, C.; Brédas, J.-L. *Adv*. *Funct*. *Mater*. **2013**, *23* (46), 5800.
(10) Wöbkenberg, P. H.; Bradley, D. D. C.; Kronholm, D.; Hummelen, J. C.; de Leeuw, D. M.; Cölle, M.; Anthopoulos, T. D. *Synth*. *Met*. **2008**, *158* (11), 468.
(11) Cates, N. C.; Gysel, R.; Beiley, Z.; Miller, C. E.; Toney, M. F.; Heeney, M.; McCulloch, I.; McGehee, M. D. *Nano Lett*. **2009**, *9* (12), 4153.
(12) Jhuo, H.-J.; Yeh, P.-N.; Liao, S.-H.; Li, Y.-L.; Cheng, Y.-S.; Chen, S.-A. *J*. *Chin*. *Chem*. *Soc*. **2014**, *61* (1), 115.
(13) Wienk, M. M.; Kroon, J. M.; Verhees, W. J. H.; Knol, J.; Hummelen, J. C.; van Hal, P. A.; Janssen, R. A. J. *Angew*. *Chem*. *Int*. *Ed*. **2003**, *42* (29), 3371.
(14) Lin, Y.; Li, Y.; Zhan, X. *Chem*. *Soc*. *Rev*. **2012**, *41* (11), 4245.
(15) Anthony, J. E. *Chem*. *Mater*. **2011**, *23* (3), 583.
(16) Chochos, C. L.; Tagmatarchis, N.; Gregoriou, V. G. *RSC Adv*. **2013**, *3* (20), 7160.
(17) Sonar, P.; Singh, S. P.; Li, Y.; Ooi, Z.-E.; Ha, T.; Wong, I.; Soh, M. S.; Dodabalapur, A. *Energy Environ*. *Sci*. **2011**, *4* (6), 2288.
(18) Guo, X.; Kim, F. S.; Seger, M. J.; Jenekhe, S. A.; Watson, M. D. *Chem*. *Mater*. **2012**, *24* (8), 1434.
(19) Zhang, X.; Lu, Z.; Ye, L.; Zhan, C.; Hou, J.; Zhang, S.; Jiang, B.; Zhao, Y.; Huang, J.; Zhang, S.; Liu, Y.; Shi, Q.; Liu, Y.; Yao, J. *Adv*. *Mater*. **2013**, *25* (40), 5791.
(20) Zang, Y.; Li, C.-Z.; Chueh, C.-C.; Williams, S. T.; Jiang, W.; Wang, Z.-H.; Yu, J.-S.; Jen, A. K.-Y. *Adv*. *Mater*. **2014**, *26* (32), 5708.
(21) Lin, Y.; Wang, J.; Zhang, Z.-G.; Bai, H.; Li, Y.; Zhu, D.; Zhan, X. *Adv*. *Mater*. **2015**, *27* (7), 1170.
(22) Liu, Y.; Mu, C.; Jiang, K.; Zhao, J.; Li, Y.; Zhang, L.; Li, Z.; Lai, J. Y. L.; Hu, H.; Ma, T.; Hu, R.; Yu, D.; Huang, X.; Tang, B. Z.; Yan, H. *Adv*. *Mater*. **2015**, *27* (6), 1015.
(23) Holliday, S.; Ashraf, R. S.; Nielsen, C. B.; Kirkus, M.; Röhr, J. A.; Tan, C.-H.; Collado-Fregoso, E.; Knall, A.-C.; Durrant, J. R.; Nelson, J.; McCulloch, I. *J*. *Am*. *Chem*. *Soc*. **2015**, *137* (2), 898.
(24) Mu, C.; Liu, P.; Ma, W.; Jiang, K.; Zhao, J.; Zhang, K.; Chen, Z.; Wei, Z.; Yi, Y.; Wang, J.; Yang, S.; Huang, F.; Facchetti, A.; Ade, H.; Yan, H. *Adv*. *Mater*. **2014**, *26* (42), 7224.
(25) Zhou, Y.; Kurosawa, T.; Ma, W.; Guo, Y.; Fang, L.; Vandewal, K.; Diao, Y.; Wang, C.; Yan, Q.; Reinspach, J.; Mei, J.; Appleton, A. L.; Koleilat, G. I.; Gao, Y.; Mannsfeld, S. C. B.; Salleo, A.; Ade, H.; Zhao, D.; Bao, Z. *Adv*. *Mater*. **2014**, *26* (22), 3767.
(26) Earmme, T.; Hwang, Y.-J.; Subramaniyan, S.; Jenekhe, S. A. *Adv*. *Mater*. **2014**, *26* (35), 6080.

(27) Bloking, J. T.; Han, X.; Higgs, A. T.; Kastrop, J. P.; Pandey, L.; Norton, J. E.; Risko, C.; Chen, C. E.; Brédas, J.-L.; McGehee, M. D.; Sellinger, A. *Chem*. *Mater*. **2011**, *23* (24), 5484.
(28) Hwang, Y.-J.; Courtright, B. A. E.; Ferreira, A. S.; Tolbert, S. H.; Jenekhe, S. A. *Adv*. *Mater*. **2015**, *27* (31), 4578.
(29) Ye, L.; Jiao, X.; Zhou, M.; Zhang, S.; Yao, H.; Zhao, W.; Xia, A.; Ade, H.; Hou, J. *Adv*. *Mater*. **2015**, *27* (39), 6046.
(30) Chou, K. W.; Yan, B.; Li, R.; Li, E. Q.; Zhao, K.; Anjum, D. H.; Alvarez, S.; Gassaway, R.; Biocca, A.; Thoroddsen, S. T.; Hexemer, A.; Amassian, A. *Adv*. *Mater*. **2013**, *25* (13), 1923.
(31) Bartelt, J. A.; Beiley, Z. M.; Hoke, E. T.; Mateker, W. R.; Douglas, J. D.; Collins, B. A.; Tumbleston, J. R.; Graham, K. R.; Amassian, A.; Ade, H.; Fréchet, J. M. J.; Toney, M. F.; McGehee, M. D. *Adv*. *Energy Mater*. **2013**, *3* (3), 364.
(32) Yang, X.; Loos, J.; Veenstra, S. C.; Verhees, W. J. H.; Wienk, M. M.; Kroon, J. M.; Michels, M. A. J.; Janssen, R. A. J. *Nano Lett*. **2005**, *5* (4), 579.
(33) Campoy-Quiles, M.; Ferenczi, T.; Agostinelli, T.; Etchegoin, P. G.; Kim, Y.; Anthopoulos, T. D.; Stavrinou, P. N.; Bradley, D. D. C.; Nelson, J. *Nat*. *Mater*. **2008**, *7* (2), 158.
(34) Shu, Y.; Lim, Y.-F.; Li, Z.; Purushothaman, B.; Hallani, R.; Kim, J. E.; Parkin, S. R.; Malliaras, G. G.; Anthony, J. E. *Chem*. *Sci*. **2011**, *2* (2), 363.
(35) Huang, D. M.; Faller, R.; Do, K.; Moulé, A. J. *J*. *Chem*. *Theory Comput*. **2010**, *6* (2), 526.
(36) Lee, C.-K.; Pao, C.-W. *J*. *Phys*. *Chem*. *C* **2012**, *116* (23), 12455.
(37) Lee, C.-K.; Pao, C.-W.; Chu, C.-W. *Energy Environ*. *Sci*. **2011**, *4* (10), 4124.
(38) Jankowski, E.; Marsh, H. S.; Jayaraman, A. *Macromolecules* **2013**, *46* (14), 5775.
(39) Jorgensen, W. L.; Maxwell, D. S.; Tirado-Rives, J. *J*. *Am*. *Chem*. *Soc*. **1996**, *118* (45), 11225.
(40) Darling, S. B.; Sternberg, M. *J*. *Phys*. *Chem*. *B* **2009**, *113* (18), 6215.
(41) Schwarz, K. N.; Kee, T. W.; Huang, D. M. *Nanoscale* **2013**, *5* (5), 2017.
(42) Sigma-Aldrich Catalog www.sigmaaldrich.com.
(43) Hoover, W. G. *Phys*. *Rev*. *A* **1985**, *31* (3), 1695.
(44) Hoover, W. G. *Phys*. *Rev*. *A* **1986**, *34* (3), 2499.
(45) Plimpton, S. *J*. *Comput*. *Phys*. **1995**, *117* (1), 1.
(46) Sweetnam, S.; Graham, K. R.; Ngongang Ndjawa, G. O.; Heumüller, T.; Bartelt, J. A.; Burke, T. M.; Li, W.; You, W.; Amassian, A.; McGehee, M. D. *J*. *Am*. *Chem*. *Soc*. **2014**, *136* (40), 14078.
(47) Graham, K. R.; Erwin, P.; Nordlund, D.; Vandewal, K.; Li, R.; Ngongang Ndjawa, G. O.; Hoke, E. T.; Salleo, A.; Thompson, M. E.; McGehee, M. D.; Amassian, A. *Adv*. *Mater*. **2013**, *25* (42), 6076.
(48) Burke, T. M.; McGehee, M. D. *Adv*. *Mater*. **2014**, *26* (12), 1923.
(49) Huang, D. M. *Aust*. *J*. *Chem*. **2014**, *67* (4), 585.
(50) Vandewal, K.; Widmer, J.; Heumueller, T.; Brabec, C. J.; McGehee, M. D.; Leo, K.; Riede, M.; Salleo, A. *Adv*. *Mater*. **2014**, *26* (23), 3839.
(51) Chirvase, D.; Parisi, J.; Hummelen, J. C.; Dyakonov, V. *Nanotechnology* **2004**, *15* (9), 1317.
(52) Collins, B. A.; Gann, E.; Guignard, L.; He, X.; McNeill, C. R.; Ade, H. *J*. *Phys*. *Chem*. *Lett*. **2010**, *1* (21), 3160.

(53) Collins, B. A.; Tumbleston, J. R.; Ade, H. *J*. *Phys*. *Chem*. *Lett*. **2011**, *2* (24), 3135.
(54) Vettorel, T.; Meyer, H. *J*. *Chem*. *Theory Comput*. **2006**, *2* (3), 616.
(55) Noriega, R.; Rivnay, J.; Vandewal, K.; Koch, F. P. V.; Stingelin, N.; Smith, P.; Toney, M. F.; Salleo, A. *Nat*. *Mater*. **2013**, *12* (11), 1038.

Chapter 5

Evolution of the Electronic Properties of P3HT:IDTBR:IFBR Ternary Blends as a Function of Blend Composition

5.1 Introduction

In Chapters 3 and 4, we focused on binary-blend systems consisting of a single donor (D) and acceptor (A), where the polymer donor is the primary light-absorbing component. Bulk-heterojunction (BHJ) organic solar cells (OSCs) employing binary blends of this kind are the most commonly studied in the literature. The strategy to optimize photovoltaic (PV) performance has been to maximize the absorption of the solar spectrum while minimizing the energy losses due to thermalization after absorption; the former raises the short-circuit current density (J_{SC}) while the latter raises the open-circuit voltage (V_{OC}).[1] (Recall from Chapter 1 that the power conversion efficiency (PCE or η) follows the relation: $\eta = J_{SC}V_{OC}FF / P_{in}$, where FF and P_{in} are the fill factor and input power density, respectively.) Maximizing absorption, then, requires a small optical gap (E_{opt}) for the donor, where E_{opt} is often crudely approximated by the HOMO-LUMO gap. Therefore, for a given acceptor, to achieve a high J_{SC} would mean a shallow HOMO(D), see Figure 5.1a,[1] while a high V_{OC} would be favored by a deep HOMO(D). Consequently, efforts aiming to optimize PV efficiency in binary-blend devices have focused on finding the best compromise between maximizing J_{SC} and V_{OC} simultaneously. The ultimate performance attainable by this strategy, however, is estimated to be around 12% PCE for binary-blend devices.[2]

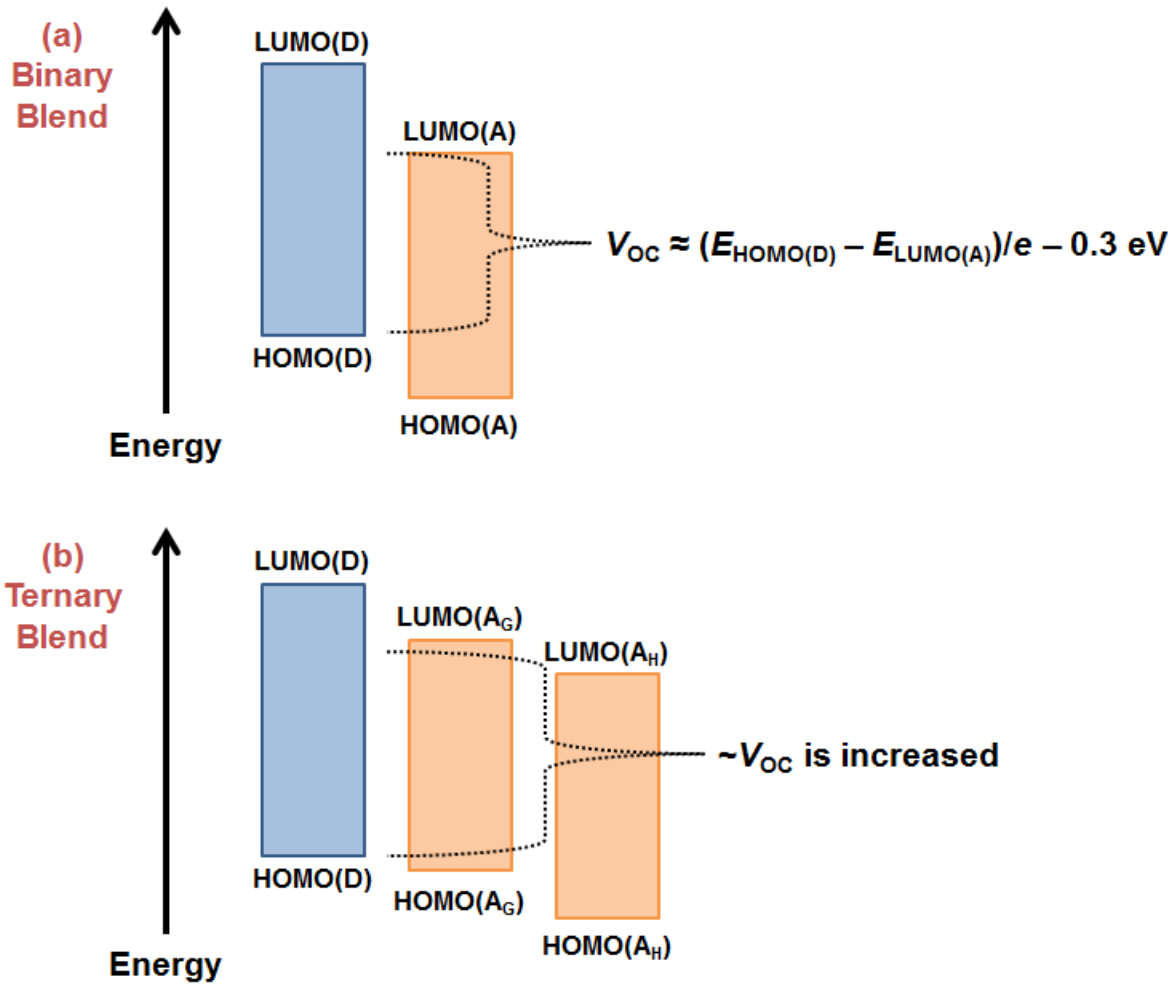

Figure 5.1 Schematic energy level diagrams showing the frontier orbitals of (a) the donor and acceptor in a binary blend and (b) the donor and host (H) and guest (G) acceptors in a ternary blend. The empirical relation between the V_{OC} and the HOMO(D)-LUMO(A) energy gap is also shown for the binary blend.[3] The V_{OC} can be increased through the addition of a third complementary component (a guest acceptor in this case), where it is not necessarily pinned to the lower-lying LUMO level of the acceptors.

Recently, OSCs employing ternary blends have garnered significant attention, motivated by the rationale that both J_{SC} and V_{OC} can be maximized without the expense of one another through the addition of a third complementary component.[4,5] Ternary blends can consist of two donors and one acceptor or vice-versa and employ polymers or small molecules. For our discussion, we will focus on a ternary blend with two acceptors, see Figure 5.1b. The introduction of a guest

acceptor allows for complementary absorption to that of the donor, thereby covering the solar spectrum more completely. At the same time, the modified energy cascade (Figure 5.1b) presents a pathway to achieve a higher V_{OC}, which is not necessarily pinned to the lower-lying LUMO level of the host acceptor.[6] The work of Barry Thompson and coworkers[6,7] has demonstrated the tunability of the V_{OC} as a function of blend composition in ternary-blend devices where the dual donors or acceptors are sufficiently well intermixed. In contrast, the V_{OC} is seen to be pinned by the lower-lying [higher-lying] LUMO [HOMO] level of the acceptors [donors] when the system exhibits high phase-separation. Many studies have reported on the enhancement of the V_{OC} for ternary blends as compared to the binary reference, where the V_{OC} shows a dependence on the blend composition of the dual donors[7–10] or acceptors.[1,11] Moreover, kinetic Monte Carlo simulation results have indicated that cascaded energy heterojunctions lead to reduced geminate recombination.[12] The above factors have culminated in efficiencies exceeding 8% for ternary-blend devices.

In this Chapter, we focus on studying a ternary-blend system consisting of donor poly(3-hexylthiophene) (P3HT) and acceptors containing indacenodithiophene (IDTBR) and indenofluorene (IFBR) flanked by 3-ethylrhodanine, see Figure 5.2. We will hereafter use "IXBR" when referring to both molecules. The acceptor molecules were developed by our collaborators, the Iain McCulloch groups at Imperial College London and King Abdullah University of Science and Technology. The motivation for developing the rhodanine molecules as acceptors is to realize inexpensive and scalable alternatives to fullerene-based acceptors, which are also high-performing.[13] Similarly, P3HT is a very low-cost material to produce, making the entire ternary components very attractive and practical as active-layer materials.

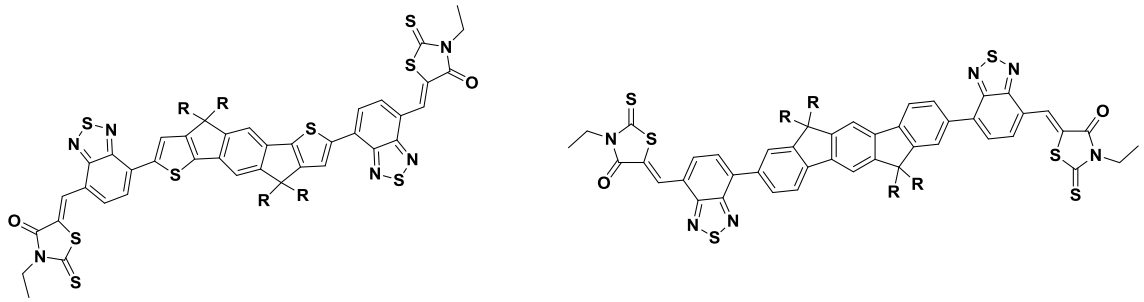

Figure 5.2 Chemical structures of the rhodanine molecules, IDTBR (left) and IFBR (right). R denotes octyl groups.

OSCs employing a ternary blend of P3HT:IDTBR:IFBR with varying weight ratios have been investigated by the McCulloch group and reveal a functional dependence of the performance parameters on the blend ratios of the rhodanine acceptors, see Figure 5.3. The highest performance is achieved for the 70:30 IDTBR:IFBR blend, where the polymer:rhodanine weight ratio is 1:1. Comparing the P3HT:IDTBR and P3HT:IFBR binary references, a much larger V_{OC} is measured for IFBR (0.89 V) versus IDTBR (0.72 V), which is attributed to the smaller electron affinity (EA) [or higher LUMO level] of IFBR. Conversely, the J_{SC} is substantially higher for IDTBR (13.9 mA cm^{-2}) versus IFBR (7.4 mA cm^{-2}), which is attributed to the better complementary light absorption with P3HT due to the smaller E_{opt} for IDTBR (1.63 eV) versus IFBR (2.07 eV) [see Figure 5.4 for the external quantum efficiency (EQE) profiles] and better electron-transport properties in IDTBR. At the optimized blend ratio of 70:30 IDTBR:IFBR (Figure 5.3), the J_{SC} remains high which is characteristic of the IDTBR reference while the V_{OC} is markedly enhanced through the addition of IFBR. To the best of our knowledge, the 7.6% efficiency for the optimal blend ratio is the highest achieved for P3HT-based devices and among the highest for nonfullerene devices.

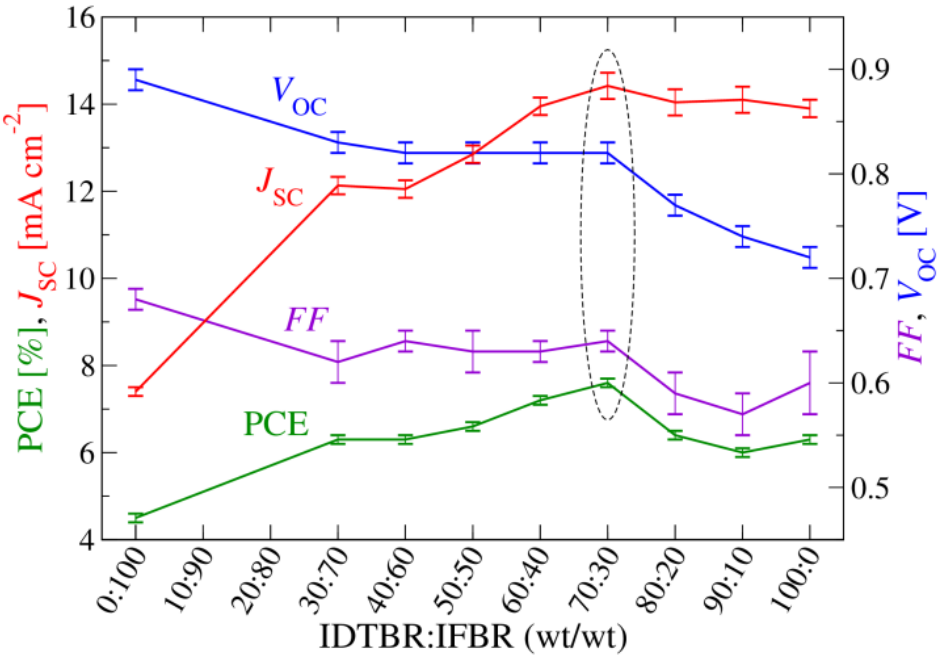

Figure 5.3 Performance of OSCs employing P3HT:IDTBR:IFBR ternary blends with varying weight ratios of the rhodanine acceptors (1 : *x* : 1-*x*). Note the highest performing blend ratio of 70:30 IDTBR:IFBR. (Measurements performed by Derya Baran, Iain McCulloch and coworkers; manuscript in preparation.)

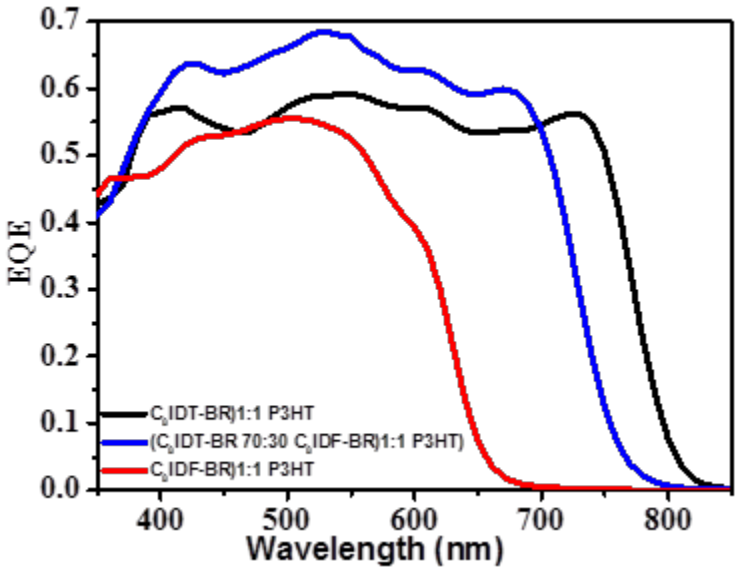

Figure 5.4 External quantum efficiency of OSCs employing P3HT:IDTBR, P3HT:IFBR, and P3HT:IDTBR(70):IFBR(30) wt/wt. (Measurements performed by Derya Baran, Iain McCulloch and coworkers; manuscript in preparation.)

Here, we aim to elucidate the molecular-scale mechanisms contributing to the observed evolution of J_{SC} and V_{OC} in the OSCs employing P3HT:IDTBR:IFBR ternary blends using molecular dynamics (MD) simulations and density functional theory (DFT) calculations. In addition, we also provide an explanation for the evolution of the EQE profiles (Figure 5.4) as a function of blend ratio. We investigate a variety of systems, including pristine, mixed, amorphous, and crystalline systems.

5.2 Computational Methodologies

We first develop a force field for IDTBR and IFBR, which we base off the OPLS-AA force field,[14] by performing DFT calculations of the single molecule *in vacuo* at the ωB97X-D/6-31G(d,p) level. The bond length and angle parameters were taken from the optimized geometry, while the force constants were taken directly from the stock OPLS-AA values. The parameters for dihedrals between adjacent backbone moieties were obtained by first performing constrained-geometry optimizations at varying dihedral angles between 0 and 180 degrees to obtain the intrinsic torsion profiles. Then, constant volume and temperature (NVT ensemble) simulations of the single molecule *in vacuo* were performed at finite temperatures (300-500 K) while the dihedral parameters were optimized such that the resulting dihedral distributions from the NVT simulations reproduced the intrinsic (DFT) torsion profile when approximated as a free energy.[15] The partial charges were obtained from the Electrostatic Potential (ESP) method.[16] Finally, the Lennard-Jones parameters were taken direction from the stock OPLS-AA values. As for P3HT, the force-field parameters were taken from Ref. 16.[17]

With the force fields in hand, we then studied ternary blends of P3HT:IDTBR:IFBR with varying weight ratios containing 0:100, 30:70, 50:50, 70:30, and 100:0 ratios of IDTBR:IFBR.

We sampled the molecular packing configurations in the NPT ensemble at 550 K and 298.15 K by cooling down the simulation from the melt. The configurations at room temperature were parsed to pick out neighboring pairs of molecules or chains that have backbone atoms within 4 Å of each other. The selected dimers and molecular complexes were studied via DFT-ωB97X-D/6-31G(d,p) calculations to obtain their electronic properties. In particular, the electronic couplings between the frontier MOs of the neighboring molecules were determined following the procedure of Valeev *et al*., which corrects for the case where the MOs on different molecules are non-orthogonal.[18]

In addition to studying the ternary blends in the mixed amorphous phase, we also studied the IDTBR and IFBR crystals, which have been shown to crystallize in the BHJ morphology. The crystalline systems we studied comprised of 3 x 3 x 3 super cells of the experimental unit cell. Again here, dimers from the simulated crystals were extracted to determine their electronic structure properties.

All MD simulations and DFT calculations were performed with *LAMMPS*[19] and *Gaussian 09* (Revision D.01)[20], respectively.

5.3 Results and Discussion

In our development of the force fields for simulating the IXBR systems, we have determined the torsion profiles along the molecular backbones, see Figures 5.5 and 5.6. The profile for the torsion between the ethylrhodanine (ER) and benzothiadiazole (BT) units is nearly the same for both IXBR molecules. In contrast, the profiles for the torsion between the BT and indacenodithiophene or indenofluorene (IX) units are starkly different. While IDTBR favors a

planar conformation (0° and 180°), IFBR favors a non-planar conformation at ~40° and ~140°. The propensity for distinct backbone conformations between the IXBR molecules are expected to have significant consequences on their molecular packing in the solid state, as we shall see below from our MD simulations of the various IXBR systems.

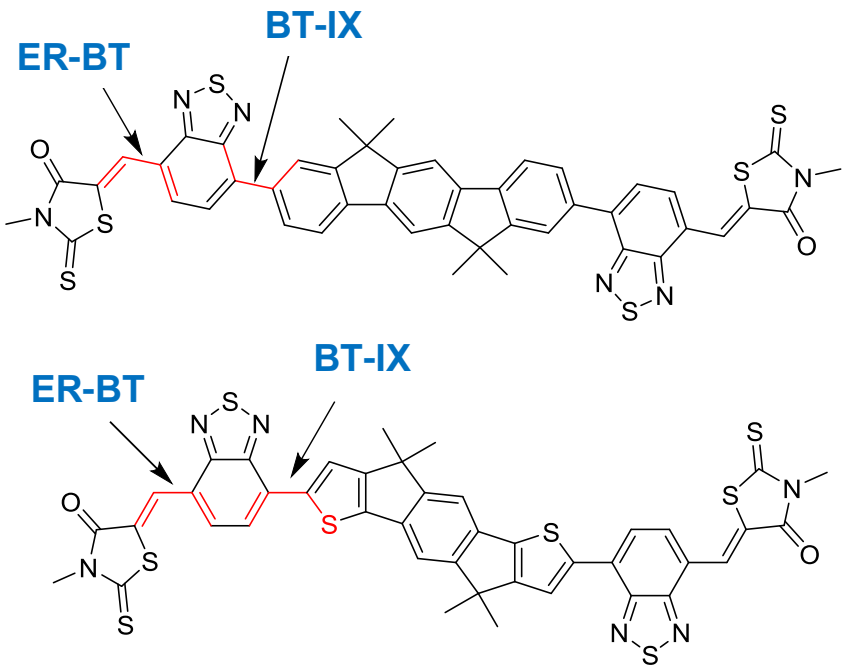

Figure 5.5 Chemical structures of the IXBR molecules with labels for the dihedrals (indicated by red bonds) along the molecular backbone. The structures shown have each dihedral in the syn conformation (0 degree).

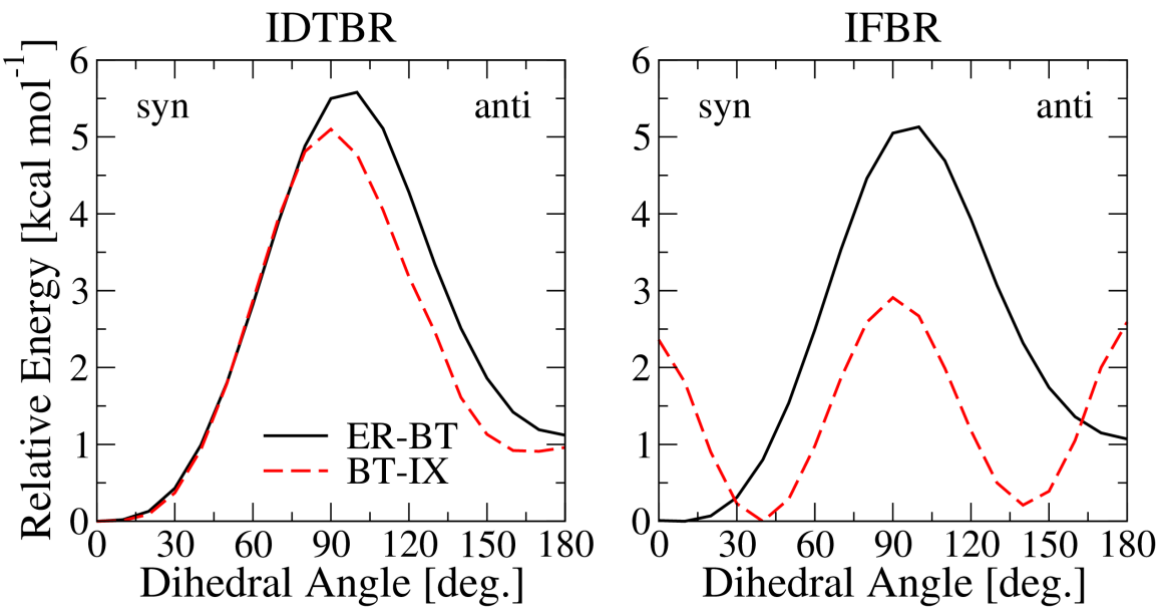

Figure 5.6 Torsion profiles between the ethylrhodanine (ER) and benzothiadiazole (BT) (solid) and BT and indacenodithiophene or indenofluorene (IX) (dashed) for IDTBR (left) and IFBR (right) determined at the ωB97X-D/6-31G(d,p) level for a single molecule in vacuum.

We performed MD simulations of a variety of amorphous systems including pristine systems of IXBR and blends of IDTBR:IFBR and P3HT:IDTBR:IFBR with varying weight ratios. In addition, we also studied the IXBR crystals. The dihedral distributions along the IXBR backbones in the solid state at the melt temperature of 550 K are shown in Figure 5.7. The distributions are nearly identical between the IXBR molecules for the ER-BT dihedral. In contrast, the distributions for the BT-IX dihedral are significantly different, as a result of the differences in the intrinsic torsion profiles (Figure 5.6). These dihedral distributions remain unchanged when either of the IXBR molecules is blended with the other or with P3HT or both. The propensity for IFBR to assume non-planar backbone conformations is expected to increase the intermolecular distances between neighboring molecules. When blended with IDTBR or P3HT (or both), we expect the BT units of IFBR to protrude out of the backbone plane and

possibly induce disorder onto the neighboring chain. Our discussion below will aim to address these predictions.

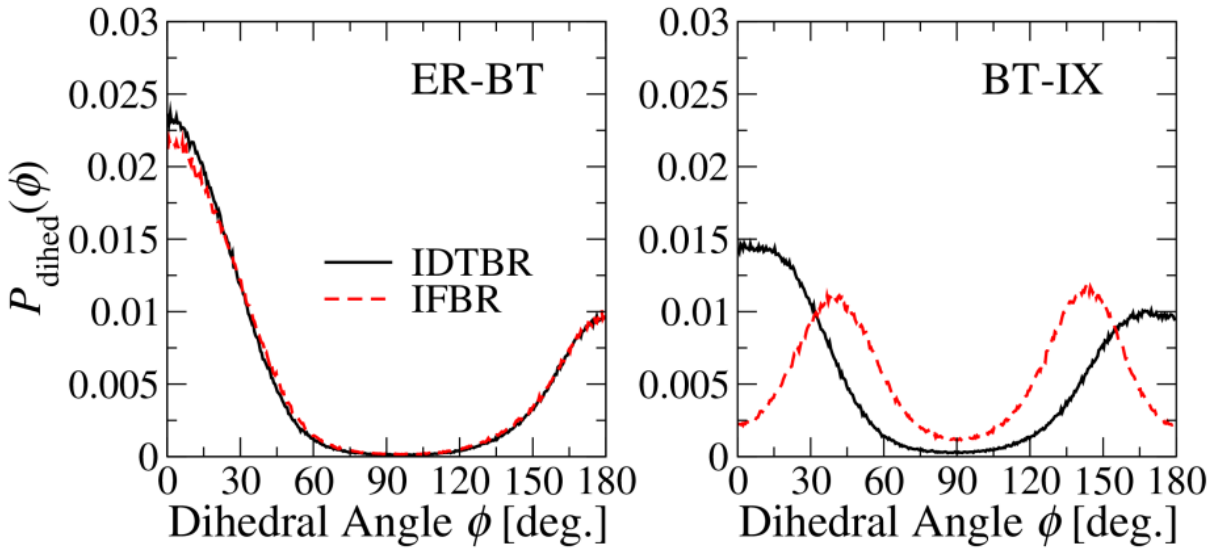

Figure 5.7 Dihedral distributions between ER-BT (left) and BT-IX (right) for the pristine systems of IDTBR (solid) and IFBR (dashed) determined from constant NPT simulations at 550 K.

From the resulting molecular configurations in the solid state at room temperature, we evaluated the electronic structure properties using DFT calculations at the ωB97X-D/6-31G(d,p) level. Since the V_{OC} has been shown to correlate with the LUMO energy level of the acceptor given the same donor component,[21] we will first examine the distribution of those energy levels for IDTBR and IFBR in the various systems, see Figure 5.8. Note for our discussion that changes in HOMO and LUMO levels (or IPs and EAs) on the order of 1 meV translate empirically to V_{OC} changes on the order of 1 mV.[21]

We first look at IDTBR, which has an average LUMO level that is slightly higher in the crystal than in the pristine amorphous phase (Figure 5.8a). We attribute this result to the fact that, in the crystal, the BT-IX dihedral assumes the anti (180°) conformation (Figure 5.6), which is slightly higher in energy relative to the syn conformation and contributes to destabilizing the LUMO. On the other hand, the IDTBR molecules can assume a distribution of syn and anti conformations in the amorphous phase. Moving on, upon blending with IFBR, P3HT, or both, the IDTBR LUMOs are further destabilized in that order. Since both IFBR and P3HT have intrinsic torsion profiles that favor non-planarity, we believe the destabilization of the IDTBR LUMOs is a consequence of the protrusive effects of the backbone units of IFBR (BT units) and P3HT (thiophene units). Between IFBR and P3HT, it appears that P3HT acts to destabilize the IDTBR LUMOs slightly more than IFBR does (Figure 5.8a).

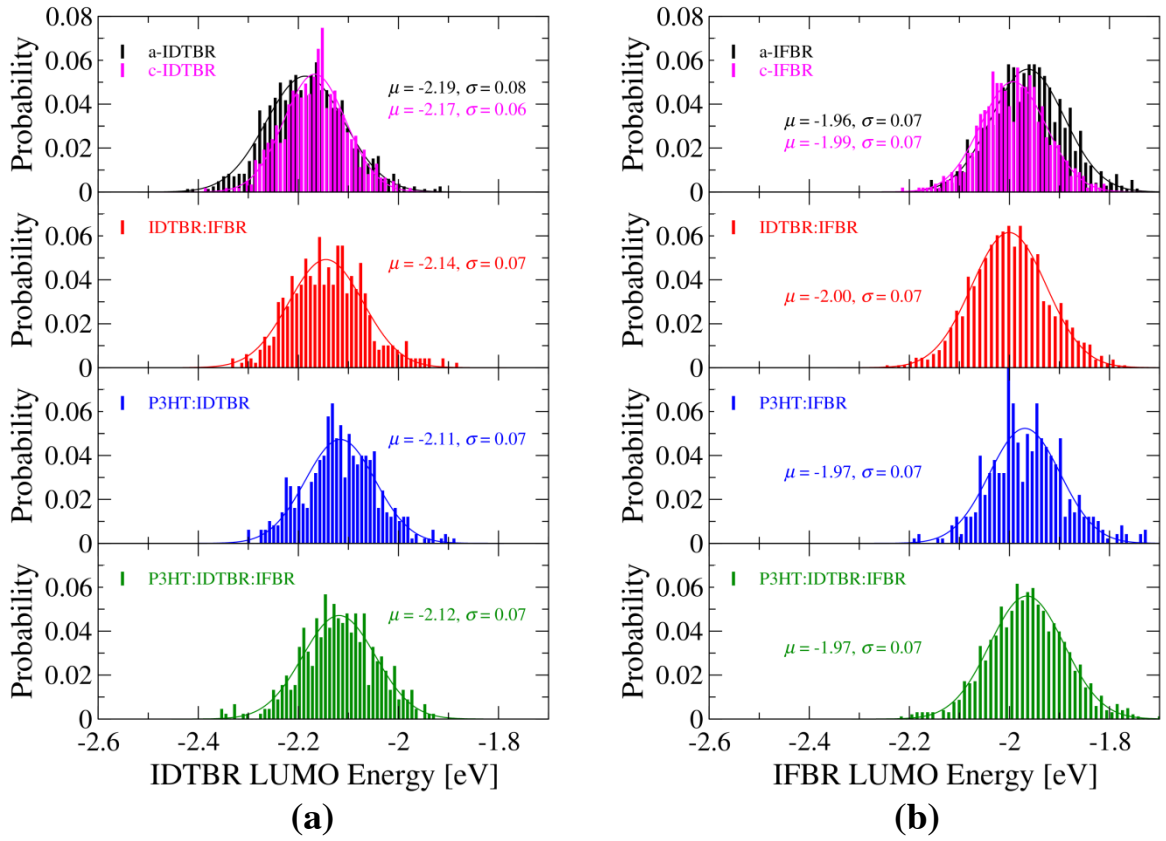

Figure 5.8 Distributions of the LUMO energy levels of (a) IDTBR and (b) IFBR molecules in the various types of systems (from top to bottom): pristine amorphous (black) and crystalline (magenta), 30:70 IDTBR:IFBR (red), 100:100 P3HT:IDTBR or P3HT:IFBR (blue), and 100:30:70 P3HT:IDTBR:IFBR (green). The mean is μ and the standard deviation is σ (in eV).

Turning to IFBR (Figure 5.8b), the average LUMO level is slightly higher in the pristine amorphous phase than in the crystal. We attribute this result to the fact that, in the crystal, the IFBR molecules pack more orderly, thereby minimizing the protrusive effects of neighboring BT units, which results in less backbone distortion and stabilizes the IFBR LUMOs. When blended with IDTBR, the average LUMO of IFBR is stabilized by ~40 meV, which further supports the hypothesis that the protrusion of the BT units of IFBR destabilizes the LUMOs of neighboring molecules regardless of their identity. In IDTBR:IFBR blends (where the total number of molecules is the same as in the pristine IDTBR or IFBR systems), the probability that a molecule

will have an IFBR molecule as its neighbor is decreased. When the concentration of IFBR is reduced by the addition of IDTBR, which has a non-protruding BT unit owing to the higher propensity for planarity, the average distortion felt by the IFBR molecules is also reduced. We will attempt to characterize the degree of backbone distortion later in the discussion.

The LUMO level distributions shown in Figure 5.8 are for the IDTBR:IFBR blend with 30:70 weight ratio and P3HT:IDTBR:IFBR blend with 100:30:70 weight ratio. The results for other blend ratios are shown in Tables 5.1 and 5.2, respectively. The first trend to observe is that in IDTBR:IFBR blends, the largest changes (~40 meV) occur when adding 30% of either component (Table 5.1). The evolution in the intermediate range between 70:30 and 30:70 IDTBR:IFBR is roughly flat (~10 meV variations). The smaller variation is also observed for P3HT:IDTBR:IFBR ternary blends throughout the entire range of blend ratios (Table 5.2). The trends observed for the IDTBR:IFBR blends follow the evolution of the V_{OC} (Figure 5.3) for the P3HT:IDTBR:IFBR ternary solar cells, that is the largest changes for the V_{OC} occur when 30% of either IDTBR or IFBR is added to the respective binary blend. In the intermediate range, the evolution of the V_{OC} is essentially flat. These results suggest that the mixed IDTBR:IFBR phases play an important role in affecting the V_{OC} of the P3HT:IDTBR:IFBR ternary devices as a consequence of the evolution of the LUMO levels in those mixed phases. The results here are also consistent with the alloying model of Thompson and coworkers,[6] which demonstrates that the V_{OC} is tunable when the two acceptors are sufficiently well mixed.

Table 5.1 Average LUMO energy levels for IDTBR and IFBR molecules in IDTBR:IFBR binary systems with varying blend ratios. All values are in eV; standard deviations are 0.07 eV.

Blend ratio (wt/wt)	IDTBR	IFBR
100:0	-2.19	--
70:30	-2.15	-2.00
50:50	-2.14	-1.99
30:70	-2.14	-2.00
0:100	--	-1.96

Table 5.2 Average LUMO energy levels for IDTBR and IFBR molecules in P3HT:IDTBR:IFBR ternary systems with varying blend ratios. All values are in eV; standard deviations are 0.07 eV.

Blend ratio (wt/wt)	IDTBR	IFBR
100:100:0	-2.12	--
100:70:30	-2.13	-1.98
100:50:50	-2.12	-1.97
100:30:70	-2.12	-1.97
100:0:100	--	-1.97

Next, we examine the HOMO-LUMO (H-L) energy gaps for the IDTBR:IFBR blends (Table 5.3) and P3HT:IDTBR:IFBR blends (Table 5.4), where the evolutions are in line with the results from the LUMO level distributions above. The largest changes (~100-110 meV) from average values of the H-L gaps of IDTBR and IFBR occur when 30% of the other component is added (Table 5.3). A comparatively smaller evolution (~10-20 meV changes) occurs in the intermediate range. Once again, these trends are not observed for the P3HT:IDTBR:IFBR ternary blends (Table 5.4). The distributions for the 30:70 IDTBR:IFBR blends are shown in Figure 5.9 for

example. While the average H-L gap for IFBR (Figure 5.9b) is approximately the same in both the amorphous phase and the crystal, a large difference (~130 meV) exists in the case of IDTBR (Figure 5.9a).

Table 5.3 Average HOMO-LUMO energy gaps for IDTBR and IFBR molecules in IDTBR:IFBR binary systems with varying blend ratios. All values are in eV; standard deviations are 0.10 eV.

Blend ratio (wt/wt)	IDTBR	IFBR
100:0	4.06	--
70:30	4.15	4.57
50:50	4.14	4.58
30:70	4.16	4.56
0:100	--	4.66

Table 5.4 Average HOMO-LUMO energy gaps for IDTBR and IFBR molecules in P3HT:IDTBR:IFBR ternary systems with varying blend ratios. All values are in eV; standard deviations are 0.10 eV.

Blend ratio (wt/wt)	IDTBR	IFBR
100:100:0	4.24	--
100:70:30	4.22	4.65
100:50:50	4.23	4.65
100:30:70	4.23	4.66
100:0:100	--	4.66

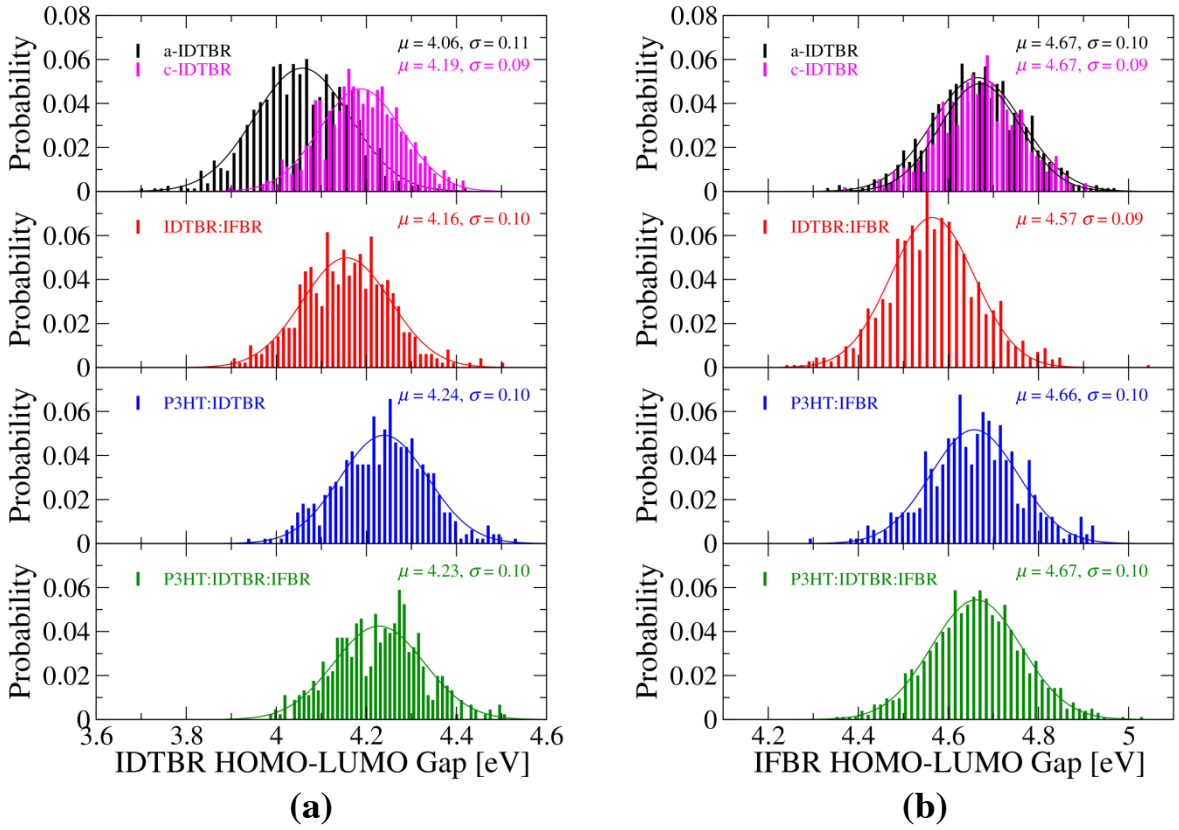

Figure 5.9 Distributions of the LUMO energy levels of IDTBR (left) and IFBR (right) molecules in the various types of systems (from top to bottom): pristine amorphous (black) and crystalline (magenta), 50:50 IDTBR:IFBR (red), 50:50 P3HT:IDTBR or P3HT:IFBR (blue), and 100:50:50 P3HT:IDTBR:IFBR (green). The mean is μ and the standard deviation is σ.

The results here for the IFBR H-L gaps can partly explain the evolution of the J_{SC} in the ternary solar cells (Figure 5.3), where the largest enhancement occurs when 30% IDTBR is added to the P3HT:IFBR binary blend. The initial addition of 30% IDTBR into the system produces IDTBR:IFBR mixed phases, which leads to the most dramatic changes in the IFBR H-L gap (narrowing by ~100 meV, see Table 5.3) with no further significant changes for higher IDTBR concentrations. The qualitative agreement between the evolution of the J_{SC} and IFBR H-L gap suggests that the narrower IFBR H-L gap translates to a smaller E_{opt} and in turn to greater absorption and charge-carrier generation. The further increase in the J_{SC} beyond the 30:70

IDTBR:IFBR ratio (Figure 5.3) is likely due to the greater absorption and charge-carrier generation from the increasing concentration of IDTBR; recall that the IFBR H-L gap does change much beyond this point.

On the other hand, the results for the IDTBR H-L gaps can partly explain the evolution of the EQE profiles (Figure 5.4). The addition of 30% IFBR into the P3HT:IDTBR binary blend shifts the onset of the EQE profile to ~810 nm to ~770 nm, which is equivalent to ~0.08 eV. This shift appears to be a direct consequence of the destabilization of the IDTBR LUMO leading to a wider H-L gap upon the addition of IFBR. Additionally, the EQE in the 400-700 nm range is enhanced relative to the both reference binary blends, which points to the synergistic enhancement in absorption through blending the IXBR molecules.

In summary, we note that the IDTBR:IFBR mixed phases appear to play an important role in determining the evolution of the V_{OC}, J_{SC}, and EQE profiles as a function of blend ratio. The most dramatic changes occur upon addition of 30% of either component into the reference binary blends. In the discussion above, we have focused on clarifying the evolution of the J_{SC} in terms of changes in absorption. In the next section, we will examine the electron-transport properties of the IXBR systems in the crystals and mixed amorphous phases.

We first examine the electronic couplings for electrons (LUMO-LUMO couplings between neighboring molecules) in the IXBR crystals, the structures of which are shown in Figure 5.10 along with labels (I-V) for the various unique dimers. The corresponding electronic coupling distributions for these dimers at room temperature (298.15 K) are shown in Figure 5.11. The coupling distributions for IDTBR (Figure 5.11a) have mean absolute values between 30-55 meV while those for IFBR (Figure 5.11b) are between 10-13 meV. Distribution V for IFBR

appears to be bimodal where the higher distribution has a mean absolute value of ~77 meV but a large standard deviation of ~32 meV. Given that the electron mobility is expected to be hindered by the slowest-rate hopping step, the results here indicate that the charge-transport along π-stacks in IDTBR crystals is more efficient than in IFBR crystals. The poorer electron mobility for IFBR crystals would contribute negatively to the J_{SC}.

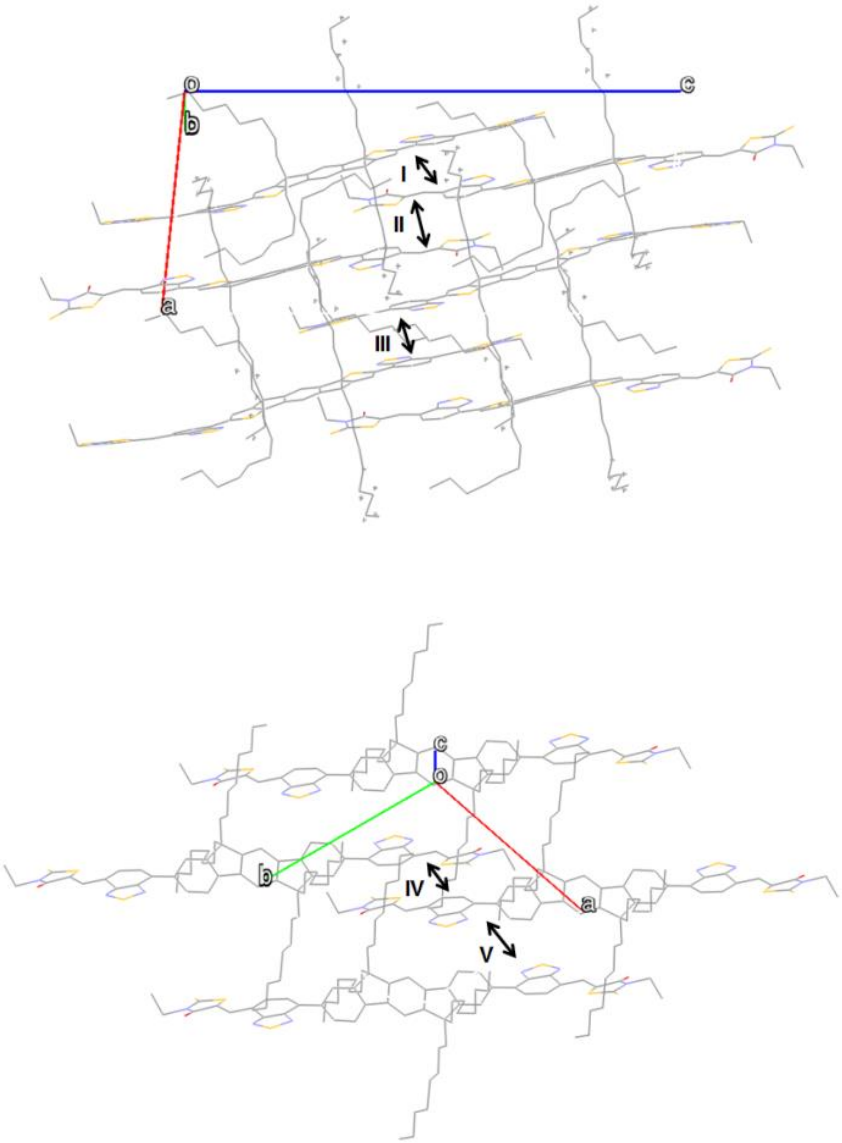

Figure 5.10 Crystal structures of IDTBR (top) and IFBR (bottom) with labels for the various unique dimers.

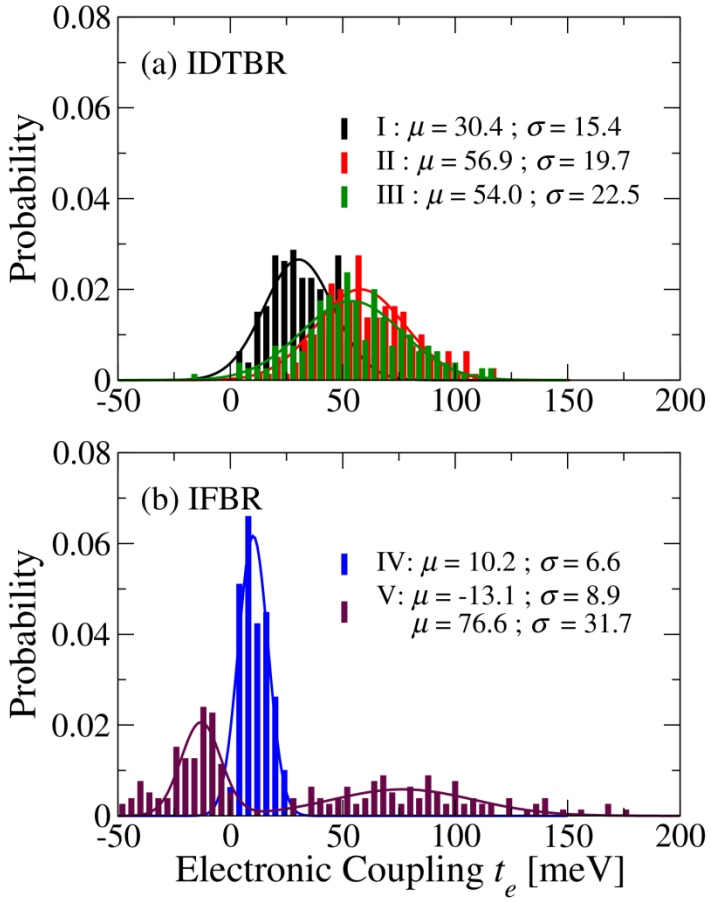

Figure 5.11 Electronic coupling distributions for electrons (LUMO-LUMO) for the various unique dimers in the (a) IDTBR and (b) IFBR crystals determined from NPT simulations at 298.15 K. The mean is μ and the standard deviation is σ.

Lastly, we examine the electronic coupling distributions for the pristine and mixed IDTBR:IFBR systems at room temperature, see Figure 5.12. There is a slight difference between the distributions for the pristine IDTBR and IFBR systems. In the mixed phases, the distributions resemble more closely the IDTBR system even when the concentration of IFBR is much higher (see 30:70 IDTBR:IFBR system). Overall, the distributions indicate similarities between the electron transport properties of the two materials in the amorphous phase and suggest that they are compatible with one another as pairing electron acceptors.

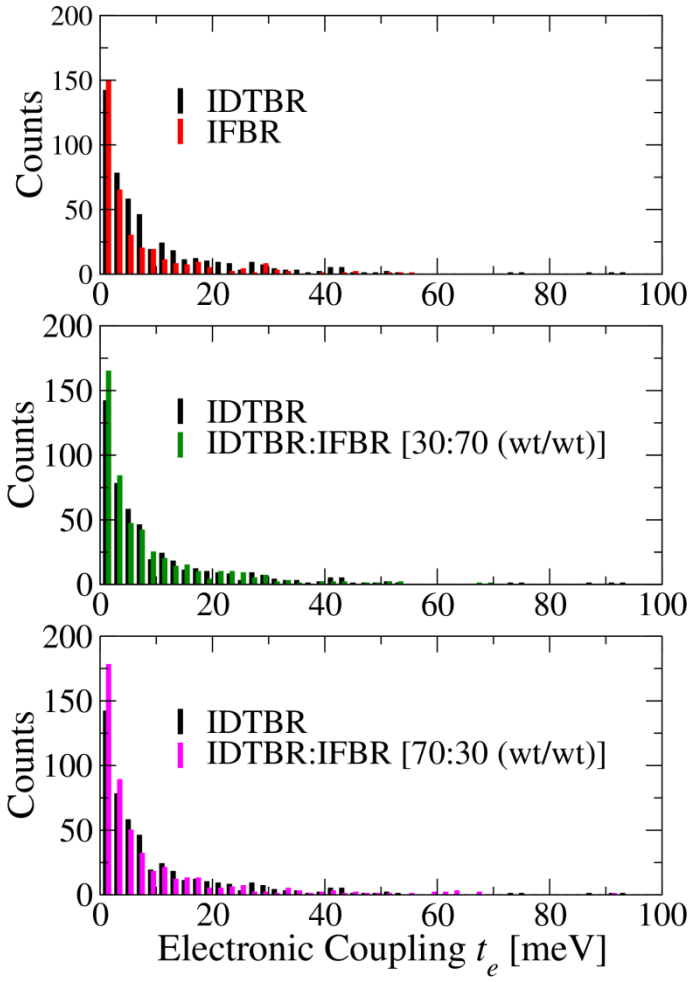

Figure 5.12 Electronic coupling distributions for electrons (LUMO-LUMO) for the dimers or molecular complexes in the pristine and mixed IXBR phases determined from NPT simulations at 298.15 K.

5.4 Conclusions

In this Chapter, we performed MD simulations and DFT calculations to study the structural and electronic properties of the IXBR molecules in a variety of pristine and mixed systems. We have related the evolution of the electronic properties of the IDTBR:IFBR blend to the evolution of the J_{SC}, V_{OC}, and EQE profiles of the P3HT:IDTBR:IFBR ternary blends.

The main results from our work are as follows:

(i) The quantum-chemical calculations of the torsion profiles along the molecular backbones point to a clear propensity for backbone planarity in IDTBR and lower extents of backbone planarity in IFBR, both of which persist in the solid state as revealed by the dihedral distributions from molecular dynamics simulations.

(ii) The evolutions of the average LUMO levels [HOMO-LUMO gaps] for IDTBR and IFBR in the IDTBR:IFBR binary blends suggest that the mixed phases play an important role in determining the evolution of the V_{OC} [J_{SC} and EQE profiles] in the ternary solar cells.

(iii) The origin of the evolution of the electronic properties of IXBR in the IDTBR:IFBR mixed phases appears to stem from the competing effects between the protruding nature of the benzothiadiazole (BT) unit of IFBR and the co-planar nature of the BT unit with its neighbors unit in IDTBR.

(iv) The electronic couplings for electron transport are generally higher in the IDTBR than IFBR crystals. The distributions for the mixed IDTBR:IFBR systems resemble more to the pristine IDTBR system than IFBR system, even when the IFBR concentration is the majority.

5.5 References

(1) Khlyabich, P. P.; Burkhart, B.; Thompson, B. C. *J*. *Am*. *Chem*. *Soc*. **2011**, *133* (37), 14534.
(2) Kotlarski, J. D.; Blom, P. W. M. *Appl*. *Phys*. *Lett*. **2011**, *98* (5), 053301.
(3) Scharber, M. C.; Mühlbacher, D.; Koppe, M.; Denk, P.; Waldauf, C.; Heeger, A. J.; Brabec, C. J. *Adv*. *Mater*. **2006**, *18* (6), 789.
(4) Ameri, T.; Khoram, P.; Min, J.; Brabec, C. J. *Adv*. *Mater*. **2013**, *25* (31), 4245.
(5) Chen, Y.-C.; Hsu, C.-Y.; Lin, R. Y.-Y.; Ho, K.-C.; Lin, J. T. *ChemSusChem* **2013**, *6* (1), 20.
(6) Khlyabich, P. P.; Rudenko, A. E.; Thompson, B. C.; Loo, Y.-L. *Adv*. *Funct*. *Mater*. **2015**, *25* (34), 5557.
(7) Khlyabich, P. P.; Burkhart, B.; Thompson, B. C. *J*. *Am*. *Chem*. *Soc*. **2012**, *134* (22), 9074.
(8) Campoy-Quiles, M.; Ferenczi, T.; Agostinelli, T.; Etchegoin, P. G.; Kim, Y.; Anthopoulos, T. D.; Stavrinou, P. N.; Bradley, D. D. C.; Nelson, J. *Nat*. *Mater*. **2008**, *7* (2), 158.
(9) Lu, L.; Xu, T.; Chen, W.; Landry, E. S.; Yu, L. *Nat*. *Photonics* **2014**, *8* (9), 716.
(10) Ameri, T.; Heumüller, T.; Min, J.; Li, N.; Matt, G.; Scherf, U.; Brabec, C. J. *Energy Environ*. *Sci*. **2013**, *6* (6), 1796.
(11) Cheng, P.; Li, Y.; Zhan, X. *Energy Environ*. *Sci*. **2014**, *7* (6), 2005.
(12) Groves, C. *Energy Environ*. *Sci*. **2013**, *6* (5), 1546.
(13) Holliday, S.; Ashraf, R. S.; Nielsen, C. B.; Kirkus, M.; Röhr, J. A.; Tan, C.-H.; Collado-Fregoso, E.; Knall, A.-C.; Durrant, J. R.; Nelson, J.; McCulloch, I. *J*. *Am*. *Chem*. *Soc*. **2015**, *137* (2), 898.
(14) Jorgensen, W. L.; Maxwell, D. S.; Tirado-Rives, J. *J*. *Am*. *Chem*. *Soc*. **1996**, *118* (45), 11225.
(15) Huang, D. M.; Faller, R.; Do, K.; Moulé, A. J. *J*. *Chem*. *Theory Comput*. **2010**, *6* (2), 526.
(16) Singh, U. C.; Kollman, P. A. *J*. *Comput*. *Chem*. **1984**, *5* (2), 129.
(17) Schwarz, K. N.; Kee, T. W.; Huang, D. M. *Nanoscale* **2013**, *5* (5), 2017.
(18) Valeev, E. F.; Coropceanu, V.; da Silva Filho, D. A.; Salman, S.; Brédas, J.-L. *J*. *Am*. *Chem*. *Soc*. **2006**, *128* (30), 9882.
(19) Plimpton, S. *J*. *Comput*. *Phys*. **1995**, *117* (1), 1.
(20) Frisch, M. J.; Trucks, G. W.; Schlegel, H. B.; Scuseria, G. E.; Robb, M. A.; Cheeseman, J. R.; Scalmani, G.; Barone, V.; Mennucci, B.; Petersson, G. A.; Nakatsuji, H.; Caricato, M.; Li, X.; Hratchian, H. P.; Izmaylov, A. F.; Bloino, J.; Zheng, G.; Sonnenberg, J. L.; Hada, M.; Ehara, M.; Toyota, K.; Fukuda, R.; Hasegawa, J.; Ishida, M.; Nakajima, T.; Honda, Y.; Kitao, O.; Nakai, H.; Vreven, T.; Montgomery Jr., J. A.; Peralta, J. E.; Ogliaro, F.; Bearpark, M. J.; Heyd, J.; Brothers, E. N.; Kudin, K. N.; Staroverov, V. N.; Kobayashi, R.; Normand, J.; Raghavachari, K.; Rendell, A. P.; Burant, J. C.; Iyengar, S. S.; Tomasi, J.; Cossi, M.; Rega, N.; Millam, N. J.; Klene, M.; Knox, J. E.; Cross, J. B.; Bakken, V.; Adamo, C.; Jaramillo, J.; Gomperts, R.; Stratmann, R. E.; Yazyev, O.; Austin, A. J.; Cammi, R.; Pomelli, C.; Ochterski, J. W.; Martin, R. L.; Morokuma, K.; Zakrzewski, V. G.; Voth, G. A.; Salvador, P.; Dannenberg, J. J.; Dapprich, S.; Daniels, A. D.; Farkas, Ö.; Foresman, J. B.; Ortiz, J. V.; Cioslowski, J.; Fox, D. J. *Gaussian 09*; Gaussian, Inc.: Wallingford, CT, USA, 2009.
(21) Scharber, M. C.; Sariciftci, N. S. *Prog*. *Polym*. *Sci*. **2013**, *38* (12), 1929.

Chapter 6

Effect of Fluorine Substitutions on the Structural and Electronic Properties of 5,11-Bis(triethyl silylethynyl) Anthradithiophene Crystals

6.1 Introduction

In Chapters 3-5, we focused on systems that are of interest to bulk-heterojunction (BHJ) organic solar cells (OSCs). In this Chapter, we shift our attention to molecular crystals of π-conjugated small molecules that are used as the hole-transport material in organic field-effect transistors (OFETs). While the systems studied here are specific to OFETs, the results are general in that they demonstrate how quantum-chemical calculations and MD simulations can be used to evaluate the structural and electronic properties of the crystal, which for certain blend materials, have been observed to crystallize in the BHJ morphology of OSCs.

OFETs based on solution-processable π-conjugated semiconductors have become increasingly attractive to serve as the backplane component in flexible electronic devices such as sensors, organic light-emitting diodes (OLEDs), and radio frequency identification (RFID) tags.[1,2] However, for OFETs to become competitive with their inorganic counterparts (oxide and polycrystalline silicon thin-film transistors), greater improvements in their device performance, materials stability, and high-throughput processability must be achieved.[1] In particular, OFETs employing acene-based small molecules that are easy to synthesize and whose solubility and molecular electronic properties are amenable to systematic tailoring have shown promising potential to satisfy the above requirements.[2,3] For example, facile chemical substitution of the acene backbone with electron-withdrawing groups has allowed for improvements in thermal and oxidative stability.[4]

With that context in mind, we focus here on molecular materials derived from 5,11-bis(triethyl silylethynyl) anthradithiophene (TESADT) and its 2,8-difluorinated analog diF-TESADT (Figure 6.1), which have achieved relatively high hole mobilities (close to or >1 cm^2

V^{-1} s^{-1}) in OFETs using simple fabrication techniques at room or moderately elevated temperatures.[5–8] Reproducible mobilities (μ_{avg} = 0.42 ± 0.19 cm^2 V^{-1} s^{-1} over 90 transistors)[9] have been achieved with TESADT active layers deposited through single-step spin casting at temperatures well below the material glass transition temperature. Notably, OFETs using diF-TESADT showed slightly better performance (μ_{avg} = 0.70 ± 0.15 cm^2/V-s over 50 transistors)[6] than TESADT in device configurations where the Au source and drain contacts were treated with pentafluorobenzene thiol before spin casting; the high performance was attributed to the rapid, preferential nucleation of the crystallite originating from the contacts and extending into the conduction channel, with a dominant fraction of crystallites having the π-stacking direction parallel to the substrate.[6,10] More recently, mobilities as high as 6.7 cm^2 V^{-1} s^{-1} have been achieved for diF-TESADT when blended with polystyrene and processed via blade coating[11] – a result which is on par with single-crystal devices.[12]

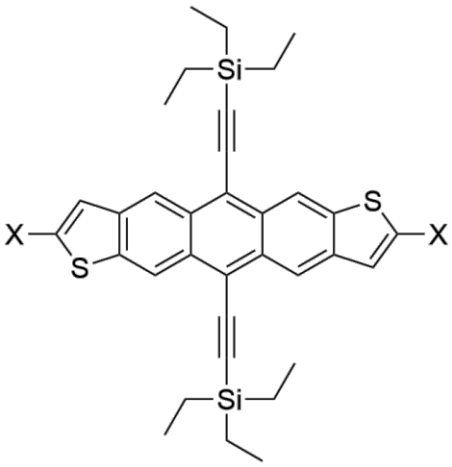

Figure 6.1 Chemical structure of 5,11-bis(triethyl silylethynyl) anthradithiophene (TESADT) (*X* = H) and its 2,8-difluorinated analog diF-TESADT (*X* = F).

Several studies – making use of a number of scattering and microscope techniques, including scanning microbeam grazing incidence wide-angle X-ray scattering (μGIWAXS),[13] scanning Kelvin probe microscopy (SKPM),[14] atomic force microscopy (AFM), and transmission electron microscopy (TEM)[10] – have sought to correlate the OFET performance with the thin-film microstructure of diF-TESADT. Three polymorphs have been identified as a function of channel length[14]:

- In short channels (≈5 μm), a single-crystal polymorph exists in which the π-stacking (001) plane favorably extends across the full length of the channel, and charge-carrier transport is mainly hindered by injection.
- In medium-length channels (≈20-50 μm), the polymorph includes grain boundaries in the middle of the channel where the two preferentially oriented [001] crystallites meet from the source/drain electrodes; transport is hindered both by injection and grain boundaries.
- In long channels (≈80-100 μm), unfavorably [111] oriented crystallites dominate the polymorph as the mid-section of the channel is too far away (≈25 μm) from the source/drain electrodes for the preferential nucleation to persist; transport is limited from the small and poorly ordered grains that form on the silicon dioxide substrate.

Given the importance of the extent of crystallization in the conduction channel on the mobility of these materials, we are motivated here to examine the structural and charge-transport properties of their crystal structures. We use a combination of computational methodologies to compare the intrinsic charge-transport properties of the TESADT and diF-TESADT crystals and evaluate the effect of partial fluorination of these molecular crystals, which to the best of our knowledge has not been reported before. Using density functional theory (DFT) calculations, we examine side-by-side the reorganization energies, band structures, effective masses, and electronic couplings

between neighboring molecules. Through molecular dynamics (MD) simulations, we provide a dynamic picture of the electronic couplings. In addition, we perform molecular mechanics (MM) calculations to compare the intrinsic growth morphologies of the crystals.

6.2 Computational Methodologies

We note that the preparations of TESADT and diF-TESADT have originally yielded an inseparable mixture of syn- and anti-isomers where the terminal thiophenes are aligned parallel or anti-parallel, respectively.[5,6] Later, Lehnherr et al. reported the synthesis of isomerically pure syn-anthradithiophenes[15] and found that single-crystal OFETs of the pure syn-isomer gave comparable performance to those of the mixed isomers. For the sake of simplicity, we focus only on the anti-isomers of the anthradithiophenes in our theoretical investigation.

Geometry optimizations and single-point energy calculations of the isolated TESADT and diF-TESADT molecules in the neutral, radical-cation, and radical-anion states were performed via density functional theory (DFT)[16] at the B3LYP/6-31G(d,p) level.[17,18] Intermolecular electronic couplings (transfer integrals) were evaluated through the fragment orbital approach[19–21] for dimers extracted (i) directly from the crystal structures and (ii) from molecular dynamics (MD) simulations of the crystal structures. The MD simulations were performed to sample the configuration space at room temperature (RT) and to generate a set of dynamic configurations of nearest-neighbor molecular dimers from which distributions of the electronic couplings may be obtained. For the MD simulations, triclinic super cells consisting of 8 × 7 × 4 and 7 × 7 × 4 ($n_a \times n_b \times n_c$) for TESADT and diF-TESADT, respectively, were simulated with periodic boundary conditions enforced. The OPLS-AA[22] (all-atom optimized

potentials for liquid simulations) force field was used to model the RT dynamics of the crystals, reproducing the unit-cell parameters to within ca. 5 percent error. The temperature (298 K) and pressure (1 atm) of the crystals were kept constant using a Nosé-Hoover thermostat[23] and Parrinello-Rahman barostat,[24] respectively. The cut-off radius for non-bonded interactions was 12.0 Å. The SHAKE algorithm was used to constrain C-H bonds with fixed length.[25] Electrostatic interactions were computed using the Ewald summation method.[26] The velocity-Verlet method was used for dynamic integration with a time step of 1.5 fs. Configurations were saved every 75 fs and distributions were computed using 30 ps of the simulated trajectory. Distributions of the electronic coupling, as calculated at the B3LYP/6-31G(d,p) level, were obtained by sampling all possible dimers of a given type within the crystal for all trajectory frames considered.

Electronic band structures of the TESADT and diF-TESADT crystals were evaluated using periodic DFT calculations at the B3LYP/6-21G level of theory. Pack-Monkhorst and Gilat shrinking factors of 6 and 12, respectively, were used for the generation of the *k*-point grid in reciprocal space. The effective masses were computed at the band extremes using a finite difference method as implemented in the "Effective Mass Calculator" software.[27] Cohesive energies (E_{coh}) were determined according to the equation:

$$E_{coh} = \frac{E_{bulk}}{Z} - E_{molecule} \tag{6.1}$$

where E_{bulk} is the crystal structure energy, Z is the number of molecules per unit cell, and $E_{molecule}$ is the energy of an isolated molecule in the gas phase. E_{bulk} and $E_{molecule}$ correspond to the energy of the optimized geometries; for the bulk optimizations, only the molecular parameters were relaxed, while all cell parameters remained fixed. The role of the zero-point energy (ZPE)

corrections in the cohesive energy calculation was considered by carrying out frequency calculations at the optimized geometries, but was determined to be relatively small (≈1 kcal mol^{-1}). The cohesive energies were determined with counterpoise correction to account for basis set superposition errors (BSSE),[28] and with the dispersion energy described by the semi-empirical method of Grimme.[29]

All DFT calculations on the isolated molecules and dimers were performed with the *Gaussian 09* (Revision B.01)[30] software suite while band structure calculations were performed with the *Crystal09* package. All MD simulations were performed using the *LAMMPS* software.[31]

Additionally, molecular mechanics (MM) calculations were performed to determine the effect of fluorine substitution on the intrinsic single crystal growth morphology. These calculations are based on the method of Hartman and Bennema and assumed that the growth rate of a crystal face is proportional to its attachment energy E_{att}, which is the energy per molecule released upon adsorption of a crystalline slice to the bulk crystal.[32] The calculations were performed using the COMPASS force field[33] in the Materials Studio Morphology module[34] with an accuracy setting of "fine". Electrostatic interactions were computed using the Ewald summation method.[26]

6.3 Results and Discussion

In this Section, we compare the structural and electronic properties of the molecular and crystal systems of TESADT and diF-TESADT to elucidate the effects of fluorine substitution in the parent anthradithiophene compound. We begin with a quick presentation of the molecular

electronic properties before moving to the properties of the crystals. In each case, we discuss the implications for electron and hole transport.

Molecular Properties: Electronic Structure, Redox Properties, and Reorganization Energies

The molecular electronic and redox properties of TESADT and diF-TESADT, as calculated at the B3LYP/6-31G(d,p) level, are shown in Table 6.1. The HOMOs and LUMOs of the two molecules are nearly identical (see Figure 6.2). As expected, both the HOMO and LUMO energies of TESADT are stabilized upon fluorination. The HOMO is more stabilized (by 0.16 eV) than the LUMO (0.05 eV), thereby increasing the HOMO-LUMO gap, a result which is also observed for similar functionalized acene derivatives. Accordingly, fluorination of TESADT increases both the ionization potential (IP) and electron affinity (EA) [see Table 6.1], with a larger increase for the IP (0.14 eV) than for the EA (0.06 eV). For comparison, the IP [EA] values for TESADT and diF-TESADT are larger [smaller] than those for TIPS-pentacene (IP of 5.68 eV and EA of 1.73 eV, calculations at the same level of theory), which suggests enhanced oxidative stability but reduced electron-injection efficiency for these ADT-based compounds. To the best of our knowledge, no experimental IP or EA values have been reported for TESADT and diF-TESADT. However, the trend in our calculated IP values between TIPS-pentacene and TESADT (≈0.2 eV difference) is consistent with that for pentacene versus anthradithiophene as observed experimentally[35] (≈0.1 eV difference) or obtained by theoretical calculations[36] (≈0.2 eV difference).

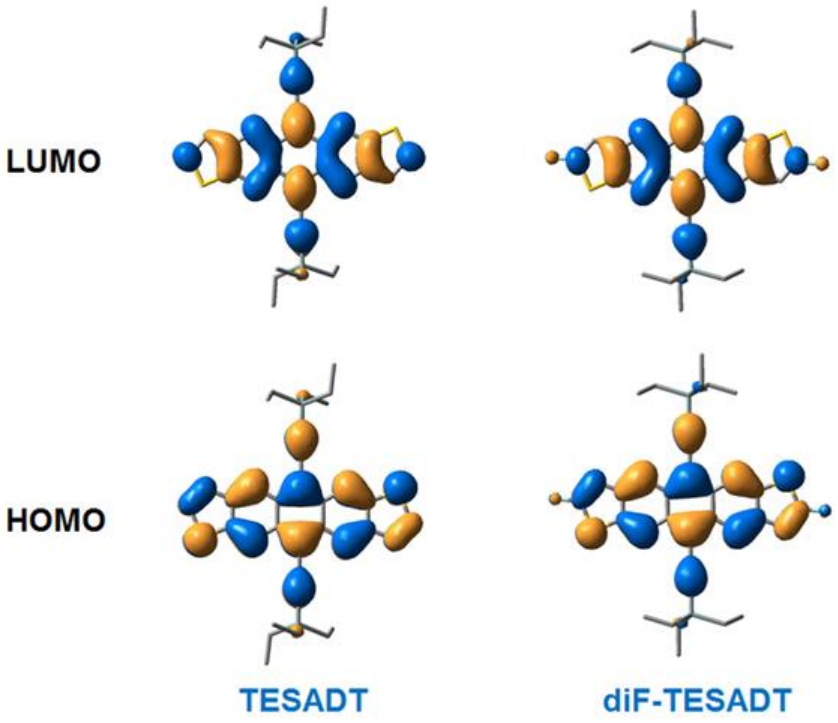

Figure 6.2 Frontier orbitals of TESADT and diF-TESADT molecules determined from DFT-B3LYP/6-31G(d,p) calculations.

Next, we examine the effect of fluorination on the intramolecular reorganization energies, which are relevant parameters in evaluating charge-carrier transport. The reorganization energy is a measure of the energetic stabilization when a molecule acquires a charge and therefore influences the rate at which localized charge carriers can hop between molecular sites; higher values indicate higher propensities for charge localization and contribute to decreasing the rate of charge transfer.[37] The intramolecular reorganization energies for both hole (λ_h) and electron (λ_e) are slightly larger for diF-TESADT than for TESADT, as shown in Table 6.1. This effect can be explained in part by the small anti-bonding π-contribution of fluorine in the HOMO and LUMO orbitals of diF-TESADT (see Figure 6.2), which are reduced [strengthened] upon oxidation [reduction]. Both compounds exhibit smaller intramolecular reorganization energies for holes

than for electrons, which is similar to previous results obtained for similar functionalized acene derivatives, or for the parent anthradithiophene compound. The λ_e value for TESADT (0.246 eV) is larger than that for TIPS-pentacene (0.203 eV), which again suggests reduced electron transfer properties, whereas the λ_h values are similar (0.149 eV and 0.144 eV, respectively).

Table 6.1 HOMO and LUMO energies, redox properties (adiabatic ionization potential IP[a] and electron affinity EA[a]), intramolecular reorganization energies (λ_e and λ_h), and polaron binding energies for hole transport (values in parentheses) for TESADT and diF-TESADT determined from B3LYP/6-31G(d,p) calculations of the isolated molecules. The reorganization energies are deduced from the adiabatic potential energy surfaces. All values are in eV.

	E_{LUMO}	E_{HOMO}	EA[a]	IP[a]	λ_e	λ_h
TESADT	-2.45	-4.80	1.30	5.88	0.246	0.149 (0.075)
diF-TESADT	-2.50	-4.96	1.36	6.02	0.267	0.175 (0.088)

Crystal Properties: Crystal Structure, Cohesive Energies, and Crystal Growth

We now turn our attention to the crystal properties of TESADT and diF-TESADT. Representative orientations of the crystal structures show modest differences between the crystal packings of the two materials, as shown in Figure 6.3. In both cases, the molecules are arranged with the acene backbones stacking principally along the *a*- and *b*-directions, with a small angle (~20°) between the Si-Si axes and the *c*-axis (Figure 6.3a and 6.3c). In both crystals, the interlayer distances in the *a*-direction are more closely spaced than those in the *b*-direction (~6.73 Å versus ~7.25 Å, respectively) [Figure 6.3]. The interlayer distances along the *a*-direction (shortest intermolecular distances between C···C, C···S, or C···F atoms) are 3.23 Å for TESADT and 3.38 Å for diF-TESADT. Along the *b*-direction, they are 6.53 Å and 6.65 Å,

respectively. Partial backbone stacking is also present along the diagonal intermediate *ab*-directions as shown in Figure 6.3e, which illustrates the crystal packing at the (001) surface. Based on the interlayer spacings discussed above and the fact that the electronic coupling falls of exponentially with distance, we expect charge-carrier transport to be most efficient between dimers A and least efficient between dimers B (Figure 6.3e). Thus, transport is expected to be most dominant in the *a*-direction between dimers A while transport in the *b*-direction is expected to occur in an alternating "zig-zag" fashion along dimers A, ABx, and ABy.

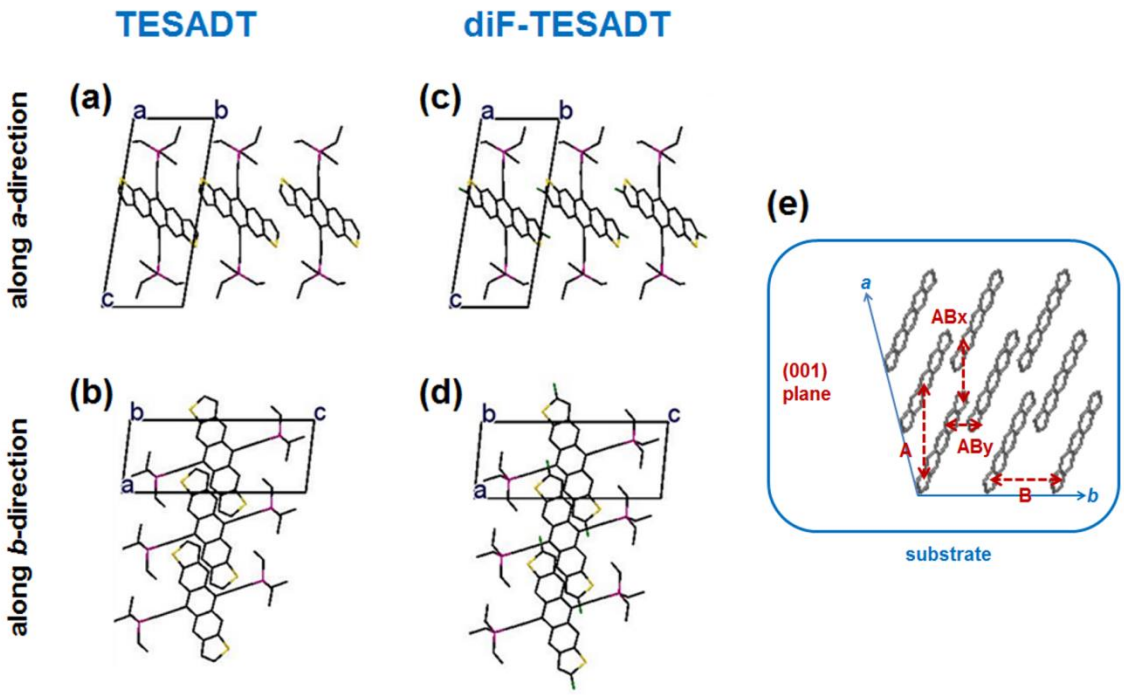

Figure 6.3 Representative orientations of the crystal structures of (a, b) TESADT and (c, d) diF-TESADT. For each material, the top panel corresponds to the view in the *a*-direction and the bottom panel corresponds to the view in the *b*-direction. (e) Top view of the (001) plane where dimer types of adjacent molecules are indicated (red arrows) along the *a*-, *b*-, and intermediate *ab*-directions. Hydrogen atoms are omitted for clarity.

The structural modifications induced by fluorination in the crystal structure of diF-TESADT lead to a small displacement between adjacent acene backbones along their long axis as compared to TESADT, see Figure 6.4. The small displacement of ≈0.4 Å corresponds to the difference in the *a*-parameters of the unit cells, which will be shown to impact key electronic properties of diF-TESADT. An analogous comparison can be made for the displacement in the *b*-direction as shown in Figure 6.3 (b, d). The difference between C-H and C-F bond-lengths is roughly 0.4 Å, which matches the center-to-center shift of ≈0.4 Å along the long axes in diF-TESADT as compared to TESADT. The driving force for this last shift might thus correspond to the tendency upon crystallization to match the appropriate C-H···F of S···F directionality of the hydrogen or halogen bonds.

The cohesive energy of the crystal structure is larger for diF-TESADT by ≈2.3 kcal mol^{-1} than for TESADT (56.4 kcal mol^{-1} vs. 54.1 kcal mol^{-1}), which suggests that additional attractive interactions (likely due to a combination of non-covalent and dispersion interactions) constitute the driving force for the observed structural modifications. Interestingly, the melting enthalpy of diF-TESADT was found to be roughly 3 kcal mol^{-1} larger than that of TESADT.

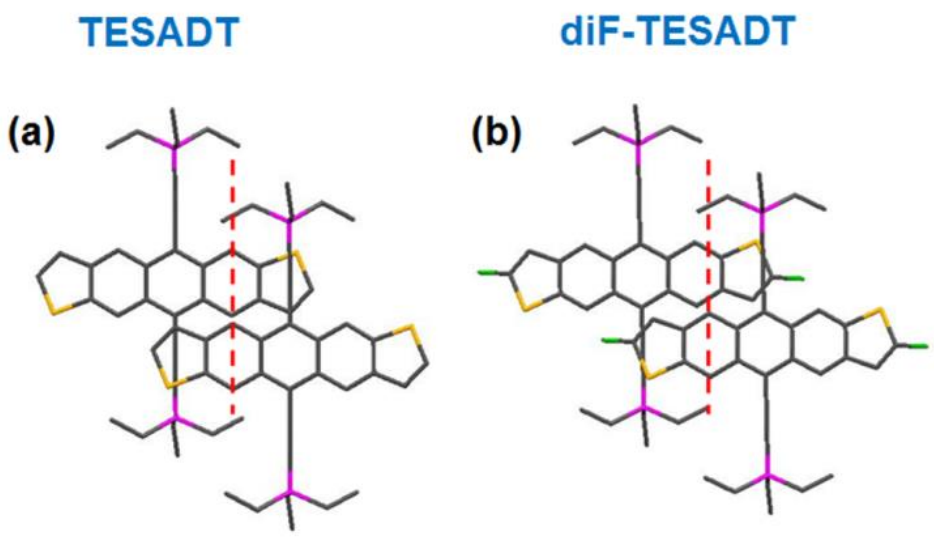

Figure 6.4 Dimer configurations from the crystal structures of (a) TESADT and (b) diF-TESADT along the *a*-direction and viewed in an intermediate *ab*-direction. Note the small displacement between adjacent ADT cores along their long axis in diF-TESADT versus TESADT as highlighted by the red dashed vertical line. Hydrogen atoms are omitted for clarity.

A final point of comparison between the TESADT and diF-TESADT crystals is their intrinsic growth morphologies, which we determine using molecular mechanics calculations following the method of Bennema.[32] Our results indicate practically the same intrinsic crystal growth morphology for both materials (see Figure 6.5), which consists of platelets with the (001) surface dominant, a feature in agreement with experiment. Thus, differences in the thin-film microstructures of the two materials are expected to stem not from intrinsic but rather from external effects such as those from the surface treatment of the substrate prior to the deposition of the organic layer. While the adsorption of pentafluorobenzene thiol on the source/drain electrodes was observed to induce strong crystallization in the transistor channel and crystal orientations that are beneficial for charge transport for diF-TESADT, no such effect was found for TESADT.[6] It has been proposed that the S···F interactions between diF-TESADT and the

pentafluorobenzene thiol lead to preferential nucleation of the crystal that favors the *ab* plane to form parallel to the substrate where charge transport is most efficient.[13] We will examine next the charge transport properties within the crystals of TESADT and diF-TESADT.

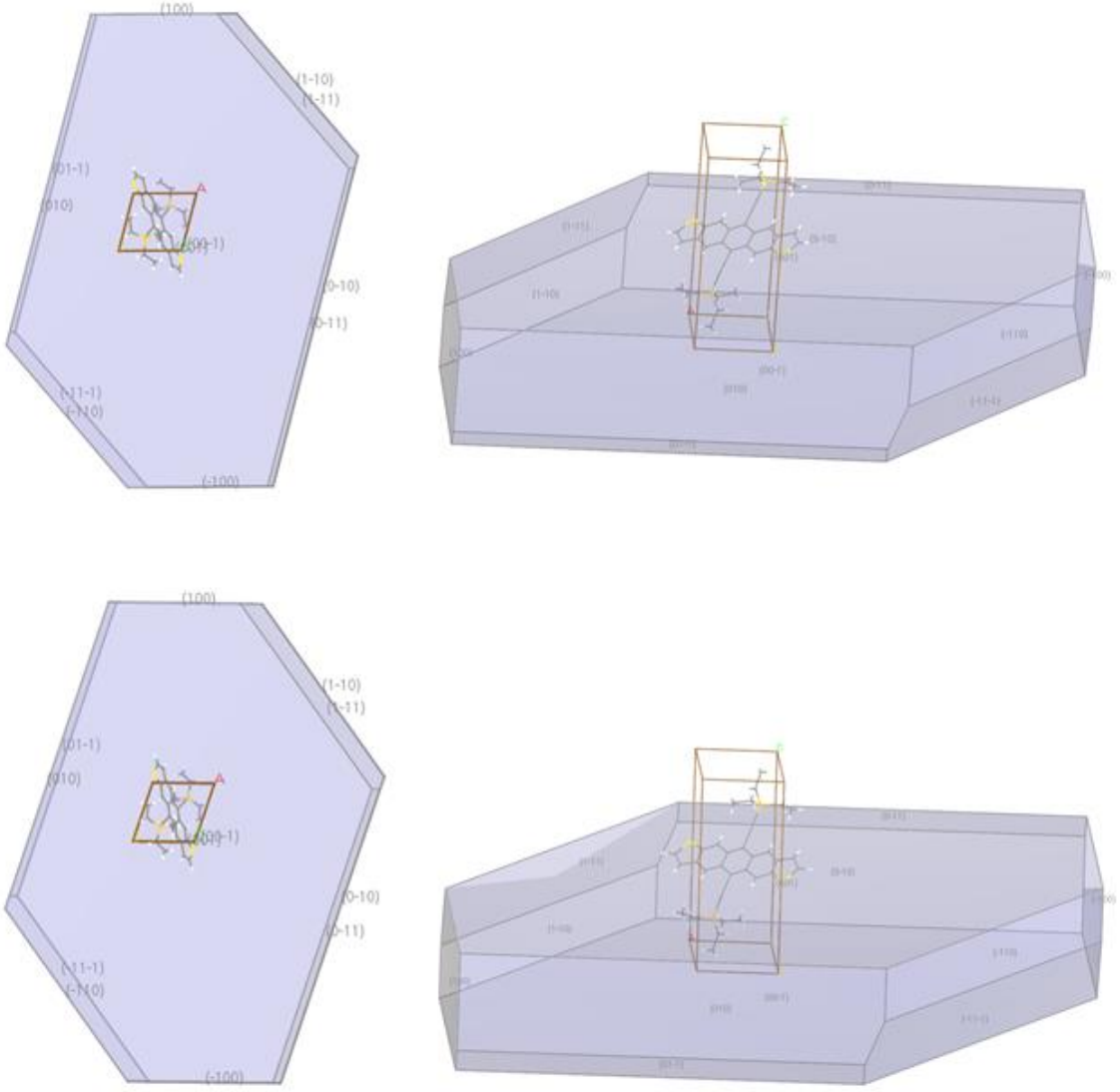

Figure 6.5 Crystal growth shapes of TESADT (top) and diF-TESADT (bottom) calculated from the Hartman and Bennema method. The two orientational views shown are chosen to highlight the platelet structure of the crystals with the <001> directions perpendicular to the surface with the largest area. These growth shapes are consistent with microscopy measurements.

Charge Transport Properties: Band Structures, Transfer Integrals, and Effective Masses

We have examined earlier the effect of fluorination on the intramolecular reorganization energy, which is a measure of the propensity for charge localization on a molecule and thus influences the rate of charge transfer between adjacent molecules. We now evaluate how the differences in the crystal packing of the two materials affect their electronic band structure and intermolecular electronic couplings (*i.e.*, transfer integrals) using both a static and dynamic picture of the packing configurations.

The band structures for TESADT and diF-TESADT reveal two-dimensional (2D) charge-carrier transport for both crystals, see Figure 6.6. The strongest dispersions of the conduction and valence bands appear along the *a*-direction (Γ-X) for both crystals, whereas substantial dispersions can be seen along the *b*-direction (Y-Γ). As for the *c*-direction (Γ-Z), there is practically no dispersion in the conduction or valence band. The band structure for TESADT shows nearly symmetric evolutions of the valence and conduction bands, the valence band being wider as compared to the conduction band (520 meV and 380 meV respectively). Transfer integrals of 130 meV and 95 meV can be deduced for hole and electron transport respectively ($1/4^{th}$ of the band widths, Table 6.2), suggesting better hole than electron transport properties for TESADT. Larger transfer integrals were also found for hole transport in diF-TESADT as compared to electron transport (135 and 43 meV, respectively), with the difference here much larger than in the TESADT case. The presence of F atoms in diF-TESADT is seen to have very marginal impact on the valence band dispersion, but results in a marked decrease in the electron transfer integral by more than 50% as compared to TESADT. Figure 6.6 clearly illustrates the quite different evolutions of the valence bands for the two compounds.

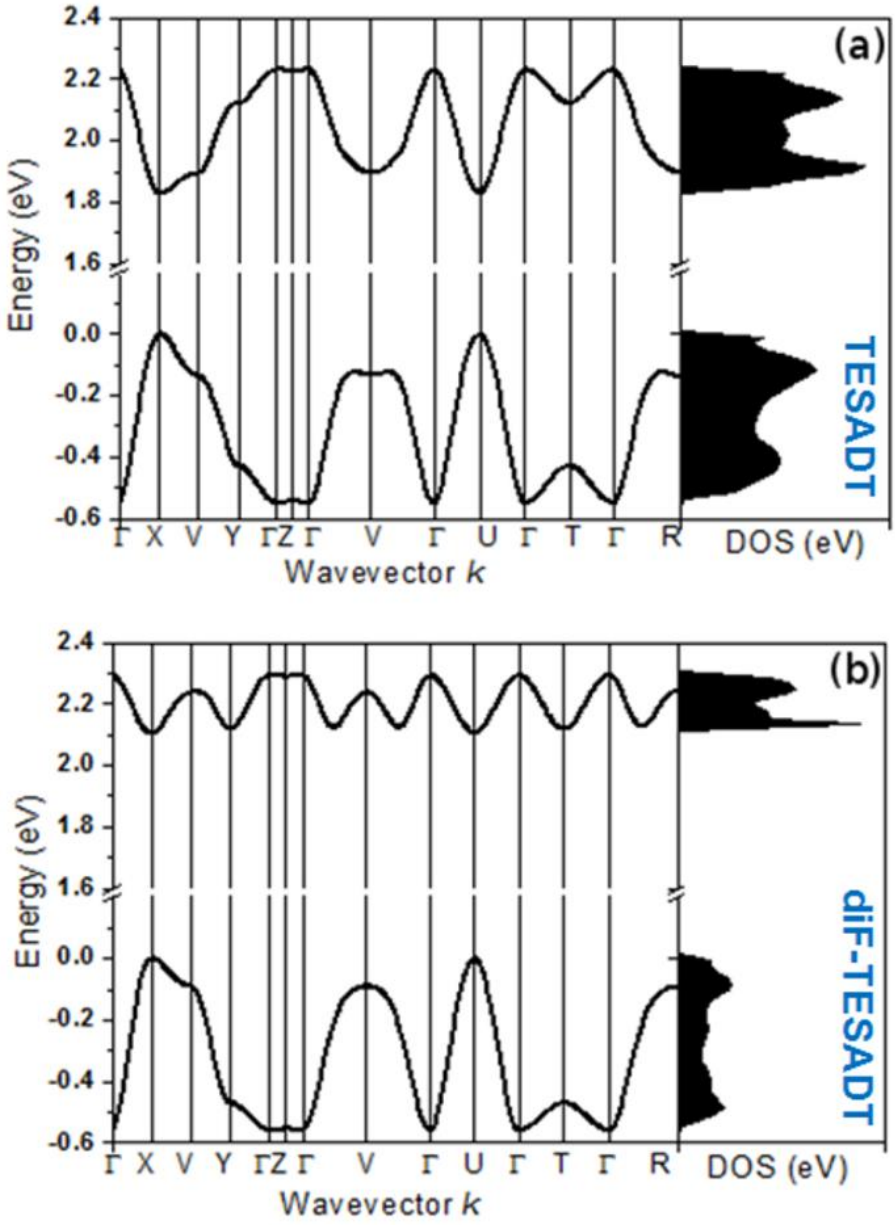

Figure 6.6 Band structures and densities of states for (a) TESADT and (b) diF-TESADT determined from B3LYP/6-21G calculations using the crystal structure geometry. The points of high symmetry in the Brillouin zone in both cases are labeled as follows: Γ=(0,0,0), X=(0.5,0,0), Y=(0,0.5,0), Z=(0,0,0.5), V=(0.5,0.5,0), U=(0.5,0,0.5), T=(0,0.5,0.5) and R=(0.5,0.5,0.5).

Transfer integrals corresponding to hole (HOMO-HOMO) and electron (LUMO-LUMO) transport were also calculated by using the dimers extracted from the crystal structure; see Figure

6.3e for definitions of dimer types. The transfer integrals for dimers B are essentially zero for both materials. For TESADT, the transfer integrals show larger values for dimers A (102 meV and 77 meV for holes and electrons, respectively, Table 6.2) as compared to dimers ABx (4 meV and 1 meV, respectively) and ABy (34 meV and 21 meV, respectively). This indicates that for TESADT, both hole and electron transport are more efficient in the *a*-direction than in the *b*-direction, which is consistent with the findings from the band structure calculations. For diF-TESADT, only the characteristics of hole transport show larger dispersion and larger transfer integral in the *a*-direction (Table 6.2). In contrast, the transfer integral for electron transport for dimer ABy (40 meV) is larger than that for dimer A (6 meV). This may first seem to indicate better electron transport in the *b*-direction than in the *a*-direction for diF-TESADT. However, the orientation of the ABy dimer (Figure 6.3e) contributes roughly equally to electron transport in the *a*- and *b*-directions, which leads to a more balanced electron transport in the *ab*-plane as evidenced by the similar band dispersions between the Γ-X and Y-Γ directions (Figure 6.6b).

In summary, while fluorination of TESADT marginally is susceptible to improve hole transport in the dominant transport pathway (*a*-direction) by increasing the hole transfer integral of dimer A (113 meV up from 102 meV, Table 6.2), it reduces substantially the overall electron transport in the *ab*-plane – this includes a drastic reduction in the electron transfer integral of dimer A (6 meV down from 77 meV) but a notable increase in the electron transfer integral of dimer ABy (40 meV up from 21 meV). For hole and electron transport in TESADT and for hole transport in diF-TESADT, the "zig-zag" fashion by which transport occurs along the *b*-direction is expected to take place between dimers A and ABy (Figure 6.3e); all transfer integrals for dimer ABx should contribute negligibly (Table 6.2). For electron transport in diF-TESADT, transport in the *a*- and *b*-direction is expected to occur primarily via dimer ABy; the electron

transfer integral of dimer A should contribute negligibly. The origin of the detrimental effects of fluorination to electron transport properties for diF-TESADT will be discussed next.

Table 6.2 Transfer integrals for electron and hole transport for TESADT and diF-TESADT determined from DFT calculations of dimers within the crystal structure (between LUMO-LUMO and HOMO-HOMO, respectively) and band structures of the crystal. All values are in meV.

	t_e (electron)				t_h (hole)			
	dimer types[a]			BS[b]	dimer types[a]			BS[b]
	A	ABx	ABy	*W*/4	A	ABx	ABy	*W*/4
TESADT	77	1	21	95	102	4	34	130
diF-TESADT	6	0	40	43	113	1	27	135

[a]See Figure 6.3e for dimer type definitions; B3LYP/6-31G(d,p) level.

[b]*W* is the band width; B3LYP/6-21G(d,p) level.

We now turn to the hole and electron effective masses (m_{eff}) of TESADT and diF-TESADT, see Table 6.3, which are shown to be consistent with the results from the band structure and dimer calculations. The m_{eff} is a measure of the dispersion of the bands at the top of the valence band and bottom of the conduction band, with smaller values pointing to higher mobilities. The individual components of the m_{eff} eigenvectors along the crystallographic directions indicate the directionality and dimensionality of charge-carrier transport. In the case of TESADT, the results from the m_{eff} are consistent with those from the band structure and dimer calculations (Table 6.2): smaller effective masses are found for holes than for electrons for eigenvectors in the *ab*-plane (0.82 and 2.59 for hole versus 0.90 and 3.83 for electron, in electron mass units). Turning to diF-TESADT, the hole m_{eff} shows the same pattern as that for TESADT. The electron m_{eff} for

each eigenvector also shows the same pattern as in TESADT but with more balanced contributions from the *a*- and *b*-directions (1.00 and 0.90 respectively for the first eigenvector; -0.80 and 1.00 respectively for the second eigenvector), see Table 6.3. These results are consistent with the valence band dispersions and electron transfer integrals from the dimer calculations of diF-TESADT discussed above.

Table 6.3 Effective masses for electron and hole transport for TESADT and diF-TESADT obtained at the band extremes using the band structures determined from B3LYP/6-21G(d,p) calculations. m_{eff} is the effective mass along the various eigenvector directions in units of the electron rest mass m_0.

	electron				hole			
	m_{eff}	$\vec{a}$	$\vec{b}$	$\vec{c}$	m_{eff}	$\vec{a}$	$\vec{b}$	$\vec{c}$
TESADT	0.90	1.00	0.23	-0.01	0.82	1.00	0.36	0.00
	3.83	-0.02	1.00	-0.01	2.59	-0.17	1.00	-0.01
	27.43	0.35	0.48	1.00	53.89	0.32	0.42	1.00
diF-TESADT	1.26	1.00	0.90	-0.02	0.71	1.00	0.18	0.00
	7.45	-0.80	1.00	0.07	3.42	0.13	1.00	-0.01
	23.76	0.43	0.29	1.00	166.59	0.25	0.43	1.00

The results from the band structure, dimer, and effective mass calculations all point to the same conclusion: Hole transport properties are marginally improved but electron transport properties are substantially diminished upon fluorination of TESADT, particularly in the *a*-direction. We now examine the HOMOs and LUMOs of dimer A (Figure 6.7) to clarify on the origin of these results. Due to the structural displacement induced by the F atoms (Figure 6.4), the overlap of HOMOs in the dimer is slightly increased on going from TESADT to diF-TESADT ($S_{HOMO\text{-}HOMO}$

of 0.0172 and 0.0175 respectively). In contrast, the overlap of LUMOs in the dimer is more decreased ($S_{LUMO-LUMO}$ of -0.010 and -0.002, respectively). This analysis is consistent with the observed effects of fluorination on TESADT. We have thus been able to relate the structural modifications induced by fluorination to the charge-carrier transport properties in the crystalline structures of these anthradithiophene materials.

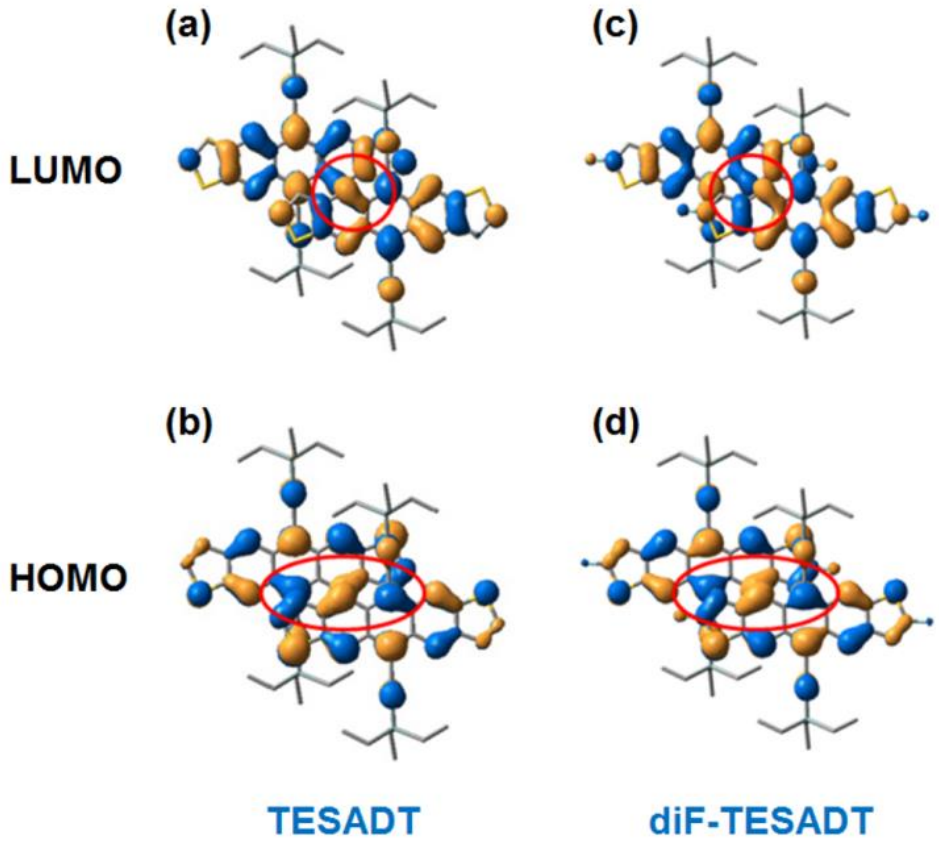

Figure 6.7 Diagrams showing the (a, c) LUMOs and (b, d) HOMOs of TESADT and diF-TESADT in the dimer configuration along the *a*-direction. Note the alignment in the phase of the HOMOs (b, d) for both materials and the increased overlap for diF-TESADT as highlighted by the red ellipses. In contrast, the phase of the LUMOs is misaligned for both materials as highlighted by the red circles.

The above comparisons between the charge transport properties of TESADT and diF-TESADT crystals employed a static picture with molecular configurations coming from the crystal structure. To assess the modulation of the electronic couplings by lattice vibrations, in the following we account for the effects of pressure and thermal motion at room temperature on the crystal packing using MD simulations. The distributions of the electronic coupling for holes for the various dimers within the crystals (Figure 6.3e) are shown in Figure 6.8. The means (μ) and standard deviations (σ) of the distributions were determined by fitting them to Gaussian functions (Figure 6.8). The distributions for dimer A show the same trend as observed from the static picture (Table 6.2), where the mean of the diF-TESADT distribution is ≈12 meV larger than that of TESADT. In contrast, the mean of the diF-TESADT distribution is ≈20 meV smaller than that of TESADT for dimer ABy. The effect of lattice vibrations has led the TESADT distribution to be centered at roughly zero, which is markedly different from the corresponding static value. Lastly, the distributions for dimer ABx are also in line with the static values reported above.

The distributions of the electronic coupling for electrons is shown in Figure 6.9 and reveal the same trends as the static values for dimers A and ABx. However, for dimer ABy, the mean of the TESADT distribution is slightly larger than that of diF-TESADT (μ = 22.7 meV versus 17.1 meV) while the static couplings show the opposite trend and by a larger extent (21 meV versus 40 meV, see Table 6.2).

In summary, the electronic coupling distributions reveal a dynamic picture of TESADT and diF-TESADT where fluorination is shown to detrimentally affect the charge transport properties in nearly all pathways within the crystal. The sole exception is the coupling distribution for holes for dimer A. The results here suggest that the higher hole mobility for diF-

TESADT (0.70 $cm^2\ V^{-1}\ s^{-1}$) versus TESADT (0.42 $cm^2\ V^{-1}\ s^{-1}$) in OFETs is due to the enhanced crystallinity from the surface treatment with pentafluorobenzene thiol rather than any significant improvements in the intrinsic charge transport properties within the crystal as a result of fluorination.

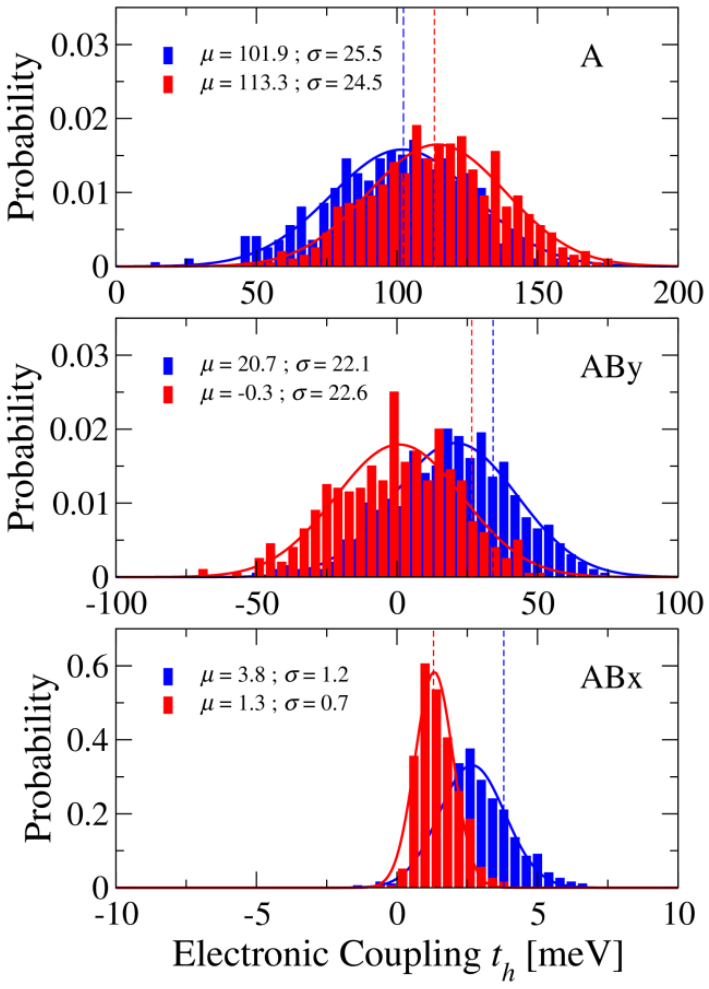

Figure 6.8 Distributions of the hole transfer integral (HOMO-HOMO) determined at the B3LYP/6-31G(d,p) level for the various dimer types within the TESADT (blue) and diF-TESADT (red) crystals at 298 K; see Figure 6.3e for definitions of dimer types. The vertical lines show values for dimers taken from the experimental crystal structures. The mean values are obtained from fitting the distributions to Gaussian functions. Note the order of magnitude differences in the abscissae.

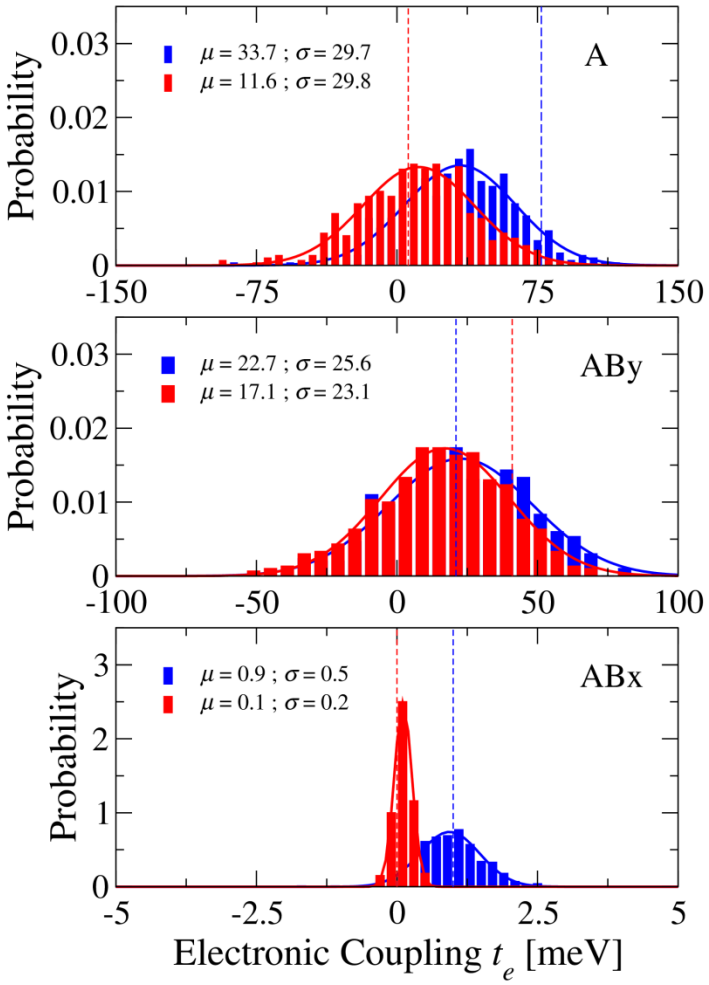

Figure 6.9 Distributions of the electron transfer integral (LUMO-LUMO) determined at the B3LYP/6-31G(d,p) level for the various dimer types within the TESADT (blue) and diF-TESADT (red) crystals at 298 K; see Figure 6.3e for definitions of dimer types. The vertical lines show values for dimers taken from the experimental crystal structures. The mean values are obtained from fitting the distributions to Gaussian functions. Note the order of magnitude differences in the abscissae.

6.4 Conclusions

We have carried out a comparative investigation of the anthradithiophene crystals TESADT and its fluorinated analog diF-TESADT, using a combination of theoretical and computational methodologies. Our goal was to relate the structural features of the crystals to their electronic properties, thereby evaluating the effect of fluorine substitution on the intrinsic transport

properties of the crystals. Our comparison of the two systems employed both a static and dynamic picture of the molecular packing and its effects on the electronic properties.

The main results from our work are as follows:

(i) Fluorine substitution of the anthradithiophene backbone in TESADT mainly causes a structural shift of ≈0.4 Å along the long axis of the backbone between adjacent molecules in the *a*-direction of the crystal structure.

(ii) While the small structural modifications lead to slightly enhanced hole transport properties in the *a*-direction, they significantly diminish the electron transport properties in all directions, especially when lattice vibrations are taken into account. Additionally, the hole transport properties in the *b*-direction and intermediate *ab*-directions are also diminished.

(iii) Given that the intrinsic crystal growth morphology of the two materials are found to be essentially the same, the results above suggest that the higher hole mobility for diF-TESADT (0.70 cm^2 V^{-1} s^{-1}) versus TESADT (0.42 cm^2 V^{-1} s^{-1}) in OFETs is mainly due to the enhanced crystallinity resulting from surface treatment rather than any significant improvements in the intrinsic charge transport properties of the crystal as a result of fluorination.

The results here demonstrate the importance of being able to discern intrinsic versus external factors that can lead to improved performance in OFETs.

6.5 References

(1) Sirringhaus, H. *Adv*. *Mater*. **2014**, *26* (9), 1319.
(2) Mei, J.; Diao, Y.; Appleton, A. L.; Fang, L.; Bao, Z. *J*. *Am*. *Chem*. *Soc*. **2013**, *135* (18), 6724.
(3) Wang, C.; Dong, H.; Hu, W.; Liu, Y.; Zhu, D. *Chem*. *Rev*. **2012**, *112* (4), 2208.
(4) Kim, C.-H.; Hlaing, H.; Payne, M. M.; Parkin, S. R.; Anthony, J. E.; Kymissis, I. *ChemPhysChem* **2015**, *16* (6), 1251.
(5) Gundlach, D. J.; Royer, J. E.; Park, S. K.; Subramanian, S.; Jurchescu, O. D.; Hamadani, B. H.; Moad, A. J.; Kline, R. J.; Teague, L. C.; Kirillov, O.; Richter, C. A.; Kushmerick, J. G.; Richter, L. J.; Parkin, S. R.; Jackson, T. N.; Anthony, J. E. *Nat*. *Mater*. **2008**, *7* (3), 216.
(6) Subramanian, S.; Park, S. K.; Parkin, S. R.; Podzorov, V.; Jackson, T. N.; Anthony, J. E. *J*. *Am*. *Chem*. *Soc*. **2008**, *130* (9), 2706.
(7) Jurchescu, O. D.; Hamadani, B. H.; Xiong, H. D.; Park, S. K.; Subramanian, S.; Zimmerman, N. M.; Anthony, J. E.; Jackson, T. N.; Gundlach, D. J. *Appl*. *Phys*. *Lett*. **2008**, *92* (13), 132103.
(8) Park, S. K.; Mourey, D. A.; Subramanian, S.; Anthony, J. E.; Jackson, T. N. *Appl*. *Phys*. *Lett*. **2008**, *93* (4), 043301.
(9) Yu, L.; Li, X.; Pavlica, E.; Loth, M. A.; Anthony, J. E.; Bratina, G.; Kjellander, C.; Gelinck, G.; Stingelin, N. *Appl*. *Phys*. *Lett*. **2011**, *99* (26), 263304.
(10) Kline, R. J.; Hudson, S. D.; Zhang, X.; Gundlach, D. J.; Moad, A. J.; Jurchescu, O. D.; Jackson, T. N.; Subramanian, S.; Anthony, J. E.; Toney, M. F.; Richter, L. J. *Chem*. *Mater*. **2011**, *23* (5), 1194.
(11) Niazi, M. R.; Li, R.; Qiang Li, E.; Kirmani, A. R.; Abdelsamie, M.; Wang, Q.; Pan, W.; Payne, M. M.; Anthony, J. E.; Smilgies, D.-M.; Thoroddsen, S. T.; Giannelis, E. P.; Amassian, A. *Nat*. *Commun*. **2015**, *6*, 8598.
(12) Jurchescu, O. D.; Subramanian, S.; Kline, R. J.; Hudson, S. D.; Anthony, J. E.; Jackson, T. N.; Gundlach, D. J. *Chem*. *Mater*. **2008**, *20* (21), 6733.
(13) Li, R.; Ward, J. W.; Smilgies, D.-M.; Payne, M. M.; Anthony, J. E.; Jurchescu, O. D.; Amassian, A. *Adv*. *Mater*. **2012**, *24* (41), 5553.
(14) Teague, L. C.; Hamadani, B. H.; Jurchescu, O. D.; Subramanian, S.; Anthony, J. E.; Jackson, T. N.; Richter, C. A.; Gundlach, D. J.; Kushmerick, J. G. *Adv*. *Mater*. **2008**, *20* (23), 4513.
(15) Lehnherr, D.; Waterloo, A. R.; Goetz, K. P.; Payne, M. M.; Hampel, F.; Anthony, J. E.; Jurchescu, O. D.; Tykwinski, R. R. *Org*. *Lett*. **2012**, *14* (14), 3660.
(16) Kohn, W.; Sham, L. J. *Phys*. *Rev*. **1965**, *140* (4A), A1133.
(17) Lee, C.; Yang, W.; Parr, R. G. *Phys*. *Rev*. *B* **1988**, *37* (2), 785.
(18) Becke, A. D. *J*. *Chem*. *Phys*. **1993**, *98* (7), 5648.
(19) Newton, M. D. *Chem*. *Rev*. **1991**, *91* (5), 767.
(20) Senthilkumar, K.; Grozema, F. C.; Bickelhaupt, F. M.; Siebbeles, L. D. A. *J*. *Chem*. *Phys*. **2003**, *119* (18), 9809.
(21) Valeev, E. F.; Coropceanu, V.; da Silva Filho, D. A.; Salman, S.; Brédas, J.-L. *J*. *Am*. *Chem*. *Soc*. **2006**, *128* (30), 9882.
(22) Jorgensen, W. L.; Maxwell, D. S.; Tirado-Rives, J. *J*. *Am*. *Chem*. *Soc*. **1996**, *118* (45), 11225.
(23) Hoover, W. G. *Phys*. *Rev*. *A* **1985**, *31* (3), 1695.

(24) Parrinello, M.; Rahman, A. *J*. *Appl*. *Phys*. **1981**, *52* (12), 7182.
(25) Ryckaert, J.-P.; Ciccotti, G.; Berendsen, H. J. C. *J*. *Comput*. *Phys*. **1977**, *23* (3), 327.
(26) Ewald, P. P. *Ann*. *Phys*. *64*, 253.
(27) Fonari, A.; Sutton, C. *ArXiv13024996 Cond-Mat* **2013**.
(28) Boys, S. F.; Bernardi, F. *Mol*. *Phys*. **1970**, *19* (4), 553.
(29) Grimme, S. *J*. *Comput*. *Chem*. **2006**, *27* (15), 1787.
(30) Frisch, M. J.; Trucks, G. W.; Schlegel, H. B.; Scuseria, G. E.; Robb, M. A.; Cheeseman, J. R.; Scalmani, G.; Barone, V.; Mennucci, B.; Petersson, G. A.; Nakatsuji, H.; Caricato, M.; Li, X.; Hratchian, H. P.; Izmaylov, A. F.; Bloino, J.; Zheng, G.; Sonnenberg, J. L.; Hada, M.; Ehara, M.; Toyota, K.; Fukuda, R.; Hasegawa, J.; Ishida, M.; Nakajima, T.; Honda, Y.; Kitao, O.; Nakai, H.; Vreven, T.; Montgomery Jr., J. A.; Peralta, J. E.; Ogliaro, F.; Bearpark, M. J.; Heyd, J.; Brothers, E. N.; Kudin, K. N.; Staroverov, V. N.; Kobayashi, R.; Normand, J.; Raghavachari, K.; Rendell, A. P.; Burant, J. C.; Iyengar, S. S.; Tomasi, J.; Cossi, M.; Rega, N.; Millam, N. J.; Klene, M.; Knox, J. E.; Cross, J. B.; Bakken, V.; Adamo, C.; Jaramillo, J.; Gomperts, R.; Stratmann, R. E.; Yazyev, O.; Austin, A. J.; Cammi, R.; Pomelli, C.; Ochterski, J. W.; Martin, R. L.; Morokuma, K.; Zakrzewski, V. G.; Voth, G. A.; Salvador, P.; Dannenberg, J. J.; Dapprich, S.; Daniels, A. D.; Farkas, Ö.; Foresman, J. B.; Ortiz, J. V.; Cioslowski, J.; Fox, D. J. *Gaussian 09*; Gaussian, Inc.: Wallingford, CT, USA, 2009.
(31) Plimpton, S. *J*. *Comput*. *Phys*. **1995**, *117* (1), 1.
(32) Hartman, P.; Bennema, P. *J*. *Cryst*. *Growth* **1980**, *49* (1), 145.
(33) Sun, H. *J*. *Phys*. *Chem*. *B* **1998**, *102* (38), 7338.
(34) Accelrys Software, Inc. *Materials Studio: Morphology Module*; Accelrys Software, Inc.: San Diego, 2007.
(35) Gruhn, N. E.; da Silva Filho, D. A.; Bill, T. G.; Malagoli, M.; Coropceanu, V.; Kahn, A.; Brédas, J.-L. *J*. *Am*. *Chem*. *Soc*. **2002**, *124* (27), 7918.
(36) Kwon, O.; Coropceanu, V.; Gruhn, N. E.; Durivage, J. C.; Laquindanum, J. G.; Katz, H. E.; Cornil, J.; Brédas, J. L. *J*. *Chem*. *Phys*. **2004**, *120* (17), 8186.
(37) Barbara, P. F.; Meyer, T. J.; Ratner, M. A. *J*. *Phys*. *Chem*. **1996**, *100* (31), 13148.

Chapter 7

Conclusions and Outlook

7.1 Conclusions

In this Thesis, we have aimed to elucidate clear connections between the chemical functionality and molecular morphologies of a number of high-performing or benchmark π-conjugated materials used in organic solar cells (OSCs). We have proceeded to link these structural features to the electronic properties that are important to solar cell performance. Using a combination of theoretical methodologies including density functional theory (DFT), molecular dynamics (MD), and coarse-grained (CG) simulations in tandem with experimental results such as solid-state NMR characterization and photovoltaic performance characteristics, we have linked the molecular morphologies from simulations directly and quantitatively to the molecular electronic properties. Following which, we have clarified semi-quantitatively or at least qualitatively how those electronic properties contribute to the materials and performance properties. We briefly summarize below the results from the individual investigations in this Thesis before discussing the general insights we have learned from those results.

In Chapter 3, we considered the PBDT[2X]T polymers as model systems to elucidate the molecular-scale effects that fluorine substituents induce on main-chain conformations, packing, and electronic couplings. The quantum chemical calculations of the intrinsic inter-monomer torsion profiles along the chains point to a clear propensity for backbone planarity in PBDT[2F]T and lower extents of backbone planarity in PBDT[2H]T. The solid-state NMR analyses and molecular dynamics simulations provide a consistent picture and indicate a prominence of (near) anti conformations along the PBDT[2H]T chains and coplanar syn conformations along the PBDT[2F]T chains. Importantly, compared to PBDT[2H]T, the higher propensity for backbone planarity seen in PBDT[2F]T leads to more pronounced, yet staggered, chain stacking in the solid state. As a result, higher inter-chain electronic couplings for holes and larger binding

energies between neighboring polymer chains are calculated in the fluorine-substituted polymer, with the former being consistent with the larger hole mobility measured for this material via SCLC experiments.

In Chapter 4, molecular simulations of P3HT:acene blends were performed to determine structure-morphology relationships relevant to organic BHJ solar-cell performance. By focusing on a matrix of nine acenes whose chemical structure is systematically varied in the nature of the alkyl groups and electron-withdrawing groups, connections between the chemical structure of the acene and P3HT and the molecular-scale properties within the blend can be made. The main results from this work are: (i) Diffusivity is observed to generally decrease with size of the alkyl group and strength of the electron-withdrawing group on the acene. (ii) Donor-acceptor interactions are enhanced by the electron-withdrawing group strength, but diminished primarily by steric bulk of the alkyl groups. (iii) The blend miscibility generally decreases with alkyl group size and increases with electron-withdrawing group strength. (iv) The trends in interfacial area between P3HT:acene "phases" reflect those in miscibility. (v) Blends with lower miscibility contain more extended P3HT chains.

In Chapter 5, we focused on a pair of rhodanine acceptors with an indacenodithiophene (IDTBR) or indenofluorene (IFBR) core, which are used with P3HT as the donor in ternary OSCs whose performance properties are observed to vary with the blend ratio. The quantum chemical calculations and molecular simulations reveal conformations along the molecular backbones that point to a clear propensity for backbone planarity in IDTBR and lower extents of backbone planarity in IFBR in both vacuum and the solid state. The evolution of the J_{SC}, V_{OC}, and EQE profiles for the ternary devices are qualitatively shown to be a consequence of the evolution of the electronic properties in the IDTBR:IFBR mixed phases, the origin of which

appears to stem from the competing effects between the protruding nature of the benzothiadiazole (BT) unit of IFBR and the planar nature of the BT unit of IDTBR. These differences are erased when either material is blended with P3HT. Lastly, the transfer integral distributions for electrons point to more efficient electron transport in the crystalline and amorphous phases of IDTBR than IFBR.

In Chapter 6, we performed a comparative investigation of the triethylsilylethynyl anthradithiophene crystals, TESADT and its fluorinated analog diF-TESADT, to evaluate the effect of fluorine substitution on the intrinsic charge-carrier transport properties of the crystals. While the systems studied here are specific to OFET devices, the results are general in that they demonstrate how quantum-chemical calculations and MD simulations can be used to evaluate the structural and electronic properties of the crystal, which for certain blend materials, have been observed to crystallize in the BHJ morphology of OSCs. In this Chapter, we find that while fluorine substitution mainly induces only a modest (≈0.4 Å) structural shift along the anthradithiophene backbone direction in the crystal structure, the resulting effects on the band structures, effective masses, and electronic couplings are substantial, especially when lattice vibrations are taking into account. The intrinsic crystal growth morphology of the two materials are found to be essentially the same, thus suggesting that the higher hole mobility for diF-TESADT versus TESADT in OFETs is mainly due to the enhanced crystallinity resulting from surface treatment rather than any significant improvements in the intrinsic charge transport properties of the crystal as a result of fluorination.

Having recapitulated the main results from the individual Chapters, we are in position to discuss the general insights we have learned from those results as they pertain to the molecular design of π-conjugated materials. In Chapter 1, we noted that from a molecular design

standpoint, synthetic chemists tend to focus on controlling the energy levels of the frontier orbitals through the concatenation of a combination of electron-deficient and electron-rich moieties and substitution groups. To a more qualitative extent, they attempt to influence the solubilities and thin-film morphologies of the materials by appending alkyl groups of various shapes and sizes. Below, we discuss several important molecular and materials parameters that, motivated by the theoretical and computational work in this Thesis, we believe should be considered in the design principles of new materials.

Regarding molecular properties, the results from our investigations of the PBDT[2X]T polymer donors (Chapter 3) and IXBR rhodanine acceptors (Chapter 5) underscore the importance of controlling the backbone torsion profiles of the π-conjugated materials, which is often neglected in the design strategies for new materials. From those Chapters, we have seen that molecules and chains with planar backbones can pack more closely with one another and exhibit higher degrees of chain stacking leading to higher binding energies and electronic couplings, which are expected to yield better materials stability and charge-carrier transport properties, respectively. Although these results are quite intuitive, the current understanding of which chemical functionality is required to yield backbone torsion profiles that favor planarity is still incomplete. Our results demonstrate that quantum chemical calculations, in particular DFT, can serve to screen for chemical structures with certain desirable torsion profiles. To that end, we recommend the long-range corrected functional ωB97X-D, which also has empirical dispersion corrections, for obtaining accurate torsion profiles – with correct barrier heights and locations of local minima – for extended π-conjugated systems. Our results indicate that the locations of the local or global minima in the torsion profiles play a more important role than the barrier heights in determining molecular packing configurations. We find that barrier heights as large as 6 kcal

mol^{-1} will still allow for inter-conversion between syn and anti conformations in solution at room temperature or in the melt at 550K and above.

Another point to consider regarding molecular properties is how much the frontier orbital energies can vary in the solid state due to intermolecular interactions. The results from Chapter 5 indicate that the LUMO (and HOMO) levels of the IDTBR and IFBR molecules can vary up to 0.5 eV (distribution range) with standard deviations of 0.07 eV. Moreover, the distributions can shift due to the presence of different component materials and their concentrations. These molecular parameters are important as they have been shown to correlate with the solar cell performance. The molecular detail of how the electronic properties evolve in the bulk and blend phases is only accessible from a computational study where all atoms take known values. Thus, molecular simulations that take into account the effects of intermolecular interactions can be an indispensable tool in the effort to develop material design principles.

Lastly, we believe the ability to systematically tailor the dynamics, miscibility, and morphology of π-conjugated materials (Chapter 4) through modifying chemical functionality is an important tool to develop. The morphological features of the bulk-heterojunction such as domain size, purity, and connectivity and interfacial area, orientation, and roughness are all expected to play a role in determining photovoltaic performance in OSCs. The systematic study of the P3HT:acene blends in Chapter 4 demonstrates that it is possible to disentangle the effects of electrostatic and steric interactions involved in the formation of those morphological properties, thereby allowing one to predict more precisely the impact of chemical substituents on the morphology.

The molecular-scale insights into the BHJ morphology as developed from simulations and theoretical methodologies in this Thesis are especially valuable when they are shown to be consistent with or validated by experimental results. In Chapter 3, we have demonstrated how the combination of quantum chemical calculations, MD simulations, and solid-state NMR characterizations can be utilized to develop a comprehensive picture of the molecular morphology of a π-conjugated polymer system that is consistent with its performance characteristics. The success of our work indicates that the combined methodologies can be repeatedly implemented to investigate other π-conjugated systems that are relevant to BHJ OSCs or thin-film organic electronic applications in general.

7.2 Outlook

In the previous Section, we have used the work from this Thesis to argue for the incorporation of theoretical and computational methodologies with organic synthesis in searching the chemical space for new materials with desirable morphological and electronic properties for OSC applications. However, in our work, we have only related the molecular morphologies to the molecular electronic properties. To be of greater value, the computational techniques should be able to relate the molecular morphologies directly to the various relevant materials and device processes such as charge-carrier generation, recombination, and transport. To the best of our knowledge, the recent work of Jones *et al*.[1] is a first example of a theoretical study that has related the molecular morphology of a π-conjugated polymer system (P3HT) containing realistically long chains [modeled via CG simulations] to the hole mobility, via kinetic Monte-Carlo (KMC) simulations. The hole mobility was approximated through semiempirical quantum-

chemical evaluations of the charge-transfer rates between molecular sites following the semiclassical Marcus equation, where the rates are proportional to the square of the electronic couplings. More importantly, the work of Jones *et al*. was able to elucidate the molecular mechanism responsible for the observed higher hole mobility in P3HT as a function of increased annealing temperature and molecular weight.

The next step forward is to derive the molecular morphology of the donor-acceptor blends from solution. In this way, the blend morphology can be as realistic as possible. Several simulation studies have already begun to investigate the formation of a few π-conjugated polymers and molecules in solution.[2–5] We have also began to study the PBDT[2F]T:PCBM blends (Chapter 2) and P3HT:acene blends (Chapter 4) in solution. The resulting morphology can then be fed into kinetic Monte Carlo simulation models to relate the morphology to the relevant processes in photovoltaic operation such as geminate and non-geminate recombination, charge transport, charge injection and extraction.[6,7] We expect that in the foreseeable future, systematic relationships between the chemical functionality of π-conjugated materials and their photovoltaic performance properties can be developed directly from theoretical and computational methodologies.

7.3 References

(1) Jones, M. L.; Huang, D. M.; Chakrabarti, B.; Groves, C. *J*. *Phys*. *Chem*. *C* **2016**, *120* (8), 4240.
(2) Schwarz, K. N.; Kee, T. W.; Huang, D. M. *Nanoscale* **2013**, *5* (5), 2017.
(3) Lee, C.-K.; Pao, C.-W. *J*. *Phys*. *Chem*. *C* **2014**, *118* (21), 11224.
(4) Wang, C. I.; Hua, C. C. *J*. *Phys*. *Chem*. *B* **2015**, *119* (45), 14496.
(5) Chiu, M.; Kee, T. W.; Huang, D. M. *Aust*. *J*. *Chem*. **2012**, *65* (5), 463.
(6) Groves, C. *Energy Environ*. *Sci*. **2013**, *6* (11), 3202.
(7) Lyons, B. P.; Clarke, N.; Groves, C. *Energy Environ*. *Sci*. **2012**, *5* (6), 7657.

Appendix A

Supplementary Information for Chapter 3

Polymer Synthesis and Molecular Weight Determination

The PBDT[2X]T polymers were synthesized as previously described.[1] All reagents from commercial sources were used without further purification. Reactions were carried out under nitrogen atmosphere. Solvents were dried and purified using standard techniques. Flash chromatography was performed with analytical-grade solvents using Silicycle Silica Flash P60 (particle size 40-63 μm, 60 Å, 230 – 400 mesh) silica gel. Flexible plates PE SilG/UV 250μm from Whatman were used for TLC. Compounds were detected by UV irradiation or staining with I2, unless otherwise stated. Recycling GPC in ethanol-blended chloroform was carried out through a set of two JAIGEL-4H-40 preparative SEC columns mounted on a LC-9130NEXT (JAI) system equipped with coupled UV-254NEXT and RI-700NEXT detectors. Size exclusion chromatography (SEC) was performed with 1,3,5-trichlorobenzene (TCB) at an elution rate of 1.0 mL/min (injection volume: 200 μL) through a PL gel MIXED-B column (10 μm) (+PL gel guard), at 135 °C. The SEC system consisted of an Alliance 2000 separation module equipped with RI detector. The apparent molecular weights and polydispersities (M_w/M_n) were determined with a calibration based on linear polystyrene (PS) standards. The polymers before the injection were dissolved in hot TCB (125 °C) and then filtered hot using Millex – SV (5 μm) filters.

Table A1 SEC analyses of the PBDT[2X]T derivatives used in this study.

Polymer	M_n [kDa]	M_w [kDa]	PDI
PBDT[2F]T	11	22	2.0
PBDT[2H]T	16	37	2.3

SCLC Measurements

The carrier mobilities of the PBDT[2X]T polymers were determined by fitting the dark current to the space-charge-limited current (SCLC) model using the following diode configuration: glass/ITO/PEDOT:PSS/Polymer layer/MoO_3/Ag.

ITO substrates were first scrubbed with dilute Extran 300 detergent solution to remove organic residues before immersion into an ultrasonic bath of dilute Extran 300 for 20 min. Samples were rinsed in flowing deionized water for 5 min before being sonicated (Branson 5510) for 10 min each in successive baths of acetone and isopropanol. Next, the samples were dried with pressurized nitrogen before being exposed to a UV−ozone plasma for 10 min. An aqueous solution of PEDOT:PSS (Clevios P VP AI 4083) was spin-cast at 4,000 rpm onto the substrates and the PEDOT-coated substrates were annealed at 140 °C for 15 min. Immediately after the annealing step, the samples were transferred into a dry nitrogen glovebox (< 3 ppm O_2) for active layer deposition.

The polymers were dissolved in chlorobenzene with 5% (v/v) CN at polymer concentrations of 20 mg/mL, the polymer solution were spin-coated onto PEDOT-coated substrates, and the thin films were allowed to dry under nitrogen atmosphere for over 1 hour. The film thicknesses were varied by employing different spin-casting rates. Molybdenum oxide (7 nm) was used as an electron-blocking layer in the hole-only diodes. Silver cathodes (100 nm) were thermally evaporated (~10^{-6} Torr) through a shadow mask defining an active area of 0.1 cm^2. The electric-field dependent SCLC mobility was estimated using Equation A1.[2]

$$J(V) = \frac{9}{8}\varepsilon_0\varepsilon_r\mu_0 \exp\left(0.89\beta\sqrt{\frac{V - V_{bi}}{L}}\right)\frac{(V - V_{bi})^2}{L^3} \quad \text{(A1)}$$

Definition	Variable	Units
zero-field mobility	μ_0	$cm^2\ V^{-1}\ s^{-1}$
film thickness	L	cm
dark current density	J	$mA\ cm^{-2}$
voltage	V	V
vacuum permittivity	ε_0 (88.54×10^{-12})	$mA\ s\ V^{-1}\ cm^{-1}$
dielectric constant	ε_r (3)	
field activation factor	β	$cm^{1/2}\ V^{-1/2}$

Table A2 Zero-field hole mobilities of PBDT[2H]T as a function of film thickness.

Film thickness (nm)	Zero-field mobility ($cm^2\ V^{-1}\ s^{-1} \times 10^{-7}$)	Field activation factor ($\times 10^{-3}$)	Adj. R-square
300	3.82 ± 0.15	6.50	0.999
130	8.31 ± 0.11	5.36	0.999
90	9.78 ± 1.41	8.11	0.993

Table A3 Zero-field hole mobilities of PBDT[2F]T as a function of film thickness.

Film thickness (nm)	Zero-field mobility ($cm^2\ V^{-1}\ s^{-1} \times 10^{-6}$)	Field activation factor ($\times 10^{-4}$)	Adj. R-square
90	6.01 ± 0.07	5.45	0.999
60	6.00 ± 0.02	0	0.998
40	3.61 ± 0.02	0	0.991

Convergence of Inter-Monomer Torsion Profile

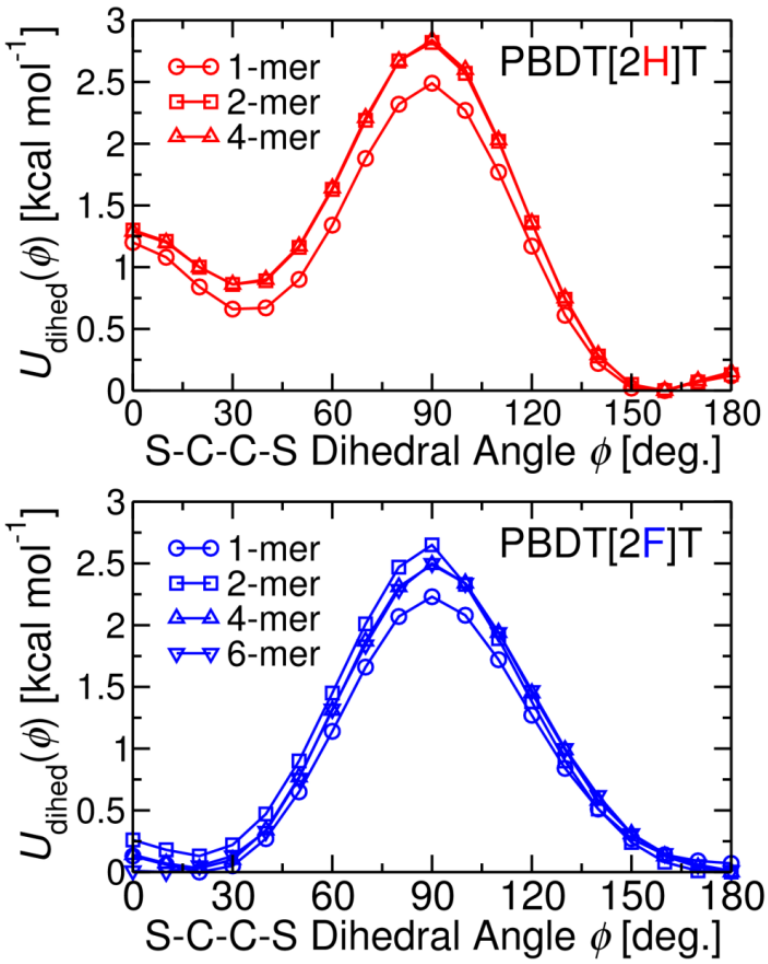

Figure A1 Inter-monomer torsion profiles of PBDT[2X]T at increasing chain length determined from DFT-ωB97XD/6-31G(d,p) calculations.

Parameterization of MD Dihedral Parameters from DFT Calculations

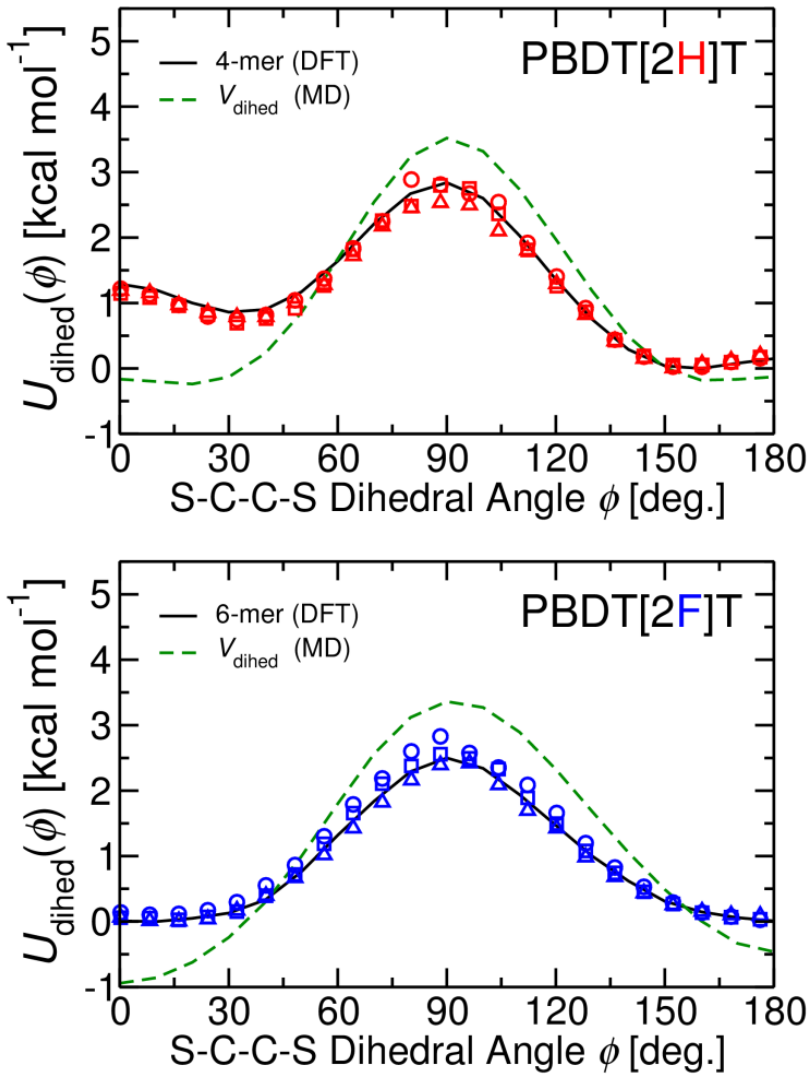

Figure A2 Converged inter-monomer torsion profile for PBDT[2X]T determined from DFT-ωB97XD/6-31G(d,p) calculations (solid) along with the torsion profiles (estimated as a free energy) at finite temperatures (circles, squares, and triangles indicate 300, 400, and 500 K, respectively) obtained from NVT simulations of a trimer chain in vacuum using the optimized dihedral potential (shown by the dashed green line).

Inter-Monomer Dihedral Distributions at 298 K

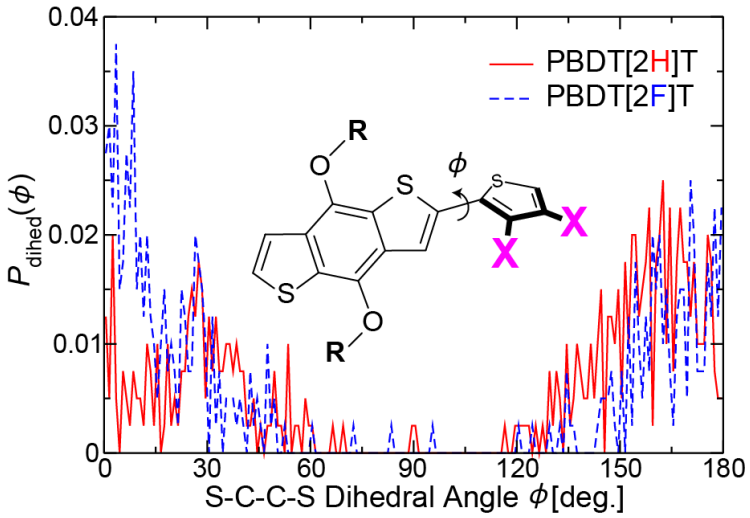

Figure A3 The inter-monomer dihedral distributions determined from constant NPT simulations of 80 5-mer chains of PBDT[2X]T at 298 K after cooling down from 550 K over 10 ns. These distributions are consistent with those obtained from higher temperature simulations.

$^{13}C\{^1H\}$ REPT-HDOR of PBDT[2X]T

To corroborate the isotropic ^{13}C chemical shifts identified with the static conformers of the polymers, as opposed to some dynamically averaged species, 2D $^{13}C\{^1H\}$ REPT-HDOR experiments were performed. In these experiments, the site-specific effective ^{13}C-^1H heteronuclear dipolar coupling constant (D) is determined, which is sensitive to dynamics experienced by the ^{13}C-^1H spin pair.[3] For a C-H group (such as those present in the thiophenes) that is rigid, a static dipolar coupling constant (D_{rigid}) of 21.0 kHz is expected.[4] Any motion experienced by a particular C-H group would result in a smaller D value, and the local order parameter (S) can be determined via the equation:

$$S = \frac{D}{D_{\text{rigid}}} \tag{A2}$$

The site-specific ^{13}C-^{1}H dipole-dipole sidebands of the major unambiguous peaks in the spectra of the PBDT[2X]T polymers are measured from the 2D $^{13}C\{^{1}H\}$ REPT-HDOR experiments as shown in Figure A4, and indicate fairly large D values (above 18 kHz), resulting in S values close to 0.9. This indicates that relatively static conformers are present in both polymers, precluding the possibility that the moieties represented by these isotropic ^{13}C chemical shifts are undergoing any fast motion relative to the NMR timescale, i.e., motions that occur on the sub-microsecond timescale.

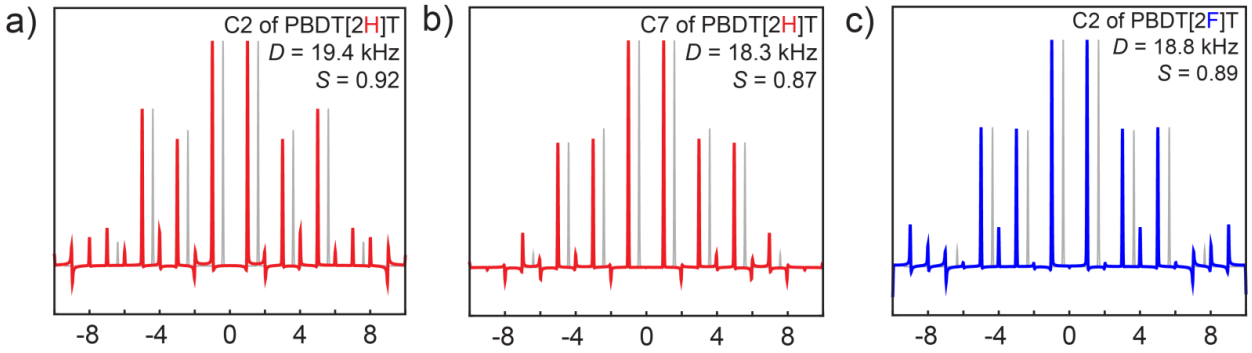

Figure A4 1D ^{13}C-^{1}H dipole-dipole sideband patterns recorded via 2D $^{13}C\{^{1}H\}$ REPT-HDOR experiments of the carbons numerically labeled in the chemical structure shown in Figure 3.4. These spectra pertain to carbon positions (a) 2 and (b) 7 of PBDT[2H]T (114 ppm and 124 ppm, respectively) and (c) 2 of PBDT[2F]T (117 ppm). The grey spectra represent simulations of the frequency dependent ^{13}C-^{1}H dipole-dipole sidebands patterns, from which the effective dipolar coupling constant (D) and the order parameter (S) were derived.

2D $^{13}C\{^{1}H\}$ FSLG HETCOR of PBDT[2X]T

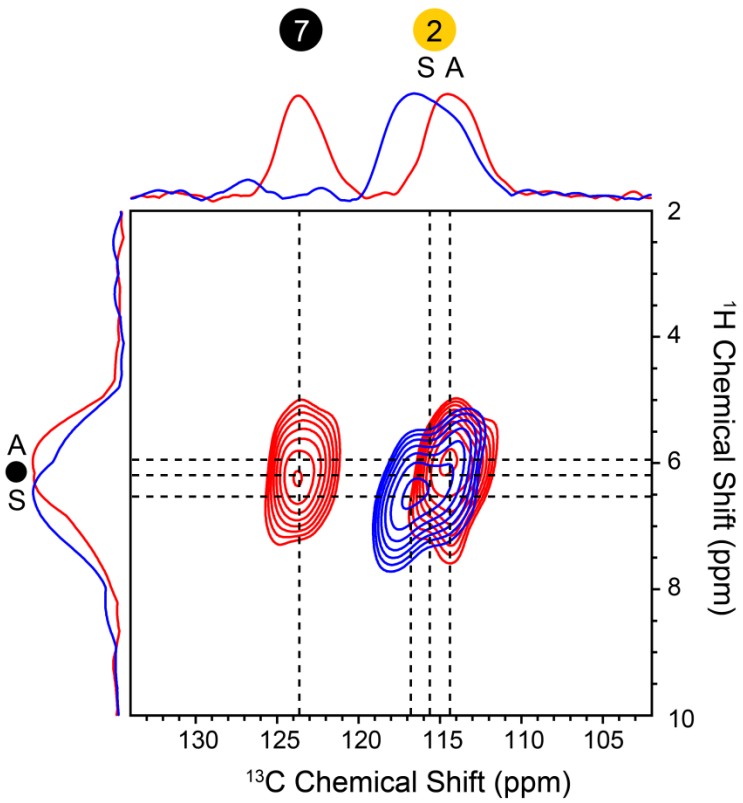

Figure A5 2D $^{13}C\{^{1}H\}$ FSLG HETCOR spectra of the thiophene region for PBDT[2H]T (red) and PBDT[2F]T (blue). An LG-CP time of 50 µs was used. Labels correspond to those shown in Figure 3.8.

Theoretical NMR Isotropic ^{13}C Chemical Shifts

Here, we discuss the results of our DFT calculations that were performed to obtain theoretical values for the isotropic ^{13}C chemical shifts (δ) using the gauge-including atomic orbital (GIAO)[24] method. These calculations were performed at the ωB97XD/6-31G(d,p) level using the Gaussian 09 Rev. D.01 code and the "NMR" keyword. The systems studied were tetramers of the PBDT[2X]T polymers where the conformation about the central bond between the 2nd and 3rd repeat units is configured to be near syn and anti with geometry optimization.

The theoretical ^{13}C chemical shift for TMS was determined to be 196.8 ppm, which compares reasonably well with the experimental value of 188.1 ppm. The chemical shifts for the PBDT[2X]T tetramers are determined relative to this reference. Focusing first on PBDT[2F]T, the chemical shifts for carbon 2 (see Figure 1a in the main article) are δ = 112.5 ppm and δ =117.0 ppm relative to TMS for the anti and syn conformers, respectively. These values compare very well with those obtained by fitting Gaussian functions to the experimental chemical shifts as shown in Figure 3.5. Turning to PBDT[2H]T, the chemical shifts for carbon 2 are δ = 114.2 ppm and δ = 114.4 ppm relative to TMS for the anti and syn conformers, respectively. The difference in chemical shift for the anti and syn conformers in this case is smaller, a trend consistent with the experimental values. In summary, these calculations provide additional support of our assignment of the syn and anti conformers in the experimental spectra.

Force-Field and Parameterization Details

The PBDT[2X]T polymers were modeled using the OPLS-AA[3] force field as template. Atomic charges were updated to ESP charges derived from DFT-ωB97XD[4]/6-31G(d,p) calculations of a geometry optimized tetramer. Likewise, bond lengths and angles were updated while their corresponding force constants were kept unchanged. The inter-monomer dihedral parameters (S-Cr-Cr-S, S-Cr-Cr-Cr, and Cr-Cr-Cr-Cr) were parameterized to reproduce the DFT torsion profile at finite temperatures as described in the Computational Methodology section of Chapter 3. The analytical form of the various bonded and non-bonded interaction potentials are shown below:

$$V_{\text{bond}}(l) = k_l(l - l_0)^2$$

$$V_{\text{angle}}(\theta) = k_\theta(\theta - \theta_0)^2$$

$$V_{\text{dihedral}}(\varphi) = \sum_{n=1}^{5 \text{ or } 9} A_n \cos^{n-1}(\varphi)$$

$$V_{\text{LJ}}(r_{ij}) = 4\varepsilon_{ij}\left[\left(\frac{\sigma_{ij}}{r_{ij}}\right)^{12} - \left(\frac{\sigma_{ij}}{r_{ij}}\right)^{6}\right],$$

with combining rules $\sigma_{ij} = \sqrt{\sigma_{ii}\sigma_{jj}}$ and $\varepsilon_{ij} = \sqrt{\varepsilon_{ii}\varepsilon_{jj}}$

$$V_{\text{Coulomb}}(r_{ij}) = \frac{q_i q_j e^2}{4\pi\epsilon_0 r_{ij}}$$

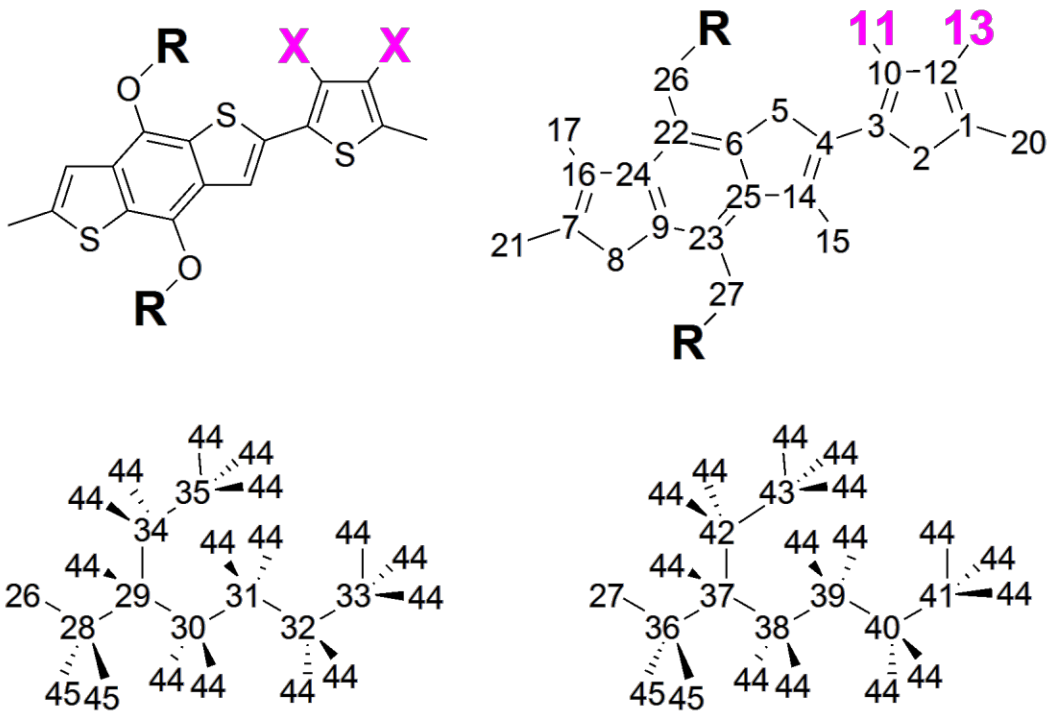

Figure A6 Chemical structures of PBDT[2X]T with atom types defined. Atom types 1 and 7 are replaced by 18 and 19, respectively, when the monomer is a chain terminus. This change is implemented to constrain the chain to charge neutrality.

Table A4 Atom types with pairwise non-bonded potential parameters (Lennard-Jones and Coulomb) for PBDT[2X]T. See Figure A6 for atom type definitions.

atom type	label	mass [amu]	σ_{ii} [Å]	ε_{ii} [kcal mol^{-1}]	PBDT[2H]T q_i [e]	PBDT[2F]T q_i [e]
1	Cr	12.011	3.550	0.070	0.0302	-0.1116
2	S	32.065	3.550	0.250	-0.0180	-0.0628
3	Cr	12.011	3.550	0.070	-0.0393	-0.1310
4	Cr	12.011	3.550	0.070	0.0000	0.0287
5	S	32.065	3.550	0.250	-0.0464	-0.0351
6	Cr	12.011	3.550	0.070	-0.0402	-0.0124
7	Cr	12.011	3.550	0.070	0.0098	0.0423
8	S	32.065	3.550	0.250	-0.0399	-0.0444
9	Cr	12.011	3.550	0.070	-0.0688	-0.0048
10	CA	12.011	3.550	0.070	-0.0804	0.2355
11	HA	1.008	2.420	0.030	0.1433	-0.1205
12	CA	12.011	3.550	0.070	-0.1934	0.1765
13	HA	1.008	2.420	0.030	0.1661	-0.1088
14	CA	12.011	3.550	0.070	-0.0565	-0.0602
15	HA	1.008	2.420	0.030	0.1332	0.1681
16	CA	12.011	3.550	0.070	-0.0886	-0.1013
17	HA	1.008	2.420	0.030	0.1461	0.1848
18	CA (tail)	12.011	3.550	0.070	-0.1834	-0.3514
19	CA (head)	12.011	3.550	0.070	-0.1963	-0.2147
20	HA (tail)	1.008	2.420	0.030	0.2069	0.2730
21	HA (head)	1.008	2.420	0.030	0.2128	0.2238
22	CA	12.011	3.550	0.070	0.2745	0.2855
23	CA	12.011	3.550	0.070	0.2534	0.2848
24	CA	12.011	3.550	0.070	-0.1380	-0.1856
25	CA	12.011	3.550	0.070	-0.1040	-0.1942
26	O	15.999	2.900	0.140	-0.3260	-0.3365
27	O	15.999	2.900	0.140	-0.3319	-0.3394
28	CT (i)	12.011	3.500	0.033	0.1474	0.1612
29	CT (ii)	12.011	3.500	0.033	-0.0600	"
30	CT (iii)	12.011	3.500	0.033	-0.1200	"
31	CT (iv)	12.011	3.500	0.033	-0.1200	"
32	CT (v)	12.011	3.500	0.033	-0.1200	"
33	CT (vi)	12.011	3.500	0.033	-0.1800	"
34	CT (vii)	12.011	3.500	0.033	-0.1200	"
35	CT (viii)	12.011	3.500	0.033	-0.1800	"
36	CT (i)	12.011	3.500	0.033	0.1474	0.1612
37	CT (ii)	12.011	3.500	0.033	-0.0600	"
38	CT (iii)	12.011	3.500	0.033	-0.1200	"
39	CT (iv)	12.011	3.500	0.033	-0.1200	"
40	CT (v)	12.011	3.500	0.033	-0.1200	"
41	CT (vi)	12.011	3.500	0.033	-0.1800	"
42	CT (vii)	12.011	3.500	0.033	-0.1200	"
43	CT (viii)	12.011	3.500	0.033	-0.1800	"
44	HT (alkane)	1.008	2.500	0.030	0.0600	"
45	HT (>CHOR)	1.008	2.500	0.030	0.0300	"

Table A5 Harmonic bond potential parameters for PBDT[2X]T.

		PBDT[2H]T		PBDT[2F]T	
bond type	label	k_l [kcal mol^{-1} Å^{-2}]	l_0 [Å]	k_l [kcal mol^{-1} Å^{-2}]	l_0 [Å]
1	S-Cr	291.25	1.738	"	1.744
2	S-Cr	291.25	1.761	"	1.763
3	S-Cr	291.25	1.746	"	1.745
4	Cr-Cr	514.27	1.372	"	1.365
5	Cr-Cr	514.27	1.360	"	1.363
6	Cr-Cr	514.27	1.416	"	1.416
7	(Cr-)Cr-Cr(-H)	453.10	1.417	"	1.418
8	(Cr-)Cr-Cr(-H)	453.10	1.435	"	1.433
9	Cr-CA (S-side)	469.00	1.388	"	1.388
10	Cr-CA (H-side)	469.00	1.399	"	1.399
11	CA-HA	370.63	1.084	"	1.083
12	CA-HA (head)	370.63	1.081	"	1.081
13	CA-HA (tail)	370.63	1.081	"	1.079
14	CA-CA (inter-ring)	392.29	1.453	"	1.449
15	CA-O	450.00	1.368	"	"
16	CT-O	320.00	1.424	"	"
17	CT-CT	268.00	1.529	"	"
18	CT-HC	340.00	1.090	"	"
19	Cr-F	--	--	420.00	1.331

Table A6 Harmonic angle potential parameters for PBDT[2X]T.

angle type	label	PBDT[2H]T		PBDT[2F]T	
		k_θ [kcal mol^{-1} rad^{-2}]	θ_0 [deg.]	k_θ [kcal mol^{-1} rad^{-2}]	θ_0 [deg.]
1	Cr-S-Cr	86.360	91.981	"	93.095
2	Cr-S-Cr	86.360	90.877	"	90.658
3	S-Cr-Cr	86.360	110.752	"	109.377
4	S-Cr-Cr	86.360	112.599	"	112.599
5	S-Cr-Cr	86.360	111.467	"	112.647
6	Cr-Cr-Cr	39.582	113.245	"	114.081
7	Cr-Cr(-H)-Cr	39.582	113.179	"	113.175
8	(Cr-)Cr-Cr-H/F	35.263	123.750	80.000	121.368
9	(Cr-)Cr-Cr-H	35.263	123.100	"	122.739
10	(S-)Cr-Cr-H/F	35.263	122.982	80.000	124.552
11	(S-)Cr-Cr-H	35.263	123.719	"	124.080
12	Cr-Cr-Cr (inter-ring)	54.694	128.231	"	127.992
13	S-Cr-Cr (inter-ring)	41.740	120.087	"	120.997
14	Cr-Cr-H (head)	35.263	127.157	"	127.158
15	Cr-Cr-H (tail)	35.263	128.178	"	127.803
16	S-Cr-H (head)	28.787	119.027	"	119.012
17	S-Cr-H (tail)	28.787	120.026	"	121.413
18	Cr-CA-Cr	63.000	117.941	"	117.862
19	(S-)Cr-Cr-CA	63.000	119.668	"	119.860
20	(Cr-)Cr-Cr-CA	63.000	122.389	"	122.265
21	Cr-CA-O (S-side)	70.000	120.860	"	121.010
22	Cr-CA-O (H-side)	70.000	121.194	"	121.110
23	CA-O-CT	75.000	113.489	"	"
24	O-CT-CT	50.000	109.500	"	"
25	O-CT-HC	35.000	109.500	"	"
26	CT-CT-CT	58.350	112.700	"	"
27	CT-CT-HC	37.500	110.700	"	"
28	HC-CT-HC	33.000	107.800	"	"
29	S-Cr-CA	63.000	126.144	"	"
30	(H-)Cr-Cr-CA	63.000	128.454	"	"
31	Cr-Cr-Cr(-H)	63.000	111.878	"	"

Table A7 Dihedral potential parameters for PBDT[2X]T. All units are kcal mol^{-1}. Parameters in red and blue correspond to PBDT[2H]T and PBDT[2F]T, respectively.

label	A_1	A_2	A_3	A_4	A_5	A_6	A_7	A_8	A_9
S-Cr-Cr-S	0.8798	-0.0529	-2.0670	-0.2157	1.7980	0.5874	-1.4309	-0.3231	0.7838
Cr-Cr-Cr-Cr	0.8798	-0.0529	-2.0670	-0.2157	1.7980	0.5874	-1.4309	-0.3231	0.7838
Cr-Cr-Cr-S	0.8798	0.0529	-2.0670	0.2157	1.7980	-0.5874	-1.4309	0.3231	0.7838
S-Cr-Cr-S	0.8403	-0.1062	-1.3884	-0.1558	0.2765	0.2284	0.4362	-0.0267	-0.3400
Cr-Cr-Cr-Cr	0.8403	-0.1062	-1.3884	-0.1558	0.2765	0.2284	0.4362	-0.0267	-0.3400
Cr-Cr-Cr-S	0.8403	0.1062	-1.3884	0.1558	0.2765	-0.2284	0.4362	0.0267	-0.3400
backbone rings[1]	7.2500	0.0000	-7.2500	0.0000	0.0000				
backbone rings[2]	2.2000	0.0000	-2.2000	0.0000	0.0000				
O-CT-CT-HT	0.2340	-0.7020	0.0000	0.9360	0.0000				
CA-O-CT-HT	0.3800	-1.1400	0.0000	1.5200	0.0000				
CA-CA-O-CT	1.5000	0.0000	-3.0000	0.0000	0.0000				
CA-O-CT-CT	0.0000	0.0000	0.0000	0.0000	0.0000				
O-CT-CT-CT	0.7000	0.3500	0.050	0.4000	0.0000				
CT-CT-CT-CT	0.7000	0.3500	0.050	0.4000	0.0000				
CT-CT-CT-HC	0.1500	-0.4500	0.0000	0.6000	0.0000				
HC-CT-CT-HC	0.1500	-0.4500	0.0000	0.6000	0.0000				

[1]Proper dihedrals to keep backbone ring atoms planar.
[2]Improper dihedrals to keep backbone ring atoms planar.

References

(1) Wolf, J.; Cruciani, F.; El Labban, A.; Beaujuge, P. M. *Chem. Mater.* **2015**, *27* (12), 4184.
(2) Murgatroyd, P. N. *J. Phys. Appl. Phys.* **1970**, *3* (2), 151.
(3) Hansen, M. R.; Graf, R.; Spiess, H. W. *Acc. Chem. Res.* **2013**, *46* (9), 1996.
(4) Saalwächter, K.; Graf, R.; Spiess, H. W. *J. Magn. Reson.* **2001**, *148* (2), 398.

Appendix B

Supplementary Information for Chapter 4

Self-diffusion in pure acene systems

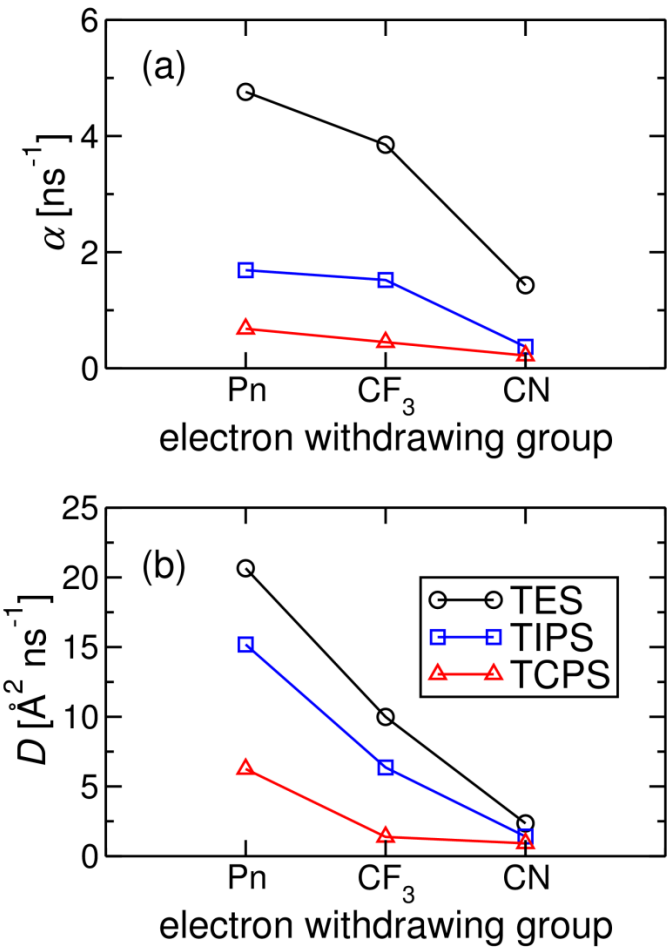

Figure B1 Acene diffusivity determined from atomistic NPT simulations of pure systems at 550 K and 1 atm. The trends in mixed systems with P3HT are the same. The coefficients α and D correspond to orientational and translational diffusion, respectively.

Energetic barrier for diffusion

Molecular diffusivity is an important consideration for thermal annealing, where temperatures between 50 to 220 °C (roughly 320-490 K) are used to post-process solution-cast morphologies. Sufficiently high thermal energy to overcome E_a (characterizing in part the temperature dependence of diffusivity as obtained from the Arrhenius equation) could allow for energetically

favorable molecular reorganization leading to higher structural order in thin films; however, too large an excess of thermal energy would diminish the order already present in the thin film before annealing. From fits of the Arrhenius equation (using data at 450, 550, and 650 K), energetic barriers for the diffusion of pure acenes range from 10 to 14 kcal mol^{-1}; values for the mixed systems are expected to be slightly higher. The narrow E_a range for these acenes suggests similar behavior during thermal annealing with P3HT.

Pair interactions between hexyl-chain and pentacene backbone

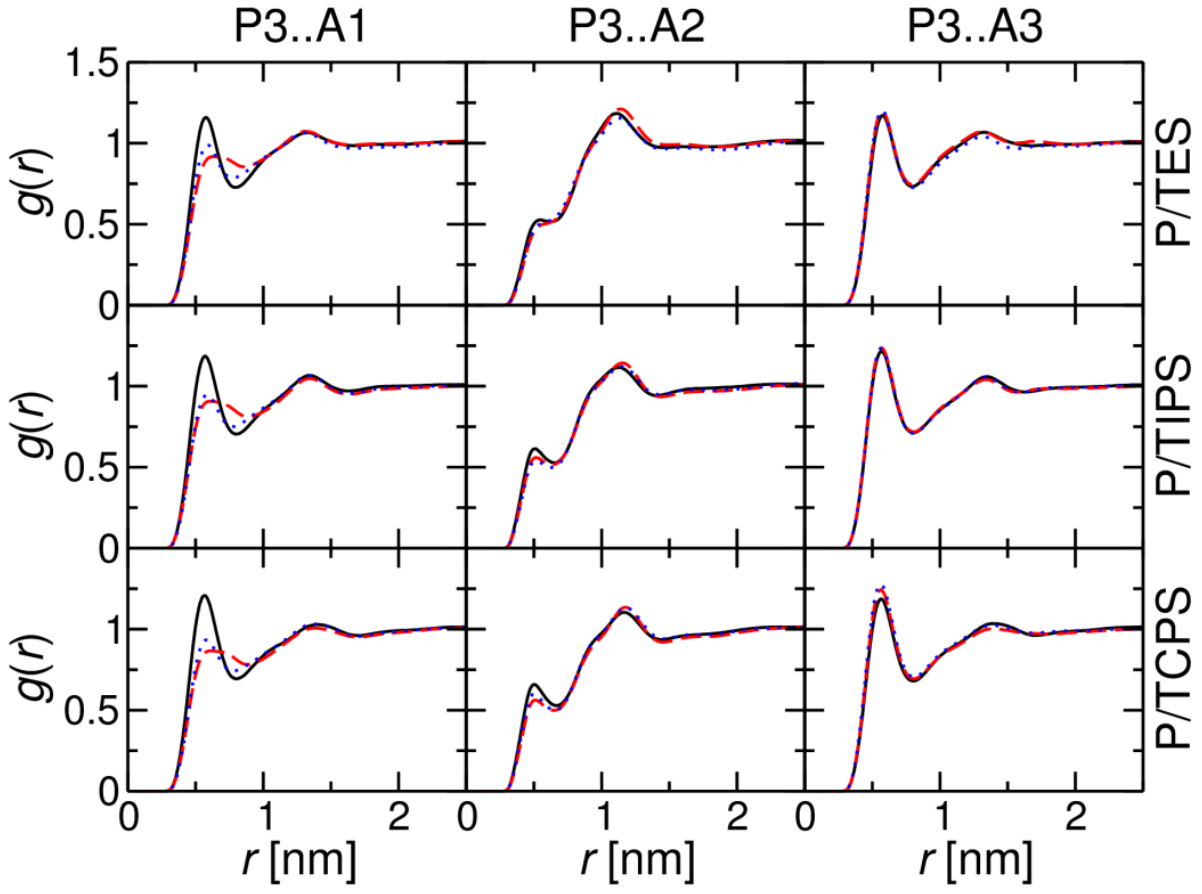

Figure B2 Radial distribution functions, $g(r)$, among non-bonded sites P3 of P3HT and A1-A3 of the acenes, determined from atomistic NPT simulations of P3HT:acene mixtures at 550 K and 1 atm. Solid, dashed, and dotted lines denote the unsubstituted, CF_3-, and CN-substituted acene, respectively. See Figure 4.3 for site definitions.

Miscibility at elevated temperature of 550 K

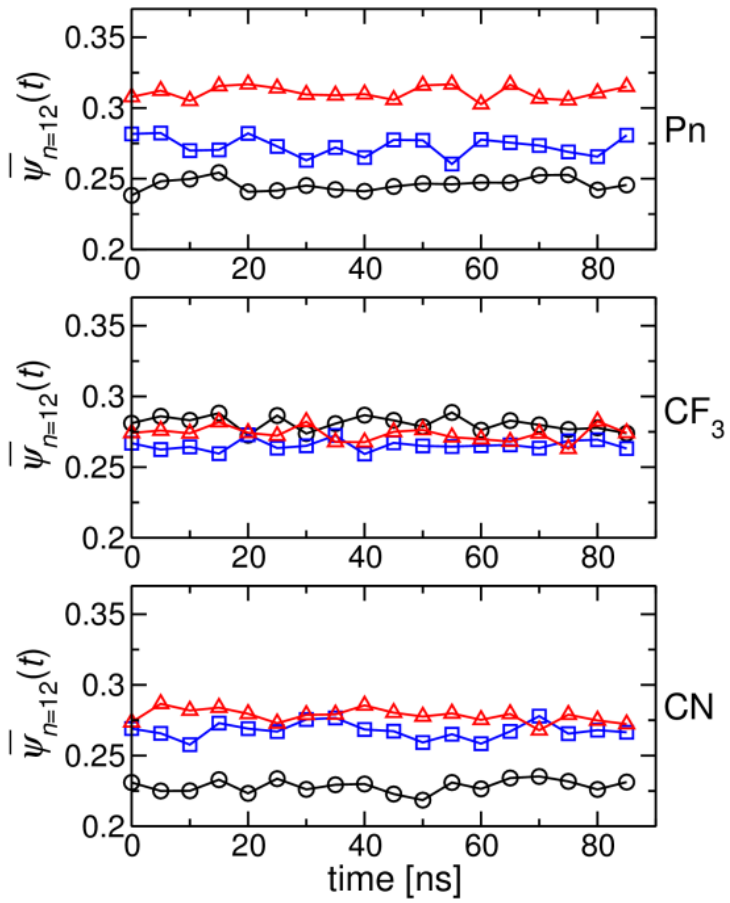

Figure B3 Normalized demixing parameter $\overline{\psi}_n$ (n = 12) of P3HT:acene blends determined from CG simulations at 550 K. Circles, squares, and triangles denote TES-, TIPS- and TCPS-acenes, respectively.

Atomistic force field

The force-field parameters for P3HT used in this work are taken from Schwarz *et al*.,[1] which were similar to those used by Huang *et al*.[2] except for slight modifications. In Schwarz *et al*., the optimized inter-monomer dihedral potential was partitioned evenly among the four dihedrals bridging the inter-monomer bond. Instead of using harmonic improper dihedrals to keep the chain backbone adequately rigid as in Huang *et al*., the OPLS-AA dihedral potential for aromatic carbons forming rings "CA-CA-CA-CA" were used instead.

The analytical form of the various bonded and non-bonded OPLS-AA[3] potentials for the acene molecules are shown below:

$$V_{\text{bond}}(l) = k_l(l - l_0)^2$$

$$V_{\text{angle}}(\theta) = k_\theta(\theta - \theta_0)^2$$

$$V_{\text{dihedral}}(\varphi) = \sum_{n=1}^{5} A_n \cos^{n-1}(\varphi)$$

$$V_{\text{LJ}}(r_{ij}) = 4\varepsilon_{ij}\left[\left(\frac{\sigma_{ij}}{r_{ij}}\right)^{12} - \left(\frac{\sigma_{ij}}{r_{ij}}\right)^{6}\right],$$

with combining rules $\sigma_{ij} = \sqrt{\sigma_{ii}\sigma_{jj}}$ and $\varepsilon_{ij} = \sqrt{\varepsilon_{ii}\varepsilon_{jj}}$

$$V_{\text{Coulomb}}(r_{ij}) = \frac{q_i q_j e^2}{4\pi\epsilon_0 r_{ij}}$$

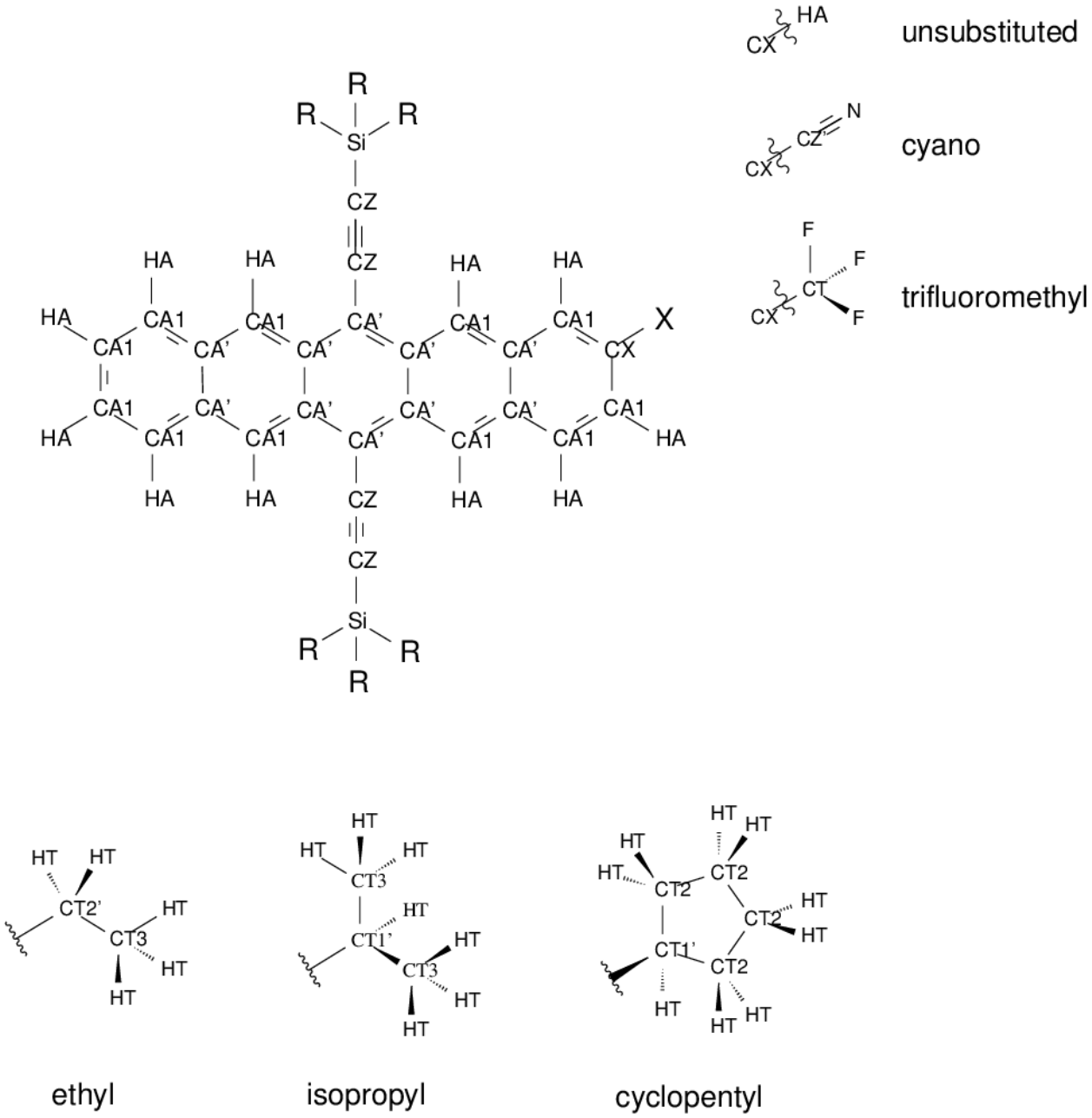

Figure B4 The chemical structures of the acene molecules with atom types defined.

Table B1 Pairwise non-bonded potential parameters (Lennard-Jones and Coulomb) for the acene molecules.

atom type	mass [amu]	σ_{ii} [Å]	ε_{ii} [kcal mol^{-1}]	q_i [e]
CA1	12.011	3.5500	0.0700	-0.1150
CX = CA1	12.011	3.5500	0.0700	-0.1150
HA	1.008	2.4200	0.0300	+0.1150
CA’	12.011	3.5500	0.0700	0.0000
CZ	12.011	3.3000	0.2100	0.0000
Si	28.086	4.0000	0.1000	+0.9999
CT1’	12.011	3.5000	0.0660	-0.3933
CT2’	12.011	3.5000	0.0660	-0.4533
CT2	12.011	3.5000	0.0660	-0.1200
CT3	12.011	3.5000	0.0660	-0.1800
HT	1.008	2.5000	0.0300	+0.0600
CX = CA2	12.011	3.5500	0.0700	+0.0350
CZ’	12.011	3.6500	0.1500	+0.3950
N	14.007	3.2000	0.1700	-0.4300
CX = CA3	12.011	3.5500	0.0700	+0.1500
CT	12.011	3.2500	0.0620	+0.4500
F	18.998	2.9400	0.0610	-0.2000

Table B2 Harmonic bond potential parameters for the acene molecules.

bond type	k_l [kcal mol^{-1} Å^{-2}]	l_0 [Å]
CA-CA	469.00	1.400
CA1-HA	367.00	1.080
CA-CZ	400.00	1.451
CZ-CZ	1150.00	1.210
CZ-Si	187.00	1.860
Si-CT	187.00	1.860
CT-CT	268.00	1.529
CT-HT	340.00	1.090
CZ’-N	650.00	1.157
CA3-CT	317.00	1.510
CT-F	367.00	1.360

Table B3 Harmonic angle potential parameters for the acene molecules.

angle type	k_θ [kcal mol^{-1} rad^{-2}]	θ_0 [deg.]
CA-CA-CA	63.00	120.00
CA-CA-HA	35.00	120.00
CA-CA-CZ	70.00	120.00
CA1-CZ-CZ	160.00	180.00
CZ-CZ-Si	160.00	180.00
CZ-Si-CT	60.00	110.00
CT-CT-Si	60.00	112.00
CT-Si-CT	60.00	110.00
Si-CT-HT	35.00	109.50
CT-CT-CT	58.35	112.70
CT-CT-HT	37.50	110.70
HT-CT-HT	33.00	107.80
CA2-CZ'-N	150.00	180.00
CA1-CA3-CT	70.00	120.00
CA3-CT-F	50.00	109.50
F-CT-F	77.00	109.10

Table B4 Dihedral potential parameters for the acene molecules. All units are kcal mol^{-1}.

dihedral type	A_1	A_2	A_3	A_4	A_5
CA-CA-CA-CA	7.250	0.000	-7.250	0.000	0.000
CA-CA-CA-HA	7.250	0.000	-7.250	0.000	0.000
HA-CA-CA-HA	7.250	0.000	-7.250	0.000	0.000
CA-CA-CA-CZ	7.250	0.000	-7.250	0.000	0.000
CA-CA-CZ-CZ	0.000	0.000	0.000	0.000	0.000
CA-CZ-CZ-Si	0.000	0.000	0.000	0.000	0.000
CZ-CZ-Si-CT	0.000	0.000	0.000	0.000	0.000
CZ-Si-CT-CT	0.500	0.500	0.000	0.000	0.000
CZ-Si-CT-HT	0.090	-0.270	0.000	0.360	0.000
Si-CT-CT-CT	0.000	0.000	0.000	0.000	0.000
Si-CT-CT-HT	0.225	-0.675	0.000	0.900	0.000
CT-CT-CT-CT	0.700	0.350	0.050	0.400	0.000
CT-CT-CT-HT	0.150	-0.450	0.000	0.600	0.000
HT-CT-CT-HT	0.150	-0.450	0.000	0.600	0.000
CT-Si-CT-CT	0.500	0.500	0.000	0.000	0.000
CT-Si-CT-HT	0.090	-0.270	0.000	0.360	0.000
CA-CA-CA-CT/CZ'	7.250	0.000	-7.250	0.000	0.000
HA-CA-CA-CT/CZ'	7.250	0.000	-7.250	0.000	0.000
CA-CA2-CZ'-N	0.000	0.000	0.000	0.000	0.000
CA-CA3-CT-F	0.425	0.000	-0.425	0.000	0.000

Coarse-grained force field

The coarse-grained (CG) "chemical structure" of the acene molecule is shown in Figure C5. A1-A2-A3 form the pentacene backbone. A4 and A5 represent the alkylsilyl groups. Harmonic bond and angle potentials are used to retain the "+" shape of the molecule, and are listed in Tables S5 and S6, respectively. There is an excellent fit between the atomistic and CG bonded distributions for all acenes as exemplified by TIPS-Pn shown in Figures C6 and C7. There is also a good fit between the atomistic and CG radial distribution functions (RDFs) describing non-bonded interactions as exemplified by P3HT:TIPS-Pn shown in Figures C8 (acene-acene) and C9 (P3HT-acene).

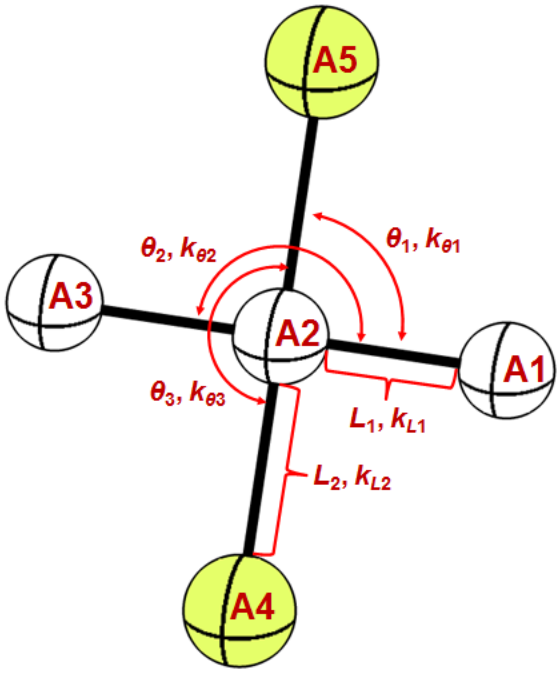

Figure B5 The "chemical structure" of the coarse-grained acene molecule with site definitions and bonded parameter definitions. Note that A1 is the site where the electron-withdrawing group is attached.

Table B5 Harmonic bond parameters for the CG acene molecules.

acene	k_{L1} [kcal mol^{-1} Å^{-2}]	L_1 [Å]	k_{L2} [kcal mol^{-1} Å^{-2}]	L_2 [Å]
TES-Pn	241.00	4.900	91.00	5.929
TES-CF_3	242.00	4.897	88.00	5.925
TES-CN	237.00	4.896	85.00	5.927
TIPS-Pn	230.00	4.900	92.00	5.912
TIPS-CF_3	230.00	4.898	90.00	5.914
TIPS-CN	231.00	4.898	90.00	5.914
TCPS-Pn	230.00	4.895	90.00	5.915
TCPS-CF_3	225.00	4.900	90.00	5.920
TCPS-CN	225.00	4.895	90.00	5.919

Table B6 Harmonic angle parameters for the CG acene molecules.

acene	$k_{\theta 1}$ [kcal mol^{-1} rad^{-2}]	θ_1 [°]	$k_{\theta 2}$ [kcal mol^{-1} rad^{-2}]	θ_1 [°]	$k_{\theta 3}$ [kcal mol^{-1} rad^{-2}]	θ_3 [°]
TES-Pn	118.00	90	95.00	180	18.00	180
TES-CF_3	115.00	90	80.00	180	14.00	180
TES-CN	118.00	90	81.00	180	13.00	180
TIPS-Pn	127.00	90	75.00	180	14.00	180
TIPS-CF_3	127.00	90	70.00	180	14.00	180
TIPS-CN	130.00	90	78.00	180	14.00	180
TCPS-Pn	132.00	90	78.00	180	15.00	180
TCPS-CF_3	134.00	90	73.00	180	15.00	180
TCPS-CN	131.00	90	78.00	180	15.00	180

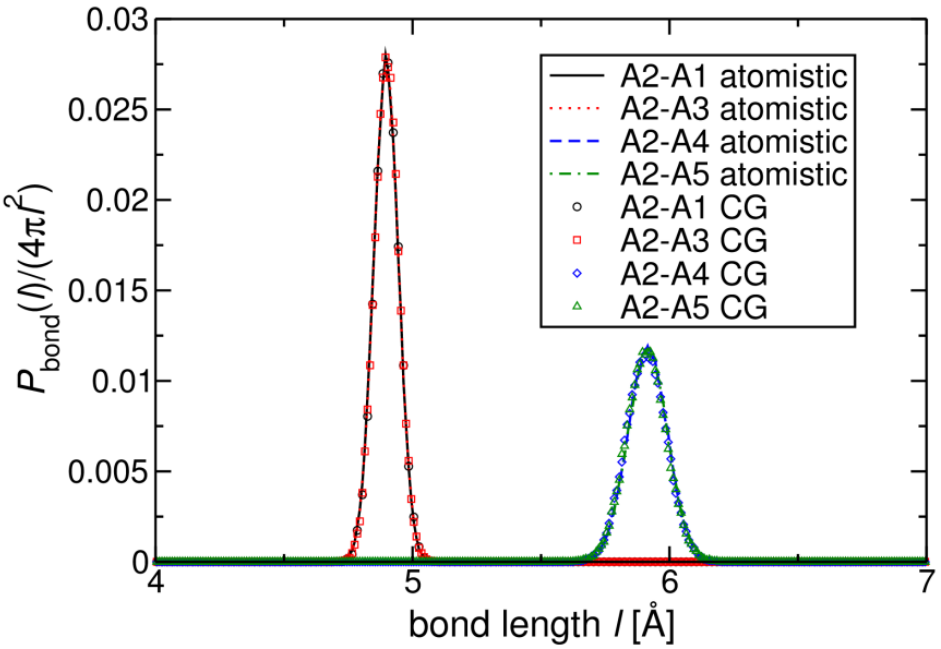

Figure B6 Bond distributions determined from atomistic (lines) and CG (symbols) NPT simulations of 128 acene molecules at 550 K and 1 atm.

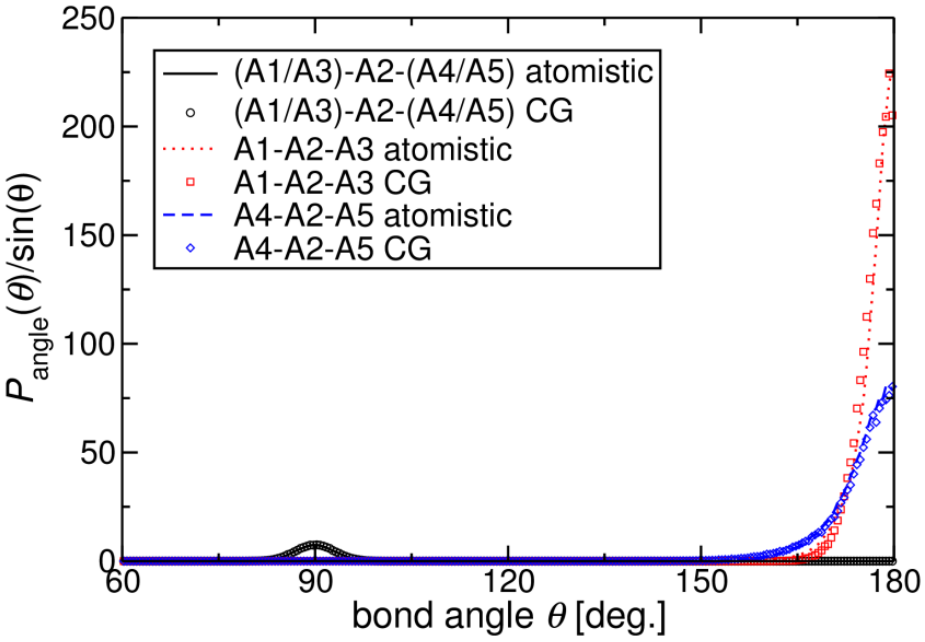

Figure B7 Angle distributions determined from atomistic (lines) and CG (symbols) NPT simulations of 128 acene molecules at 550 K and 1 atm.

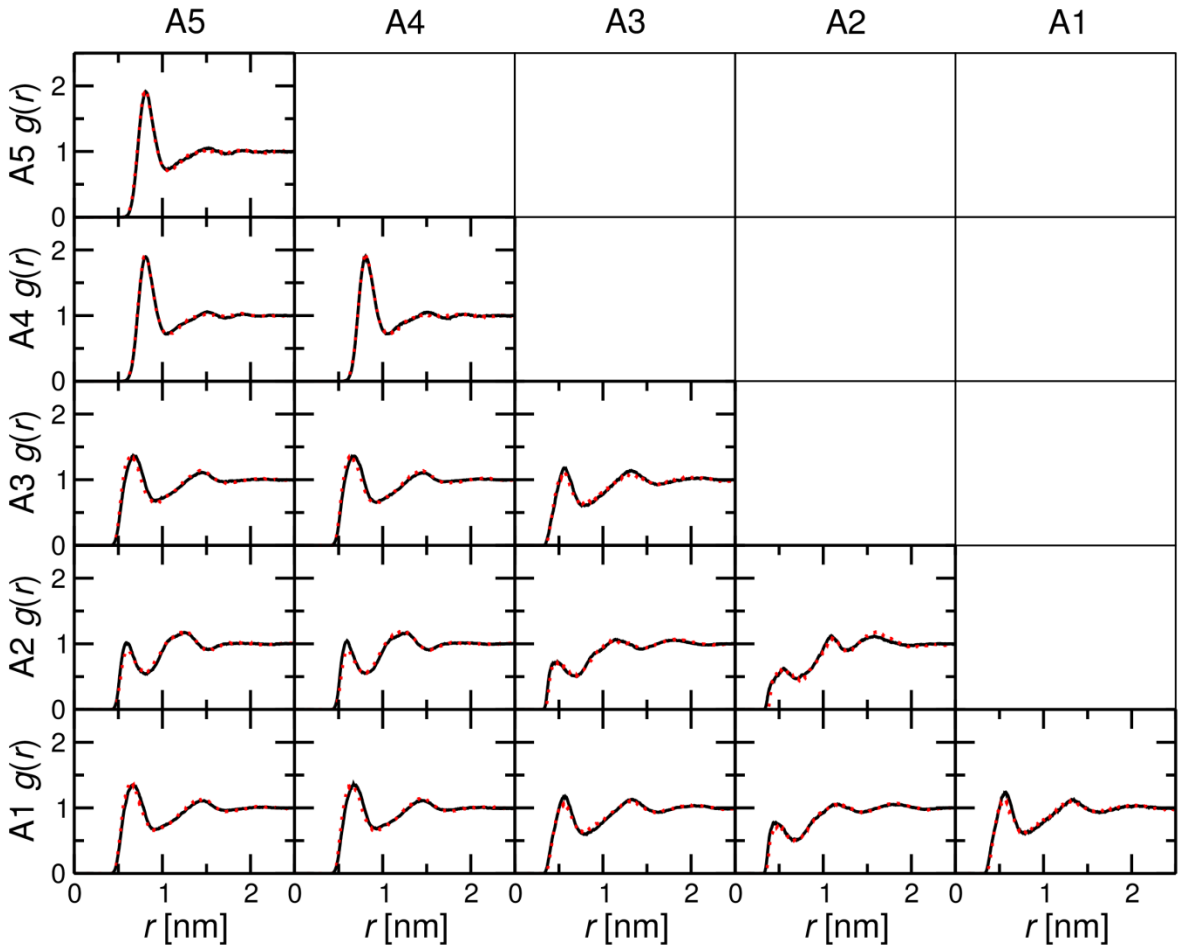

Figure B8 Radial distribution functions, $g(r)$, for pairs of sites on the TIPS-Pn molecule determined from atomistic (solid) and CG (dotted) NPT simulations of 128 TIPS-Pn molecules at 550 K and 1 atm.

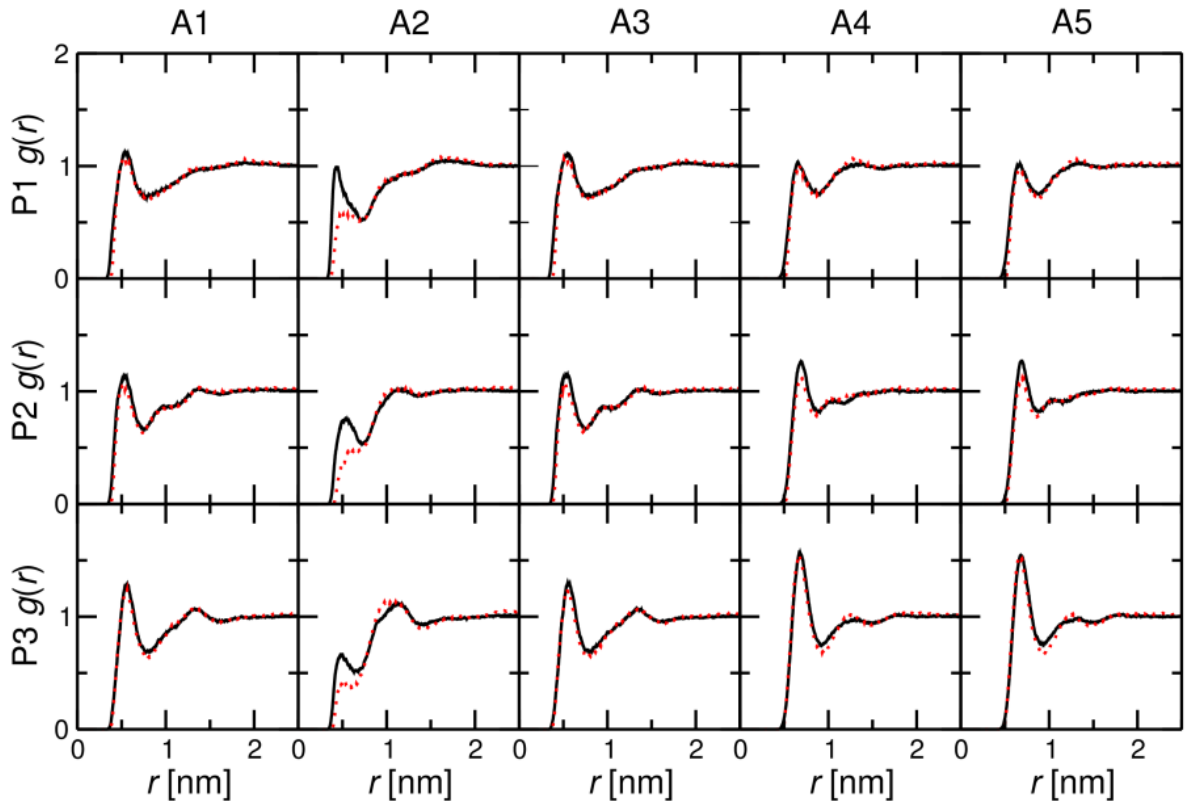

Figure B9 Radial distribution functions, $g(r)$, for pairs of sites on the P3HT chain and TIPS-Pn molecule determined from atomistic (solid) and CG (dotted) NPT simulations of 40 P3HT decamer chains and 100 TIPS-Pn molecules (1:1 wt/wt ratio) at 550 K and 1 atm.

Non-bonded CG interaction potentials

The non-bonded CG interaction potentials for P3HT-P3HT interactions are reported in the Supplementary Information of Huang *et al*. and Schwarz *et al*. The non-bonded CG interaction potentials for acene-acene and P3HT-acene interactions used here can be obtained by contacting Khanh Do at dokhanh@gmail.com. The potentials (a total of 18 sets of 15 potentials) are in a "table" format compatible with the *LAMMPS* software.

References

(1) Schwarz, K. N.; Kee, T. W.; Huang, D. M. *Nanoscale* **2013**, *5* (5), 2017.
(2) Huang, D. M.; Faller, R.; Do, K.; Moulé, A. J. *J. Chem. Theory Comput.* **2010**, *6* (2), 526.
(3) Jorgensen, W. L.; Maxwell, D. S.; Tirado-Rives, J. *J. Am. Chem. Soc.* **1996**, *118* (45), 11225.